Salt cavern volume estimation from pressure response: compressibility-based method

By

Luiza Queroga Caldas
Student Id: 4614968

in partial fulfilment of the requirements for the degree of

Master of Science
in Applied Earth Sciences

at the Delft University of Technology,
to be defended publicly on Friday August 31, 2018 at 11:15 AM.

Supervisor:	Prof. Dr. Pacelli Zitha	TU Delft
	Dr. Peter Fokker	WEP B.V.
	Prof. Dr. Hans Bruining	TU Delft
Thesis committee:	Prof. Dr. Ir. Jan Dirk Jansen	TU Delft
	Dr. Ir. Hadi Hajibeygi	TU Delft
	Dr. Ir. Anne-Catherine Dieudonné	TU Delft

This thesis is confidential and cannot be made public until August 31, 2018.

An electronic version of this thesis is available at http://repository.tudelft.nl/.

TU Delft

Title : Salt cavern volume estimation from pressure response:
compressibility-based method.

Author(s) : L. Q. Caldas

Date : August 31, 2018
Professor(s) : Prof. Dr. Pacelli Zitha
:
Supervisor(s) : Prof. Dr. Hans Bruining
: Dr. Peter Fokker, WEP B.V.
: Ir. Alex van El, WEP B.V.

Postal Address : Section for Petroleum Engineering
Department of Geoscience & Engineering
Delft University of Technology
P.O. Box 5028
The Netherlands

Telephone : (31) 15 2781328 (secretary)
Telefax : (31) 15 2781189

Contents

Salt cavern volume estimation from pressure response: compressibility-based method

Luiza Queroga Caldas

Technische Universiteit Delft – Delft, Netherlands

Abstract

Salt caverns formed by solution mining may cause soil subsidence, because the surrounding adapts to fill the void (cavity) created in the strata. The cavern volume is hence not only a function of salt extraction (estimated from mass balance) but also a function of salt creep. The cavern size can be measured by sonar, but a less costly way would be to correlate cavern volume to cavern compressibility. The size of the cavern can be obtained by a compressibility test. The compressibility test consists of injecting brine or fresh water into the cavern, causing a pressure build-up. The pressure increase depends on the cavern volume and compressibility.

Bérest et al. (2006) [1] derived an equation that expresses the pressure response to injection of a volume ΔV of fresh water. The equation includes creep that can be derived from a separate geometric creep model that relates the strain to the stress history using the Norton-Hoff law for describing an Arrhenius type of response model, and thermal expansion effects influenced by the geothermal temperature. It also considers Darcy flow and leakage through the permeable salt cavity.

This thesis investigates the sensitivity related to the various mechanisms in the Bérest and Van Sambeek (2005) model. It also extends the model by introducing chemical dissolution of salt effects and taking into account the impact of the sump (insoluble precipitates at the bottom of the cavern). We state the model equations and solve them for an example of interest. We can also compare the calculated pressure response to the results of a pressure test. In this pressure test a given volume of fresh water is injected above the sump and produced at the top of the cavity. The produced salt concentration is also one of the parameters measured in the test.

There are at least two widely used methods to obtain or predict cavern size of active salt solution mining caverns, namely sonar surveys and leaching simulators. However, these data can be flawed due to uncertainties of the methods and the accuracy of measuring devices like flow meters. The compressibility test can then be used as an additional survey method. The test execution is simple and inexpensive, making it possible to be performed more frequently than a sonar survey.

The cavern volume is obtained from a compressibility test data by using a solution that includes not only the injection volume, but also volumes introduced by other phenomena. These other phenomena are caused by thermal, hydraulic, mechanical, and chemical influences. Previous work has attempted to introduced solutions incorporating these influences for idle caverns. The proposed solution incorporates these effects in an active leaching salt cavern. It also introduces the impact of sump (insoluble on cavern bottom) to be included in the model. The proposed solution is then tested against field data.

The work here differs from previous work that it presents a comprehensive description of the various methods used in the literature and practice. Where current models predict cavity volumes with a mean absolute percentage error of 33% (Thiel's method for BAS3O) to 127% (Bérest et al. for BAS4) for the studied caverns (BAS3O and BAS4), the model here, which includes the presence of insoluble particles, and a well-established creep model is able to predict cavity volumes to an accuracy of 33% (proposed model for BAS3O) to 12% (proposed model for BAS4).

Keywords: salt solution mining, compressibility, pressure test, cavern volume estimation.

---

1. Introduction

Subsurface salt caverns resulting from solution mining can cause surface subsidence. Subsidence must be tracked and reported to government agencies. A GPS (Global Positioning System) real time survey is used to keep track of the surface level. The data give information on the size of the subsidence bowl (described by a Gaussian curve as function of distance to cavern center location), with a maximum level drop occurring above the cavern for the case of single caverns. Once the level drop reaches a limit the leaching operation in that cavern must terminate.

A model for subsidence caused by salt caverns is presented by Fokker, [2]. The key input in determining and predicting the level of subsidence is the size of the open cavity and volume of salt dissolved (produced salt volume).

$$V_s = V_d - V_{oc} \,, \qquad (1)$$

where, V_s refers to the subsidence volume, V_d to the dissolution volume and V_{oc} to the open cavity volume. Echo measurements are the most common imaging tool used to obtain salt cavern shapes and volumes and are accomplished using a costly wireline procedure. Depending on the eccentricity of the shape of the cavity and level of irregularities, the sonar tool alone might not be enough to get an accurate volume.

The use of imaging equipment has pitfalls as to inferring an under- or overestimation of cavern volumes. This drawback is caused by the inability of using acoustic waves to measure behind sharp edges [3]. Indeed, the acoustic imaging tool, Figure 1, has a characteristic wave frequency of 100 to 600 kHz (wave length is dependent on sonic velocity in the infill fluid) and it might not be able to measure behind sharp points in the cavity due to level of resolution of the wave propagation.

Cavern volume underestimation can also be caused by insoluble minerals and trapped brine at the bottom of the cavern (sump), which prevents to get an accurate profile below the sump.

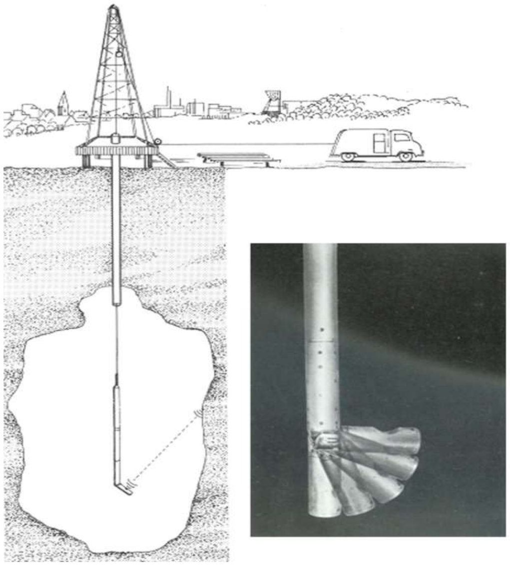

Figure 1 Illustration of echo measurement operation in a salt cavity, [4].

Wireline operations are particularly difficult in deviated wells, resulting in a long period of shut in to perform the sonar survey. In some cases, it happens that the tool cannot pass the well and cannot be used. In optimal scenarios of vertical wells, the operation takes days causing production deferment. Therefore, it is useful to develop methods to determine the cavern volume using flow rates and pressure data. This is also useful to keep continuous, frequent, monitoring of the cavity volume; meanwhile sonar measurements are done on a yearly basis.

To assure an accurate sonar measurement of cavern size a volume balance strategy is used. This is a secondary tool for quality control of the echo survey. However, both (echo and volume balance) methods present uncertainties linked to equipment calibration and consistency in procedure (caused for instance by a change of service company or tool). A third method uses pressure data. This alternative can then be of help to reconcile discrepancies in the results; or replace some of the costly echo volume measurement by a cheap alternative in the form of a pressure cycle, measuring flow volumes only.

Indeed, the proposed solution is to obtain volume estimation from pressure trends, since a correlation between cavern size and pressure response can be established from compressibility tests, [5].

Three different approaches to obtain cavern volume from compressibility tests are applied to field data viz Thiel [5], Van Sambeek et al [6] and Bérest et al. [1]. They are compared with an alternative methodology presented in this paper.

2. Concepts review

The salt cavern system is represented in Figure 2. The illustration depicts a salt solution mining cavern of irregular shape under indirect production mode, when brine is produced from central tubing. The cavern upward growth is controlled by a small volume of inert fluid with lower density than water, called blanket.

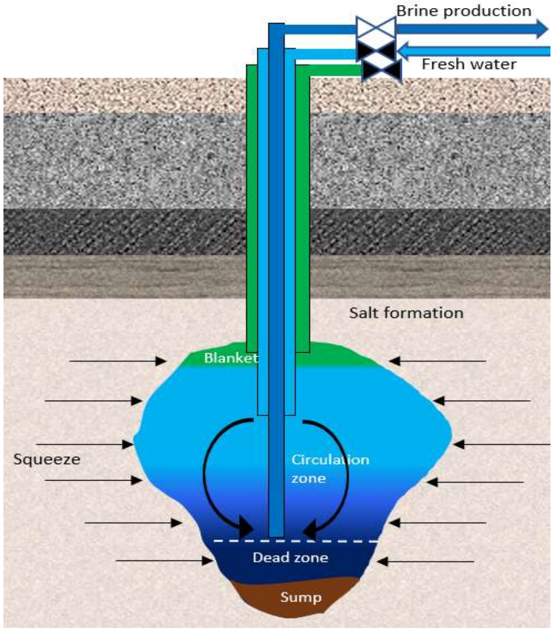

Figure 2 Representation of a salt cavern as a result of solution mining.

The injected water then circulates inside the cavern and dissolves the salt at the walls. This dissolution process liberates insoluble particles (clay and calcium sulphate in the case of BAS3O and BAS4 caverns) that accumulate at the bottom of the cavity and is referred to as sump. A dead zone is composed of saturated brine that rest at the bottom due to undersaturated brine buoyance.

2.1. Compressibility Test

The compressibility test consists of injecting fluid into the cavern during production shut-in causing compression of the system.

During a compressibility test one of the lines is shut-in and the opposite line is used for injection. This causes a pressure build-up which correlates with the cavern volume, Figure 3. In this way it is possible to obtain the cavern size. The pressure increase will be linearly related to the volume injection if only elastic behavior occurs, [7].

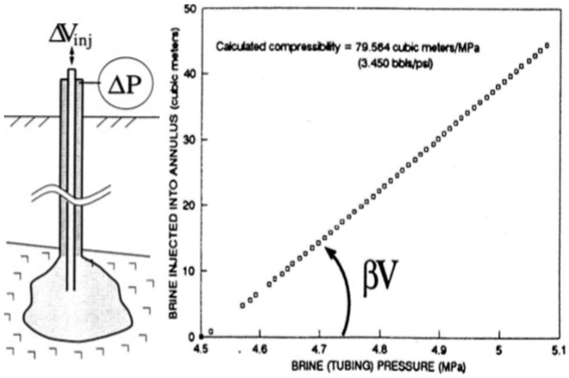

Figure 3 Compressibility test elastic response, [5]. The illustration on the left is a schematic drawing of the test with an injection volume on central tubing (ΔV_{inj}) and pressure reading on annular (ΔP). On the right is the plot of ΔV_{inj} on vertical axis and ΔP on horizontal axis, where the slope (βV) is the product of cavern volume and cavern compressibility.

However, this linear relationship only occurs in short tests. In long tests other influences in the system must be taken into account, which will result in a non-linear relationship between injection and pressure response. The coupling of all phenomena results in a THMC (Thermal Hydraulic Mechanical Chemical) process, which includes:

- Brine warming;
- Brine permeations and leaks;
- Cavity creep;
- Rock dissolution.

Also, elastic behavior is still accounted for as cavern compressibility.

2.2. Rock contribution

The rock salt exhibits an elastic-viscoplastic behavior, which is a superposition of both elastic and viscoplastic deformation.

The elastic component of the deformation is described by cavity compressibility.

2.2.1. Cavity elastic deformation

When fluid is injected into the cavern the formation deforms elastically to increase its volume, while the fluid within the cavern is compressed. The elastic deformation is an immediate response besides other time dependent factors. Assuming elastic behavior the cavern wall volumetric deformation is determined by a relationship between the rock elastic constants (E, ϑ), effective stress $(\sigma_{eff} = P_\infty - P_c)$, and cavity geometry (shape factor F), [8].

$$\frac{\delta V}{V} = -F\,\frac{(1+\vartheta)}{E}\,(P_\infty - P_c) \qquad (2)$$

The full derivation is given in appendix B. The effective stress is function of cavern pressure (P_c) and the lithostatic stress (or pressure) (P_∞) which is assumed as uniform all over the cavity. Rock salt is an isotropic material, and therefore the maximum (SH) and minimal (Sh) horizontal stresses have the same value, [9]. The overburden stress is referred as Sv, and defined as function of depth and overlying strata density, [10].

$$Sv = \int_0^z \rho(z) g \, dz \qquad (3)$$

Considering the average rock salt density of $2160\ kg/m3$ (density of halite), the vertical stress as function of depth is approximately $2.12\ MPa/km$, [11]. For a rock of viscoelastic behavior, according to Maxwell and Burgers model, the stress state approaches lithostatic condition. The assumption of lithostatic condition is known as Heim's rule, and $SH = Sh = Sv$ after a long time, [11] [12] ,therefore $P_\infty \rightarrow Sv$.

From eq. (2), cavern isothermal compressibility is obtained in appendix B, resulting in,

$$\beta_c = F\,\frac{1+\vartheta}{E}. \qquad (4)$$

The parameters are obtained from a rock sample laboratory analysis, except for the shape factor.

2.2.2. Shape factor

The shape factor can vary from 2 for the case of an infinite cylinder to 1.5 (least compressible) for the case of a sphere. For flat cavities (penny-shaped), the shape factor can be greater than that of an infinite cylinder, [8]. Figure 4 shows the impact of cavern geometry on the shape factor.

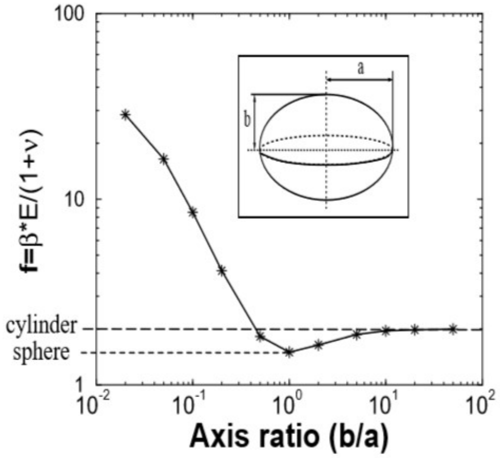

Figure 4 Cavern shape factor for an elliptical cavern, [8]. On the vertical axis is the shape factor varying from 1.5 for a sphere to 2 for a cylinder. On the horizontal axis is the ratio between cavern length and height.

During a cavern life span the shape factor changes due to changes in leaching mode. Under indirect dissolution (or production mode) most dissolution occurs at the injection depth (casing shoe), causing a faster cavern radial growth. Hence, cavern shaped is not constant in time.

2.3. Fluid contribution

Inside salt cavities used for salt solution mining three fluids are present: brine, inert fluid (diesel), and insoluble mixture. Each of these fluids are present in different proportions. The brine is the main fluid occupying the circulation zone of the cavern and can have different salt concentrations with depth or radially due to diffusion. The inert fluid is presented at significantly smaller volume. The sump is composed by a mixture of brine and insoluble material that precipitates at cavern bottom.

The fluid trapped inside of the cavern will compress to accommodate the injected volume during compressibility test. The final compressibility is obtained from the combination of each of fluids in the system.

2.3.1. Brine compressibility

When the composition is poorly known, which will be almost always the case in practice, brine isothermal compressibility is obtained from echo surveys. From this datum brine compressibility is obtained [7],

$$\beta_b = \frac{1}{\rho_b c_f^2}. \tag{5}$$

A reasonable value for brine compressibility in saturated caverns is $2.57 \times 10^{-10}\ Pa^{-1}$, [13]. If the cavity is undersaturated due to high fresh water injection volumes and low production, brine compressibility can be higher, but never more than that of fresh water $(4.45 \times 10^{-10}\ Pa^{-1})$. In fact, dissolution of the salt occurs very rapidly, as per calculations in Appendix D, and therefore the compressibility will tend to be that of a saturated brine.

2.3.2. Blanket compressibility

Blanket compressibility is much larger than brine. The total open cavern compressibility is defined as the volume average between diesel and brine, [7].

$$\beta_f = x\beta_b + (1-x)\beta_d \tag{6}$$

However, the volume fraction of inert fluid is very small compared with that of brine. Therefore, in most cases (for active salt solution mining caverns) the blanket compressibility impact can be neglected and $\beta_f \rightarrow \beta_b$.

2.3.3. Sump compressibility

In previous studies the sump influence is disregarded and only the volume of free brine is considered. The sump is present on the bottom of the cavern, and it consists of an accumulation of precipitation of insoluble material and trapped brine. This creates a liquid-solid mixture on the bottom of the cavity, [14]. The compressibility of the sump is obtained by an average between trapped brine and insoluble components, or from analysis of samples.

$$\beta_s = (1-y)\beta_{ins} + y\beta_b \tag{7}$$

For old salt caverns the volume of sump becomes extensive, thus impacting in total cavern compressibility. Cavern total compressibility is obtained from the summation of cavity and average of infill fluid compressibility,

$$\beta = \beta_c + y\beta_b + (1-y)\beta_s. \tag{8}$$

The impact of sump is included in the data analysis results, as obtained from volume balance data.

3. Proposed model

The behaviour of the cavern depends in four main physical phenomena, namely;

- Thermal – brine warming;
- Hydraulic – brine losses;
- Mechanic – rock creep,
- Chemical – salt dissolution.

These effects are more significant in large sized $(100{,}00\ m^3)$ caverns at great depths $(> 2{,}000m)$, since at those depths temperatures and overburden pressure are high. The cavern volume will determine the significance of the contribution of these factors when compared with injected volumes, as presented in normalized values in appendix D and appendix E.

Due to these phenomena it is not possible to obtain a linear relationship between pressure build up and injectivity in a compressibility test as proposed by Thiel, [15]. The solution is to incorporate such effects into the model by taking each influence separately as proposed by Bérest [1] and Van Sambeek, [6].

The individual effect of each phenomenon is discussed in detail below.

3.1. Thermal

At cavern depth the geothermal temperature is higher than that of the injected water, or of the average temperature of the brine inside the cavity. As a result, the brine warms up and expands. The added thermal volume is a function of the temperature increase inside the cavern.

The added volume caused by thermal phenomena is described by the brine volumetric thermal expansion coefficient,

$$\Delta V_{th} = \gamma_b V_c \Delta T_b. \tag{9}$$

The brine temperature increase is obtained from the heat equation for a cavity bounded by geothermal temperature and known initial brine temperature.

Rock temperature can be calculated from the correlation between depth and geothermal gradient $T_\infty = 10 + 0.03 * z$, where z is depth in m. However, temperature within rock salt is lower than that of other formations, Figure 5. This is due to the high thermal conductivity of rock salt ($K_s^{th} = 6\ W/m^oC$), [16].

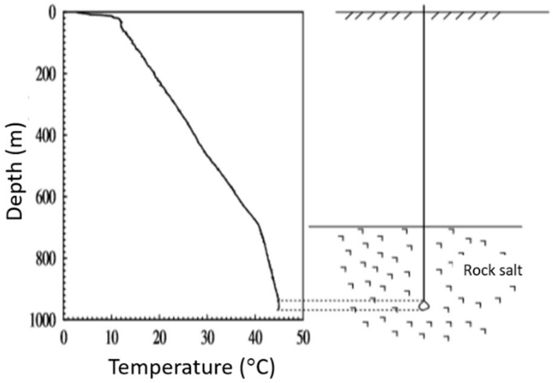

Figure 5 Geothermal temperature as function of depth for rock salt (Ez53 cavity), [16].

The model for temperature increase is then obtained by using the heat equation and Fourier's law for conductive heat transfer. Van Sambeek [6] proposed the solution for the temperature increase, assuming constant geothermal temperature at rock wall and average initial brine temperature. The derivation of the solution is given in appendix B. For the spherical cavity the solution can be simplified to,

$$\Delta\theta = \frac{3\chi}{\pi}\left[\theta_R^\infty - \theta_i(0)\right]\left[\frac{t}{t_c^{th}} + 2\sqrt{\frac{t}{t_c^{th}}}\right]. \tag{10}$$

We did not attempt to verify this solution in this work since the details of the derivation provided by Van Sambeek are unclear.

The thermal capacity ratio is given by $\chi = \frac{\rho_s c_s}{\rho_b c_b}$ (obtained in appendix B) and the characteristic time for a sphere is as,

$$t_c^{th} = \frac{R^2}{\pi\, k_s^{th}}. \tag{11}$$

For a cylindrical form the temperature increase is then as in,

$$\Delta\theta = \frac{2\chi}{\pi}\left[\theta_R^\infty - \theta_i(0)\right]\left[\frac{t}{2t_c^{th}} + 2\sqrt{\frac{t}{t_c^{th}}}\right]. \tag{12}$$

However, the characteristic time is then a logarithmic function dependent on cavern geometry and empirical values, as given by, [17].

$$t_c^{th} = a\exp\left[-\frac{1}{2}\left(\frac{\ln\left(\frac{H/D}{A_0}\right)}{b}\right)^2\right] \tag{13}$$

The equations are obtained as in appendix B. According to Karimi-Jafari, [17], typical values for the empirical constants are $a = 4.67\ years,\ b = 1.97$ and $A_0 = 0.91$. The ratio between cylinder height and diameter is H/D.

3.2. Hydraulic

There are two ways for hydraulic losses in the system. One is by leakages from topsides and fittings. Second is by permeation of brine into the formation. The latest is the expected to be the least important due to extremely low salt permeability. Permeation losses become relevant if the cavity has interbedded permeable formations within the salt formation, or due to connectivity of secondary porosity as cavern pressure approaches lithostatic.

Leakages occur as a function of pressure build up. The higher the pressure being applied in piping and fitting, the higher will be the fluid loss. The volume loss by leak is given by, [18],

$$\Delta V_{leak} = \psi(P_c - P_o), \tag{14}$$

where ψ is the leak constant rate in $\frac{m3}{Pa.s}$. Permeation losses are also linked to the difference between cavern and pore pressure, as dictated by Darcy's law, [2] [19].

The model for permeation losses is then obtained by using fluid diffusivity equation and Darcy's law for flow in porous media. An analytical solution is obtained in appendix B by taken the assumption of steady-state flow regime ($\frac{\partial P}{\partial t} = 0$), incompressible flow, laminar flow, and non-slip of fluid at wall, as mentioned by Dake, [19].

The solution for the total volume loss during the test from diffusivity equation for a spherical sphere (spherical flow) is then obtained for the cavern surface as in appendix B, resulting in,

$$\Delta V_p = t\frac{4\pi K_s}{\eta_b}\left(\frac{R_c r_\infty}{r_\infty - R_c}\right)(P_c - P_o). \tag{15}$$

Taken the same assumptions for the case of cylindrical cavity (with predominant radial flow) the solution is then as,

$$\Delta V_p = t\frac{2\pi H \quad s}{\eta_b}\left(\frac{1}{\ln\frac{r\infty}{R_C}}\right)(P_c - P_o). \tag{16}$$

For the case where $\mathrm{r}_\infty \rightarrow \infty$, then the solution reduces to $\Delta V_p(\mathrm{r}_\infty \rightarrow \infty) = 0$.

Values for rock permeability vary from a highly permeable salt $K_s = 10^{-4} mD$ (comparable to competent clay) to a low permeable salt $K_s = 10^{-1} nD$ (at the measuring lower bound), [20] [21].

The total hydraulic volume loss is then obtained by summing both leak and permeation losses.

$$\Delta V_{hy} = \Delta V_p + \Delta V_{leak} \tag{17}$$

However, even for highly permeable salts with great contact area the volume losses by permeation are very small. Leak rates are more likely to have significant impact than permeation losses.

3.3. Mechanical

One of the mechanisms with larger impact in cavern volume change in time is creep (viscoplastic deformation). Salt deformation can be elastic or viscoplastic.

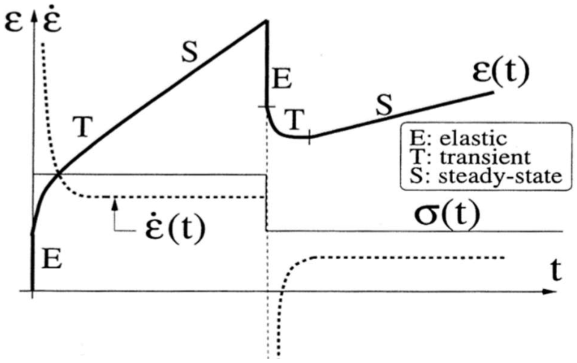

Figure 6 Strain of a Burgers type material, [7], [17]. On the vertical axis the stress (thin solid line curve), strain (thick solid line) and strain rate (dotted line). Time is on horizontal axis. The plot describes the strain (creep deformation) as a function of time caused by a constant effective stress and relaxation response. The deformation shows firstly an immediate elastic response, followed by a transient state, and finally a steady-state deformation characterized by a constant deformation rate.

During the viscoplastic behavior two states are observed; transient and steady-state creep, as in Figure 6. The transient regime, or primary creep, occurs whenever there is a change in effective Von Mises stress (or equivalent shear parameter) on the rock until it reaches steady-state, or secondary creep, [22].

Steady-state creep is observed in caverns under creep for an extended period. The negative primary creep occurs in a pressurization test, whereas it adds to creep in de depressurization test. For a conservative measure of creep in a compression test (as the primary creep reduction is more difficult to quantify) steady-state stress creep is assumed to be dominant. During the compressibility test the pressure increase is much smaller than that of the effective stress, therefore this is a reasonable to assumption. Steady-state creep Norton-Hoff law for unidimensional stress is expressed as,

$$\dot{\varepsilon}_{ss} = A\, e^{-\frac{Q}{RT\infty}}\sigma^n. \tag{18}$$

Observe that A, Q, R and n are empirical constants, which can be obtained from lab core analysis. Note that these parameters may be scale dependent and that laboratory data are not optimal for field behavior.

The solution for salt cavity deformation is then obtained by using the equilibrium equation and Norton-Hoff's creep law for isotropic material. The equilibrium equation for a sphere is presented in appendix B, [23]. It is assumed that radial component of the deformation is predominant.

$$\frac{\partial\sigma_{rr}}{\partial r} + \frac{2}{r}(\sigma_{rr} - \sigma_{\theta\theta}) = 0 \tag{19}$$

For the case of cylindrical geometry, the equilibrium is then written as, [11],

$$\frac{\partial\tau_{r\theta}}{\partial r} + \frac{1}{r}\frac{\partial\sigma_{\theta\theta}}{\partial\theta} + \frac{2\tau_{r\theta}}{r} = 0. \tag{20}$$

The total volume change in the massive caused by the geometric creep can be obtained by integrating displacement around the cavity and applying known boundary conditions, as shown in detail in appendix B. The solution for the deformation rate for steady-state creep for the spherical form is presented below, [6].

$$\frac{\dot{V}_C}{3V_C} = -\frac{1}{2}\left[\frac{3}{2n}(P_\infty - P_C)\right]^n Ae^{-\frac{Q}{RT\infty}} \tag{21}$$

In the case of rock cooling (cooled down of cavern wall) the creep could be slightly overestimated by taking the far field (initial) temperature to be representative of wall temperature.

The cylindrical form of the equation is also presented by Van Sambeek, [6], as obtained in appendix B and displayed below.

$$\frac{\dot{V}_c}{2V_c} = -\frac{\sqrt{3}}{2}\left[\frac{\sqrt{3}}{n}(P_\infty - P_c)\right]^n Ae^{-\frac{Q}{RT\infty}} \qquad (22)$$

The negative sign means the reduction of cavity radius. Since in steady-state the creep rate is constant, then the total creep volume during a period of time for a sphere is,

$$\Delta V_{cr} = t * V_c\left(\frac{3}{2}\left[\frac{3}{2n}(P_\infty - P_c)\right]^n Ae^{-\frac{Q}{RT\infty}}\right). \qquad (23)$$

For the case of a cylindrical cavity the creep volume is given by,

$$\Delta V_{cr} = t * V_c\left(\sqrt{3}\left[\frac{\sqrt{3}}{n}(P_\infty - P_c)\right]^n Ae^{-\frac{Q}{RT\infty}}\right). \qquad (24)$$

Creep deformation is then the same as the total mechanical influence in the cavern, $\Delta V_{cr} = \Delta V_{mc}$.

3.4. Chemical

The brine inside an idle cavern has already reached the maximum saturation, hence additional dissolution occurs only due to pressure increase changing maximum saturation point, [16].

Meanwhile, in an active cavern brine is yet undersaturated with a concentration profile leading to continuous dissolution, [24].

Due to the dissolution the cavern size increases, and the brine density changes. Both factors will play a role in the pressure response of the system.

The amount of salt being dissolved can be obtained from Fick's law, which describes the mass transfer in a system. The equation without advective flux, is written as,

$$J(r,t) = -D_{ab}\nabla\mathbf{c}. \qquad (25)$$

To simplify the chemical problem, it is assumed that the concentration of salt inside the cavern is a function of time. Hence, the equation can be simplified by taking a mass transfer rate for a zero-dimensional model as presented,

$$N = k(c_{sat} - c). \qquad (26)$$

The convective mass transfer coefficient (k) is obtained from the Sherwood, Grashof, and Schmidt number, i.e. [25]; [26].

$$Sh = 0.13(GrSc)^{1/3} = \frac{kh}{D_{ab}} \qquad (27)$$

$$Gr = \frac{h^3 g\rho\Delta\rho}{v^2} \qquad (28)$$

$$Sc = \frac{v}{D_{ab}} \qquad (29)$$

The change in salt volume in brine is the same as the salt dissolved from the cavern wall. Hence, change in concentration in time can be obtained as,

$$\frac{4\pi R_c^3}{3}\frac{dc}{dt} = 4k\pi R_c^2(c_{sat} - c), \qquad (30)$$

$$\frac{dc}{dt} = \frac{3}{R_c}k(c_{sat} - c) = \frac{N}{h}. \qquad (31)$$

The detailed solution is elucidated in appendix B.

In case of compressibility test, due to the short duration, the amount of salt dissolved is much smaller than that of the cavity. It is plausible to assume that the dissolution rate is somewhat constant during the test.

The total volume of salt consumed from the cavern wall for a spherical shaped cavity is then presented in equation (30) as its simplified form for a steady-state dissolution.

$$\Delta V_d = 4\pi R_c^2\frac{k(c_{sat} - c_0)}{\rho_s}t \qquad (32)$$

For the case of a cylindrical cavity with predominant radial dissolution then the dissolved salt volume is;

$$\Delta V_d = 2\pi R_c H\frac{k(c_{sat} - c_0)}{\rho_s}t. \qquad (33)$$

The concentration must be converted from mol/m^3 to kg/m^3, by dividing the molar concentration by salt molecular weight, ($0.0584\frac{kg}{mol}$ for $NaCl$).

4. Methodology

The proposed approach, analogous to Thiel's relationship, obtains cavern volume from pressure response assuming constants compressibility, [15].

$$\Delta V_{ad} = \beta V^{f} \Delta P_{c} \tag{34}$$

where, V^{f} is the average cavern volume.

The components are replaced by identified volumetric changes in the cavern.

$$\Delta V_{ad} = \Delta V_{th} + \Delta V_{inj} - \Delta V_{hy} \tag{35}$$

$$V^{f} = V^{o} + \Delta V_{ch} - \Delta V_{mc} \tag{36}$$

Where, V^{o} is the initial cavern volume (before test). The appropriate relationship is obtained in appendix A. The LHS of equation (34) describes the volume gained by compressibility which should be, as in equation (35), the same amount of volume added by volumetric expansion of brine (ΔV_{th}), the injected volume (ΔV_{inj}), and subtracted volume loss by permeation and leak (ΔV_{hy}). The latest, ΔV_{hy}, has a negative contribution since it describes flow from the cavern to the formation. The RHS of equation (34) is composed as in equation (36) by the cavern volume after radial size changes due to chemical dissolution (ΔV_{ch}) causing a positive increment and creep deformation (ΔV_{mc}) causing a negative radial size change (creep is reducing cavity size).

Substituting ΔV_{ad} components in equations (34), by (35) and (36), results in a coupled analytical solution for the change in pressure,

$$\Delta V_{inj} + \Delta V_{th} - \Delta V_{hy} = \beta (V^{o} + \Delta V_{ch} - \Delta V_{mc}) \Delta P_{c}. \tag{37}$$

This can be re-written as;

$$\frac{\Delta V_{inj}}{\Delta P_c} = V^{o}\left[\beta\left(1 + \frac{\Delta V_{ch}}{V^{o}} - \frac{\Delta V_{mc}}{V^{o}}\right) - \frac{1}{\Delta P_c}\left(\frac{\Delta V_{th}}{V^{o}} - \frac{\Delta V_{hy}}{V^{o}}\right)\right]. \tag{38}$$

The LHS of equation (38) is obtained from measurements taken during the test, for injection and pressure. The RHS is obtained from pressure measurement, known parameters and estimated cavern radius (or volume). The parameters can be estimated from the laboratory; however, scale dependency may cause that parameters from laboratory are not accurate for field predictions.

As in appendix A, the equation can then be re-written as isolating the cavern volume on LHS;

$$V^{o} = \frac{\Delta V_{inj}}{\Delta P_c}\left[\beta\left(1 + \frac{\Delta V_{ch}}{V^{o}} - \frac{\Delta V_{mc}}{V^{o}}\right) - \frac{1}{\Delta P_c}\left(\frac{\Delta V_{th}}{V^{o}} - \frac{\Delta V_{hy}}{V^{o}}\right)\right]^{-1}. \tag{39}$$

Each of the volumetric components are obtained as in equations from previous section, and the hydraulic response, $\frac{\Delta V_{inj}}{\Delta P_c}$,from field measurements.

4.1. Coupled form

The coupled form is obtained by substituting the equations (9), (17), (23) and (32) in equation (39). An analytical solution for the spherical cavern, for the case of $r_{\infty} \gg R_c$, as in appendix B, is

$$\frac{\Delta V_{inj}}{\Delta P_c} = V^{o}\Bigg[\beta\Bigg(1 + t\frac{3}{R}\frac{k(c_{sat}-c_0)}{\rho_s} - t\frac{3}{2}A^{*}\left[\frac{3}{2n}(P_{\infty} - P_c)\right]^{n}\Bigg) - \frac{1}{\Delta P_c}\Bigg(\gamma_b\frac{3\chi}{\pi}\left[T_{\infty} - T_b^{o}\right]\left[\frac{t}{t_c^{th}} + 2\sqrt{\frac{t}{t_c^{th}}}\right] - t(P_c - P_o)\left(\frac{3}{R^3}\frac{K}{\eta_b} + \psi^{o}\right)\Bigg)\Bigg]. \tag{40}$$

On the LHS is the ratio between volume injected and pressure readings, on the RHS, from left to right, are the terms for salt dissolution, creep, volumetric thermal expansion, permeation and leaks.

Analogous to the spherical form, the equation for cylindrical shaped cavities is;

$$\frac{\Delta V_{inj}}{\Delta P_c} = V^{o}\Bigg[\beta\Bigg(1 + \frac{2}{R}\left(1 + \frac{R}{H}\right)\frac{k(c_{sat}-c_0)}{\rho_s}\,t - t\sqrt{3}A^{*}\left[\frac{\sqrt{3}}{n}(P_{\infty} - P_c)\right]^{n}\Bigg) - \frac{1}{\Delta P_c}\Bigg(\gamma_b\frac{2\chi}{\pi}\left[T_{\infty} - T_b^{o}\right]\left[\frac{t}{2t_c^{th}} + 2\sqrt{\frac{t}{t_c^{th}}}\right] - t(P_c - P_o)\psi^{o}\Bigg)\Bigg] \tag{41}$$

For the case of cylindrical cavities, the equivalent radius is $R_c = \sqrt{V/\pi H}$.

Observe that, on the RHS of the equation, due to the compressibility factor and magnitude, the thermal and leaking volumes are more significant.

4.2. Measurement Readings

Cavern pressure and temperature measurements are often obtained by surface equipment. In situ data are not available, unless bottom hole gauges are installed.

This imposes a challenge in estimating brine in situ temperature, and values can be estimated from production data.

On the pressure side, the increase in pressure read at the surface is the same as that inside the cavern ($\Delta P_c = \Delta WHP$), when measured at the tubing opposite to the injection line. The same applies for the outer annular (of total true vertical depth H_{ann}) filled with blanket fluid, except that corrections must be made due to the blanket fluid (usually diesel) cooling.

$$\rho_d^f = \frac{\rho_d^o}{1+\gamma_d \Delta T} \tag{42}$$

$$\delta P_{th} = \left(\rho_d^f - \rho_d^o\right) g H_{ann} \tag{43}$$

The change in temperature, ΔT, in equation (42) is different than that of the brine and obtained from observed temperature measurements of the blanket at the wellhead. During the test in winter conditions this plays a significant role when taking measurement from the diesel blanket, since cold water injection cools down the blanket fluid on the outer string. The opposite effect occurs, and is observed in the field, when warm brine is bled of causing the outer annular fluid temperature to increase and consequently the pressure reading on the outer annular increases instead of decreases.

Outer blanket pressure information is useful as an alternative in case of errors in opposite annular measurements. The error may be caused for e.g. by salt crystallization in the brine filled tubing creating a blockage between cavern and piping.

4.3. Model sensitivity

A full sensitivity of each of the parameters on the process volumes of the model, equation (39), is presented separately in appendix D. The referred process volumes include: thermal volume due to brine expansion (ΔV_{th}), creep volume causing cavern size reduction (ΔV_{mc}), chemical volume causing cavern size increase (ΔV_{ch}), and hydraulic volume caused by permeation and leaks (ΔV_{hy}).

From the extensive results found in appendix D, the largest sensitivity to cavern volume prediction for Bérest and Van Sambeek models are in the creep volume and the second largest sensitivity is for the thermal volume. For Thiel method the largest sensitivity is to compressibility, since this is the only input parameter in this model. For the proposed model the largest sensitivity is to the thermal volume.

The largest sensitivity in creep prediction is caused by Norton-Hoff law constants. On thermally added volume the largest sensitivity lays on the initial brine temperature. Chemical volume is largely impacted by the overall brine concentration.

The sensitivity analysis is performed by varying one of the parameters and observing the impact in the THMC process volumes. The set of parameters applied are summarized in Table 1.

Table 1 Input values for sensitivity analysis. Values without reference are based on field data measurements and calculations.

	Parameter (from field data and references)	Value	Unit
A	Norton-Hoff law constant	$1.3 * 10^{-2}$	$[\frac{1}{s\ \mathrm{MPa}^n}]$
α	Thermal diffusivity [17]	$3 * 10^{-6}$	$[\frac{m^2}{s}]$
β	Total compressibility	$3.5 * 10^{-10}$	$[Pa^{-1}]$
β_b	Brine compressibility [7]	$2.3 * 10^{-10}$	$[Pa^{-1}]$
β_s	Sump compressibility [4]	$.82 * 10^{-10}$	$[Pa^{-1}]$
C_b	Brine heat capacity [17]	3840	$[\frac{W}{\mathrm{kg}°\mathrm{C}}]$
C_s	Salt heat capacity [17]	926	$[\frac{W}{\mathrm{kg}°\mathrm{C}}]$
c_f	Fluid sound velocity	1865	$[\frac{m}{s}]$
c_{sat}	Saturated concentration [27]	$53 * 10^3$	$[\frac{mol}{m^3}]$
D_{ab}	Salt mass diffusivity coeff. [28]	$0.12 * 10^{-9}$	$[\frac{m^2}{s}]$
E	Young's modulus of halite	$2 * 10^{10}$	$[Pa]$
γ_b	Volumetric expansion [17]	$4.4 * 10^{-4}$	$[°\mathrm{C}^{-1}]$
g	Acceleration of gravity	9.81	$[\frac{m}{s^2}]$
K_s	Permeability of rock [20]	10^{-19}	$[m^2]$
K_s^{th}	Thermal conductivity [17]	6	$[\frac{W}{m°\mathrm{C}}]$
n	Norton-Hoff law exponent	3.6	$[-]$
η_b	Dynamic viscosity (brine) [2]	$1.2 * 10^{-3}$	$[Pa.s]$
P_∞	Lithostatic pressure	$5.8 * 10^7$	$[Pa]$
ΔP	Pressure increase in cavern	$10 * 10^5$	$[Pa]$
ψ^o	Leak constant rate [1]	10^{-17}	$[\frac{m^3}{m^3 Pa.s}]$
$\frac{Q}{R}$	Norton-Hoff law constant	6201	$[K]$

ρ_b	Brine density	1265	$[\frac{kg}{m^3}]$
T_o	Initial brine temperature	60	[℃]
T_∞	Geothermal temperature [16]	86.5	[℃]

Creep is the most sensitive parameter affecting the mechanical volume. Creep varies drastically with the Norton-Hoff empirical parameters.

$$A^* = A\, e^{-\frac{Q}{RT\infty}} \quad (44)$$

In equation (44) the geothermal temperature T_∞ is in $Kelvin$. The values for A can very from $0.64\ /yMPa^n$ (Etrez cavity) to $2.7 * 10^5\ /yMPa^n$ (Salina), [6]. The coefficient Q/R will vary between $4100\ K$ (Etrez) to $9810\ K$ (Palo Duro).

Figure 7 and Figure 8 display the impact of different empirical values in mechanical volume (creep) contributions.

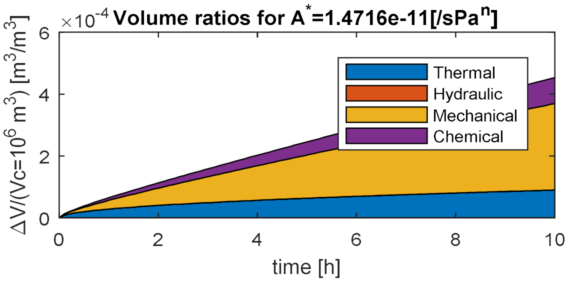

Figure 7 Sum of volume fractions for thermal, hydraulic, mechanical and chemical factors; for a high creep constant $(A^* = 1.47 * 10^{-11}\ s^{-1}Pa^{-n})$ scenario as maximum observed in BAS3O and BAS4 field data.

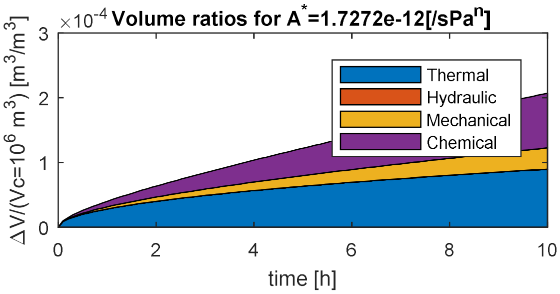

Figure 8 Sum of volume fractions for thermal, hydraulic, mechanical and chemical factors; for a low creep constant $(A^* = 1.73 * 10^{-12}\ s^{-1}Pa^{-n})$ scenario as minimum observed in BAS3O and BAS4 field data.

Observe that the hydraulic volume contribution is extremely small during the test for any of the models, for the case of a $10\ bar$ pressure build-up in the cavern. This can change if leaking rates or permeation become significant.

However, the added volume that most severely impacts the cavern volume estimation during the test is the thermally added volume, since chemical and mechanical volumes are supressed by the compressibility factor in the proposed model, as shown in equation (39).

The compressibility factor impact on the pressure reading is displayed in Figure 9.

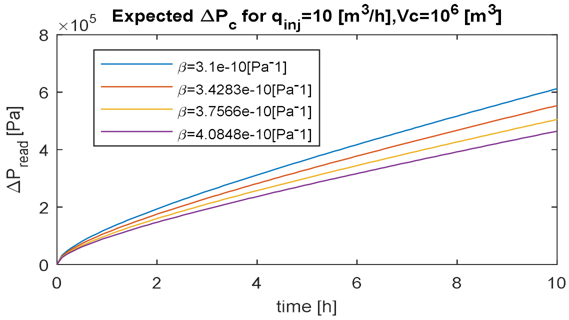

Figure 9 Compressibility factor impact in pressure reading during the test according to proposed model.

Another important aspect is that cavern volume is important in defining a representative injection volume during the test. The higher the pressure increase, the less susceptible are the readings to equipment inaccuracies (for instance due to unreliable calibration) and the effects of fluid density changes due to cooling or heating on the translation of surface pressures to cavern pressures.

Supposing a target of $10\ bar$ pressure increase in a cavity of compressibility of $\beta = 3.3 * 10^{-10}\ Pa^{-1}$, the necessary injected volume as a function of cavern size is plotted in Figure 10.

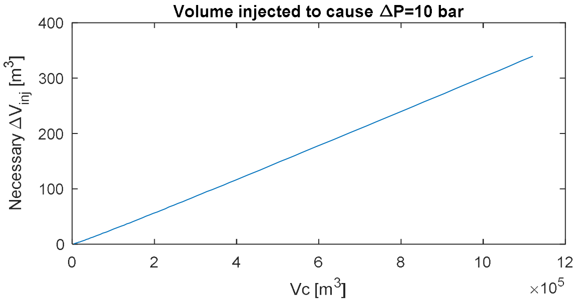

Figure 10 Injection volume to cause $10\ bar$ pressure increase in a $3.3 * 10^{-10}\ Pa^{-1}$ compressible cavern as a function of cavern volume.

As the cavern compressibility increases, the line inclination also increases, and the higher will be the volume necessary for the same pressure increase. The opposite occurs for a lower compressibility case. This also plays a role in defining the injection limits due to design pressure limits of the system. Once pressure build-up inside the cavity reaches operational design limits the test must be interrupted.

Another important datum to be estimated for the test is the cavity equivalent radius, which is unknown before the test. The cavity equivalent radius is given by $R_c = \left(\frac{3}{4\pi}V_C\right)^{1/3}$, where V_c is the cavity volume.

The radius must then be obtained from estimations from production volume balance data, leaching simulators or echo measurements. The impact of this unknown in the finally obtained cavern volume from the model is assessed in Figure 11.

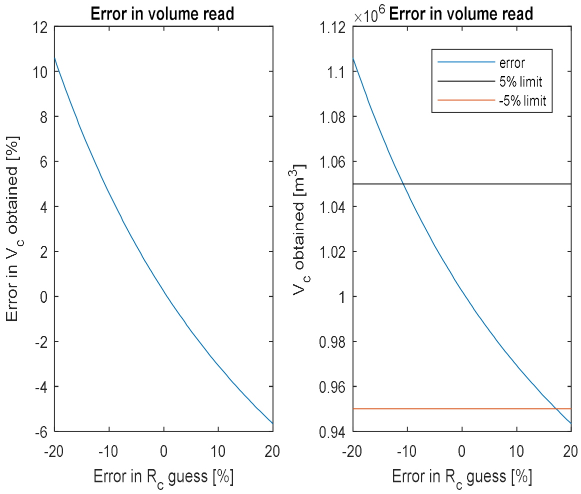

Figure 11 Error caused by wrong prediction of cavern equivalent radius in a spherical cavern size case, for the case of a $10\ hours$ *long test with total* $10\ bar$ *build-up.*

The picture shows that the error is within acceptable limits for an uncertainty on the cavern radius of up to 17% for a 10 hours long test. For shorter period of test the error reduces.

The error is linked to the fact that the cavern radius is of importance to the chemical, thermal (in the characteristic time) and hydraulic term. However, the only term with significant impact in the model is the thermal impact. A wrong estimation on cavern radius impacts the thermal characteristic time, causing the error in measured cavern volume.

5. Case study results

One of the biggest challenges in applying volume prediction models from compressibility testing is that in situ data are rare, and input parameters of the constitutive relations are uncertain. These parameters can be measured in laboratory, nevertheless they are scale dependent and it is not clear is they are useful for field prediction. An example of is the uncertainty on the Norton-Hoff law parameters, also the lack of in situ pressure measurements.

As mentioned in section 4.2 the pressure readings are impacted by cooling of the piping fluid affecting the density and therefore the pressure reading.

The model has been tested to obtain cavern volumes from BAS3O and BAS4 cavities in Zechstein formation, composed of 95% Halite rock. Insoluble material present in the cavities is mainly Anhydrite, which is deposited deposit at the sump.

Pressure data from compressibility tests has been used. The procedures consist of injection low amounts of fresh water into the production string and is also referred to as counter flush as it washes out crystals in production piping. The available measurements included temperature and pressure at central tubing, annular and outer annular (blanket) strings. The test duration varies from three to ten hours, allowing enough time for the secondary effect to take place. Also, the volumes injected are significantly small when compared to the total cavern volume.

5.1. BAS3O

Previous literature has been applied and parameters were calibrated to obtain the best fit volume prediction when compared to known cavern volumes. The impact of the sump and diesel cooling have been included to improve results.

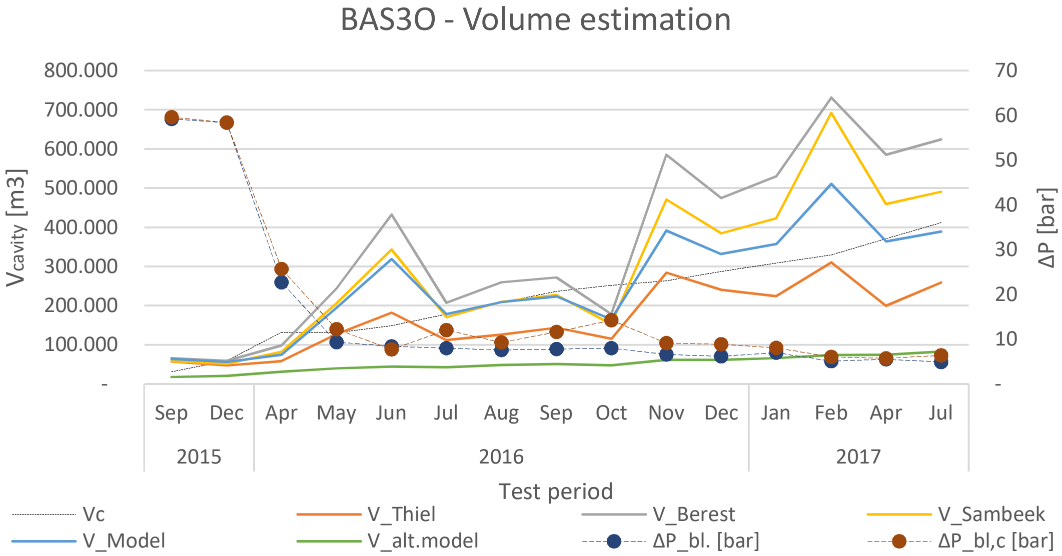

Figure 12 Cavern volume estimation for different models compared to known cavern volume (Vc), BAS3O.

The results are discussed and interpreted in detail in appendix E. From the plot, Figure 12, it is visible that the data for BAS3O are scattered. The proposed model is referred as V_m in the plot.

The cavern volume predictions using Van Sambeek and Bérest models are overestimated, because these models include secondary volumes, such as creep, as part of the injection represented by the LHS of equation (34). Meanwhile, in the proposed model the change of cavity radius due to creep and salt dissolution is on the RHS of equation (34) and here it is multiplied by the compressibility factor.

Another important difference in the models is that Van Sambeek and Bérest take the dissolution as a result of pressure increase only, which is not true for active leaching caverns.

When compared to Thiel's relationship the proposed model has the thermally added volume as the main reason for distinction in results. Indeed, the proposed model is very sensitive to assumed brine average temperature.

The peaks in the volumes obtained may be inferred as test failures or uncertainty on input parameters. In these circumstances the test must be repeated, and the parameters calibrated. Causes for test failure are untracked leaks or wrong estimation of the brine temperature and compressibility.

An alternative to in situ temperature measurements would be to the use of more accurate predictive model temperature difference between produced and in situ brine.

On the other hand, leakages can be spotted by pressure fluctuations (or pressure drop at well head gauges. This is a plausible hypothesis for BAS3O issues, since its well is a side track with complex completions and fittings.

Also, observe that the pressure increase inferred in the cavity jumps down in May 2016. This is an indication of a great change in hydraulic response caused by change in one or more process parameters, for e.g. cavern compressibility or creep. The operator clarified that in May 2016 a workover operation took place, and the cavern operating pressure increased by about $20\ bar$.

5.2. BAS4

Pressure data from BAS4 are also analysed. The cavern is on production since 2006 and shows a nearly steady state production behaviour (when squeeze volumes equals to salt production).

Due to extensive leaching the cavity has a significant volume of sump when compared to BAS3O, which is accounted for in the total cavern compressibility for all models. The results are presented Figure 13.

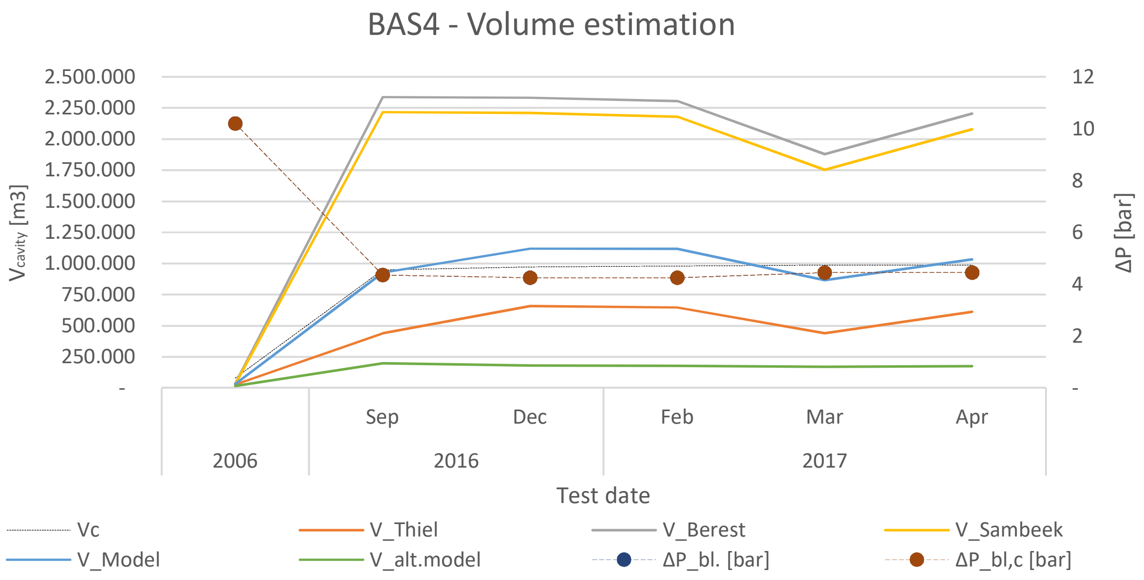

Figure 13 Cavern volume estimation for different models compared to known cavern volume (Vc), for BAS4

In the case of BAS4 the data show less scatter data than that of BAS3O cavern, since the system presents less uncertainty and variations in input parameters (for example the brine temperature due to the long time that cavern is under production).

For the case of BAS4 the proposed model is the only one to reach values close to the forecasted volume (which fits sonar survey estimated cavern volume). The reason for that is the underestimation of chemical volume from Bérest and Van Sambeek approach, which is proposed for idle cavities, but also once again (as in BAS3O results) due to the incorporation of creep as added volume in the LHS of equation (34).

Thiel's model on the other hand underestimates the volume by not considering secondary effects volumes. However, Thiel's model gives consistent results and may be applied with a constant correction factor for BAS4. This remark does not mean that the model is correct but rather that there is a quantity, not identified by Thiel, of that order of magnitude.

The proposed model although nearer to forecasted volumes yet gives results above desirable error margin of 5%. The issue once again may be caused by wrong in situ brine temperature estimation or test failure.

6. Conclusion

Cavern compressibility models fail to obtain accurate cavern volumes for deep caverns in active solution mined caverns. However, in some cases accurate results are obtained with Thiel's model which can be calibrated with constant correction factor, what explicit shows that essential mechanisms are missing in the model.

The proposed model focusses on caverns under active leaching, and therefore it shall be tested if it is applicable for idle caverns. Also, the model has only been tested for moderate test durations (three to ten hours).

In summary the proposed model can only reach an accuracy of up to 10% by eliminating unreliable data set, as in appendix E. The unreliable data set can be tracked as peaks when compared with cavern volume forecast, where error is too great meaning that the model did not deliver reliable results. The reason for these peaks is still unknown.

Furthermore, this study presents useful comparison between different existing models for compressibility-based cavern volume estimation and brings a new point of view to the issue of active leaching caverns. It is one step forward to understanding how to improve compressibility test analysis for deep salt caverns to obtain cavern volume estimations.

6.1. Discussion

In all models the sensitivity of the volume relies on the cavern compressibility. The difference is in the way secondary effects are or not accounted for, and how they are taken into account.

If creep and is accounted for as injected volume the cavern volume is significantly overestimated. Also, if the cavern volume change due to chemical dissolution must be calculated for a situation of undersaturated brine for the case of active caverns, instead of additional dissolution caused by pressure build-up only.

In Thiel's method secondary effects are neglected. Bérest and Van Sambeek present the secondary effects, or salt cavern phenomena, volumes as part of the injected volume, hence leading to overestimations. The proposed model is different from the referred previous models because it takes creep (mechanical) and dissolution volume changes as part of the volume change of the cavity space instead; and takes thermal and leak volumes as part of injection.

In the Bérest and Van Sambeek approach the volumes added by creep and thermal expansion are significant to obtain cavern volume. Meanwhile, in the proposed model creep is suppressed, leaving cavern compressibility and thermal impact as the main contributors to pressure response.

The main pitfall in Thiel's model when compared to the other options, is that it does not admit a cavern pressure build-up in the absence of injection. This can only be true in a static condition, which does not occur since the system is dynamic with continuous influence of other phenomena.

The proposed model's fails to deliver results within 5% accuracy, and it is yet unclear the reason for the error in cavern volume estimations. Nevertheless, the proposed model achieves the desired 5% accuracy in 8 of 20 data sets.

The mean absolute percentage error of the proposed model is 32% for BAS3O and 12% for BAS4, what is lower than that of Thiel (33% and 43%), Van Sambeek (45% and 114%) and Bérest (66% and 127%). Further studies to mitigate uncertainties (such as lab experiments and controlled tests) are necessary to improve existing methods.

The work here differs from previous work that it presents a comprehensive description of the various methods used in the literature and practice. Where current models predict cavity volumes with a maximum accuracy of 33%, the model here, which includes the presence of insoluble particles, and a well-established creep model is able to predict cavity volumes to an accuracy of 12%.

6.2. Recommendations

The data set used for compressibility-based volume estimation come from counter flush operations, which have a low injection rate of $10\,m^3/h$. The impact of such small injection volumes when compared to other phenomena involved needs to be studied. An attempt to investigate this issue was done by applying in total three tests with high injection rates of $100\,m^3/h$ and $180\,m^3/h$ for $2\,hours$ in both wells. The results were inconclusive, and more data is necessary to perform an analysis on the impact of injection volume in pressure readings. However, it was observed that the system tends to a linear trend after a certain amount of time (which varies) in all three tests.

This model can be tested to shut-in conditions without fluid injection for validation under slow pressure increase. Implementation of this scenario requires that the model parameters be extremely accurate, and it may be useful to find unknown (or uncertain) variables from history matching.

Thermal impact on applied models is assumed to be an added volume, however a more accurate approach would be to take it as change in brine density and therefore total cavern brine volume.

It is recommended to test this alternative approach obtained from the mass-volume relationship inside the cavern, as shown in detail in appendix A and discussed in appendix F. The alternative method is based on mass balance as below, for the case of significant blanket volume.

$$V = \frac{\Delta V_{inj}}{\Delta P_c}\left(\frac{\rho_b}{\rho_f}\right)\left\{\beta - \frac{1}{\Delta P_c}\left[\frac{\Delta V_{mc}}{V} - \frac{\Delta V_{ch}}{V}\left(1 + \frac{\rho_s}{\rho_b}\right) + \frac{\Delta V_{th}}{V}\left(\frac{1}{1+\gamma_b \Delta T}\right)\right]\right\}^{-1}, \qquad (45)$$

which can also be re-written as;

$$V = \frac{\Delta V_{inj}}{\Delta P_c}\left(\frac{\rho_b}{\rho_f}\right)\left\{\beta - \frac{1}{\Delta P_c}\left[\frac{\Delta V_{mc}}{V} - \frac{\Delta V_{ch}}{V}\frac{\rho_b+\rho_s}{\rho_b} + \frac{\gamma_b \Delta T}{1+\gamma_b \Delta T}\right]\right\}^{-1}. \tag{46}$$

The solutions disregards permeation effects since it has been proven to be negligible for salt rock, and leaks can be incorporated by subtraction from the injected volume.

Other phenomena such as rock cooling impact in pressure response in active leaching cavities is also unclear. The mechanical and thermal terms of all models assume a constant rock temperature, what may not be true, and needs yet to be studied.

Acknowledgment

The author would like to recognize prof Hans Bruining from TU Delft and Peter Fokker from WEP B.V. for their insightful inputs for the elaboration of this work. Also, WEP B.V. and Frisia Zout for sponsoring the study and providing a vast data set.

Nomenclature

	Parameter	Unit
A	Norton-Hoff law constant	$[\frac{1}{s\ Pa^n}]$
A^*	Norton-Hoff law constant	$[\frac{1}{s\ Pa^n}]$
A_c	Salt cavern surface area	$[m^2]$
β	Total cavern compressibility	$[Pa^{-1}]$
β_b	Brine compressibility	$[Pa^{-1}]$
β_c	Cavity elastic deformation	$[Pa^{-1}]$
β_d	Diesel compressibility	$[Pa^{-1}]$
β_f	Fluid compressibility	$[Pa^{-1}]$
β_{ins}	Insoluble rock compressibility	$[Pa^{-1}]$
β_s	Sump compressibility	$[Pa^{-1}]$
C_b	Brine heat capacity	$[\frac{W}{\text{kg°C}}]$
C_s	Salt heat capacity	$[\frac{W}{\text{kg°C}}]$
$\mathbf{c}$	Salt concentration vector	$[\frac{kg}{m^3.m}]$
c	Salt concentration in brine	$[\frac{kg}{m^3}]$
c_o	Initial salt concentration in brine	$[\frac{kg}{m^3}]$
c_f	Fluid sound velocity	$[\frac{m}{s}]$
c_{sat}	Salt concentration at saturation	$[\frac{mol}{m^3}]$
c_t	Total formation compressibility	$[Pa^{-1}]$
χ	Thermal capacity ratio	$[-]$
D_{ab}	Salt mass diffusivity coefficient	$[\frac{m^2}{s}]$
E	Young's modulus of the rock	$[Pa]$
ε	Strain	$[\frac{m^3}{m^3}]$
$\dot{\varepsilon}_{ss}$	Steady-state creep rate	$[\frac{m^3}{m^3 s}]$
ϑ	Poisson's ratio of the rock	$[-]$
F	Shape factor	$[-]$
G	Shear modulus	$[-]$
Gr	Grashof number	$[-]$
γ_b	Brine volumetric expansion	$[\frac{m^3}{m^3 °C}]$
γ_d	Diesel volumetric expansion	$[\frac{m^3}{m^3 °C}]$
g	Acceleration of gravity	$[\frac{m}{s^2}]$
H	Cylindrical cavity height	$[m]$
H_{ann}	Annular tubing vertical depth	$[m]$
h, L_c	Characteristic length of sphere	$[m]$
J	Transfer rate	$[\frac{kg}{s}]$
K_s	Permeability of salt formation	$[m^2]$
K_s^{th}	Thermal conductivity of salt	$[\frac{W}{m°C}]$
k_s^{th}	Thermal diffusivity of salt	$[\frac{m^2}{s}]$
k	Convective mass transfer coef.	$[\frac{m}{s}]$
M	Mass of brine in the cavity	$[kg]$
m	Mass of brine injected	$[kg]$
μ	Lamé's constant	$[Pa]$
N	Mass transfer per unit area	$[\frac{kg}{m^2}]$
n	Norton-Hoff law exponent	$[-]$
v	Kinematic viscosity	$[\frac{m^2}{s}]$
η_b	Dynamic viscosity of brine	$[Pa.s]$
P_∞	Lithostatic pressure	$[Pa]$
P_c, P	Pressure inside cavern	$[Pa]$
P_o	Pore pressure (halmostatic)	$[Pa]$
ΔP_c	Cavern pressure build-up	$[Pa]$
δP_{th}	Tubing head pressure correction	$[Pa]$
φ	Salt porosity	$[-]$
ψ	Leak constant	$[\frac{m^3}{Pa.s}]$

ψ^o	Leak constant per cavern volume	$[\frac{m^3}{m^3 Pa.s}]$
$\frac{Q}{R}$	Norton-Hoff law constant	$[K]$
$R_\infty . r_\infty$	Radial distance to aquifer	$[m]$
R_c, R	Cavity equivalent radius	$[m]$
r	Radial distance from cavity	$[m]$
ρ_b	Brine density	$[\frac{kg}{m^3}]$
ρ_b^f	Final brine density after test	$[\frac{kg}{m^3}]$
ρ_b^o	Initial brine density before test	$[\frac{kg}{m^3}]$
ρ_d^f	Final diesel density	$[\frac{kg}{m^3}]$
ρ_d^o	Initial diesel density	$[\frac{kg}{m^3}]$
ρ_d	Diesel density	$[\frac{kg}{m^3}]$
ρ_f	Fluid average density	$[\frac{kg}{m^3}]$
$\Delta\rho_f$	Fluid average density change	$[\frac{kg}{m^3}]$
$\boldsymbol{\sigma}$	Stress tensor	$[Pa]$
σ_{eff}	Effective stress	$[Pa]$
SH^*	Maximum horizontal stress	$[Pa]$
Sh^*	Minimum horizontal stress	$[Pa]$
Sh	Sherwood number	$[-]$
Sc	Schmidt number	$[-]$
T, θ	Cavern fluid temperature	$[°C, K]$
T_o, θ_o	Initial cavern fluid temperature	$[°C, K]$
$T_\infty, \theta_R^\infty$	Rock geothermal temperature	$[°C, K]$
t	Test duration, time	$[s]$
t_c^{th}	Characteristic thermal time	$[s]$
u	Radial dislocation (deformation)	$[m]$
V	Cavern volume	$[m^3]$
V^o	Initial cavern volume (before test)	$[m^3]$
V^f	Final cavern volume (after test)	$[m^3]$
ΔV	Cavity volume change	$[m^3]$
ΔV_{ch}	Cavity dissolved volume	$[m^3]$
$\Delta V_{cr}, \Delta V_{mc}$	Cavity deformation volume	$[m^3]$
ΔV_{hy}	Hydraulic volume loss	$[m^3]$
ΔV_{inj}	Injected volume	$[m^3]$
ΔV_{leak}	Leaked volume	$[m^3]$
ΔV_{ad}	Total added volume	$[m^3]$
WHP	Wellhead pressure	$[Pa]$
x_d	Diesel fraction in cavity volume	$[-]$
x_{ins}	Insoluble fraction in sump volume	$[-]$
λ	Lamé's constant	$[Pa]$
y	Open cavity volume fraction	$[-]$

References

[1] P. Bérest, M. Karimi-Jafari, B. Brouard and G. Durup, "Brine warming in a sealed cavern: what can be done?," in *SMRI Fall Conference 2006*, Rapid City, South Dakota, USA, (2006).

[2] P. A. Fokker, "The behavior of salt and salt caverns," Technische Universiteit Delft (TU Delft), Delft, ISBN 90-007953, (1995).

[3] N. G. Crossley, "Sonar surveys used in gas-storage cavern analysis," *Oil & Gas Journal,* vol. 96, no. 18, 5 April ISSN: 0030-1388, (1998).

[4] K. Lux, "Design of salt caverns for the storage of natural gas, crude oil and compressed air: Geomechanical aspects of construction, operation and abandonment," *Geological Society,* p. 313, DOI: 10.1144/SP3137, (2009).

[5] W. R. Thiel, "Precision method for testing the integrity of soluciton mined underground storage caverns.," vol. 1, pp. 377-383, (1993).

[6] L. L. Van Sambeek, P. Bérest and B. Brouard, "Improvements in mechanical Integrity tests for solution-mined caverns used for mineral production of liquid-product storage," SMRI, (2005).

[7] P. Bérest, J. Bergues and B. Brouard, "Review of Static and Dynamic Compressibility Issues Relating to Deep Underground Salt Caverns," *International Journal of Rock Mechanics and Mining Sciences 36,* p. 1031±1049, DOI: 10.1016/S0148-9062(99)00062-5, (1999).

[8] P. Bérest, B. Brouard, P. Bergues, J. Frelat and G. Durup, "Salt caverns and compressibility factor," in *SMRI Fall Meeting*, El Paso, TX, (1997).

[9] S. Sobolik and B. Ehgartner, "Analysis of Cavern Shapes for the Strategic Petroleum Reserve," Sandia National Laboratories, Albuquerque, New Mexico, Code: SAND2006-3002, (2006).

[10] S. Grandi, R. Rao and M. N. Toksöz, "Geomechanical Modeling of In-Situ Stresses Around a Borehole," *MIT Earth Resources Laboratory,* (2002).

[11] J. Jaeger, N. Cook and R. Zimmerman, Fundamentals of Rock Mechanics, Methuen, ISBN-13: 978-0632057597, (1969).

[12] A. Heim, Untersuchungen über den Mechanismus der Gebirgsbildung im Anschluss an die geologische Monographie der Tödi-Windgällen-Gruppe, Basel: ETH-Bibliothek Zürich, DOI: 10.3931/e-rara-19575, (1878).

[13] F. Crotogino, "Salt Cavern In-Situ Testing from the constructor's and from the operator's viewpoint," in *1st Conf. Mech. Behavior of Salt*, (1981).

[14] G. Crost, "Geomechanical properties of a blackfill material suitable for stabilising salt caverns in Twente," TU Delft, (2012).

[15] W. R. Thiel, "Method of determining the volume of a section of an underground cavity". United States of America Patent 4720995, 26 January (1988).

[16] B. Brouard, "On the behavior of solution-mined caverns, theorical study and in situ experimentation [in French]," Ecole Polytechnique, Palaiseau, France, (1998).

[17] M. Karimi-Jafari, "Sur le comportement transitoire des cavités salines profondes," OCLC: 869711906, (2007).

[18] P. Bérest, M. Karimi-Jafari, B. Brouard and B. Bazargan, "In situ Mechanical Tests in Salt Caverns," in *Spring Technical Meeting*, Brussels, (2006).

[19] L. Dake, Fundamentals of reservoir engineering, Elsevier B.V., ISBN: 9780444418302, (1978).

[20] J. G. Durup, "Long term tests for tightness evaluation with brine and gas in salt," in *SMRI Spring Meeting*, Houston, DOI: 10.2516/ogst:2001037, (1994).

[21] D. A. Duquesnoy, "Issues pertinent to the abandonment BAS1 and BAS2," WEP B.V., (2017).

[22] B. L. Ehgartner and J. K. Linn, "Mechanical behavior of sealed SPR caverns," in *SMRI Fall Meeting*, Houston, TX, (1994).

[23] S. Timoshenko and J. Goodier, Theory of Elasticity, McGraw-Hill Book Company Inc., ISBN-10: 0070701229, (1934).

[24] A. J. Russo, "Solution mining calculations for SPR caverns," in *Sixth International Symposium on Salt*, (1983).

[25] R. Bird, W. Stewart and E. Lightfoot, Transport Phenomena, ISBN: 0-471-07392-X, (1960).

[26] W. J. Beek and K. M. K. Muttzall, Transport Phenomena, Wiley, ISBN-10: 0471999903, (1975).

[27] "Density of aqueous solutions of inorganic sodium salts," Engineering ToolBox, 2017. [Online]. Available: https://www.engineeringtoolbox.com/density-aqueous-solution-inorganic-sodium-salt-concentration-d_1957.html. [Accessed 24th August 2018].

[28] "MASS DIFFUSIVITY DATA," Isidoro Martinez, 2018. [Online]. Available: http://webserver.dmt.upm.es/~isidoro/dat1/Mass%20diffusivity%20data.pdf. [Accessed 24th August 2018].

[29] H. S. Carslaw and J. C. Jaeger, Conduction of heat in solids, ISBN 10: 0198533683, (1959).

[30] P. Bérest, B. Brouard and J. Couteau, "Influence of the leaching phase on the mechanical behavior of salt caverns," in *36th US Rock Mechanics Symposium, ISRM*, DOI: 10.1016/S1365-1609(97)00019-1, (1997).

[31] J. H. VanSant, Conduction Heat Transfer Solutions, Lawrence Livermore National Laboratory, (1980).

[32] L. Landau and E. Lifshitz, Theory of elasticity, Pergamon Press, ISBN: 9780080570693, (1951).

[33] L. Malvern, Introduction to the mechanics of a continuous medium, Prentice-Hall, Inc., ISBN: 9780134876030, (1969).

[34] G. Kirsch, Die Theorie der Elastizität und die Bedürfnisse der Festigkeitslehre, Springer, (1898).

[35] E. Anderson, The dynamics of faulting and dyke formation with applications to Britain., Edinburgh, Oliver and Boyd, (1951).

[36] P. Bérest and B. Brouard, "Behavior of sealed solution-mined caverns," in *SMRI Spring Meeting*, New Orleans, (1995).

[37] P. Bérest, J. F. Beraud and V. de Greef, "Creep closure rate of shallow cavern," in *SMRI Spring Meeting*, Galveston, ISBN 978-0-415-80444-8, (2011).

[38] P. Bérest, B. Brouard and J. G. Durup, "Shut-in pressure test, Case studies," in *SMRI Fall Meeting*, (2000).

[39] P. Bérest, B. Brouard and G. Durup, "Tightness Test in Salt-Cavern Wells," in *SMRI Spring Meeting*, Banff, Alberta, Canada, DOI: 10.2516/ogst:2001037, (2002).

[40] M. Jeremic, Rock Mechanics in Salt Mining, CRC Press, ISBN: 9054101032, (1994).

[41] J. Li, X. Shi, C. Yang, Y. Li, T. Wang and H. Ma, "Mathematical model of salt cavern leaching for gas storage in high-insoluble salt formations," Scientific Reports, DOI: 10.1038/s41598-017-18546-w, (2018).

[42] T. Wang, X. Z. Yan, X. J. Yang and H. L. Yang, "Dynamic subsidence prediction of ground surface above salt cavern gas storage considering the creep of rock salt," *Science China Technological Sciences,* vol. 53, no. 12, pp. 3197-3202, December DOI: 10.1007/s11431-010-4172-4, (2010).

Appendix A – Compressibility test

The correlation obtained by Thiel for compressibility test is based in a mass-volume relationship to accommodate the injected volume in the cavern, [7] [15]. To obtain a solution is assumed that brine density and compressibility is uniform inside the cavern. If the cavern contains different fluids, such as blanket, then the density and compressibility of the combined fluid is taken.

In this section Thiel's model and the proposed model for compressibility-based volume estimation is obtained.

A.1. Pressure build-up relationship (Thiel's model)

According to the solution proposed by Thiel's the cavity pressure response is only being impacted by fluid compressibility (assumed to be constant) and injection volume. To obtain Thiel's relationship we must assume a brine and diesel filled cavern, [7]. The total mass within the cavern is then;

$$M = \rho_f V = [x_d \rho_d + (1 - x_d)\rho_b]V. \tag{A. 1}$$

where; ρ_f is the fluid average density, V the cavern volume, x_d the diesel fraction, and ρ_b the brine density. As the cavern deforms elastically under pressure change, the added volume in the cavity will be;

$$\Delta V = \beta_c \Delta P_c V. \tag{A. 2}$$

where, β_c is the cavity compressibility (assuming isentropic behaviour) and ΔP_c the pressure build-up in the cavern. If an additional mass of brine, m, is forced into the cavern we obtain;

$$m = \rho_b \Delta V_{inj}. \tag{A. 3}$$

The pressure increases by the following mass-volume relationship, including fluid density variation $\Delta\rho_f$;

$$M + m = \rho_f(V + \Delta V) + \Delta\rho_f(V + \Delta V). \tag{A. 4}$$

Substituting (A.1) and (A.3) into equation (A.4) we obtain:

$$\rho_b \Delta V_{inj} = \rho_f \Delta V + \Delta\rho_f V + \Delta\rho_f \Delta V. \tag{A. 5}$$

The variation in fluid density is defined as function of cavern pressure and fluid average compressibility by:

$$\Delta\rho_f = \rho_f \beta_f \Delta P_c \tag{A. 6}$$

and;

$$\beta_f = x\beta_d + (1 - x)\beta_b. \tag{A. 7}$$

Substituting (A.6) into equation (A.5) we obtain:

$$\frac{\rho_b \Delta V_{inj}}{\rho_f} = \beta_f \Delta P_c V + (1 + \beta_f \Delta P_c)\Delta V. \tag{A. 8}$$

Substituting (A.2) into equation (A.8) we obtain:

$$\frac{\Delta V_{inj}}{V} = \frac{\rho_f}{\rho_b}[\beta_f + \beta_c + \beta_c \beta_f \Delta P_c]\Delta P_c, \tag{A. 9}$$

where the factor $\beta_c \beta_f \Delta P_c^2$ is assumed to be nearly zero, and:

$$\frac{\Delta V_{inj}}{V} = \Delta P_c \frac{\rho_f}{\rho_b}\left(\beta_f + \beta_c\right). \tag{A. 10}$$

For the case where diesel volume is much smaller than that of the brine ($\frac{\rho_f}{\rho_b} \rightarrow 1$), the equation (A.10) can be simplified resulting in;

$$\frac{\Delta V_{inj}}{V} = \Delta P_c\left(\beta_f + \beta_c\right) = \Delta P_c \beta. \tag{A. 11}$$

This relationship gives the pressure build-up due to injected volume only. This is only accurate for a short enough test so that other effects do not impact the readings.

A.2. Proposed model for pressure build-up

The cavern pressure build-up is not only a consequence of the volume injected in the cavern, but also from other volume contributions. The equation is then better re-written as:

$$\frac{\Delta V_{ad}}{V^f} = \beta \Delta P_c, \tag{A. 12}$$

where, V^f is the final cavern volume at the end of the test, and ΔV is different from the previous equation. Here ΔV_{ad} refers to the total added volume, including injection, thermal expansion and subtracting hydraulic volume losses. The components are replaced by identified volumetric changes in the cavern;

$$\Delta V_{ad} = \Delta V_{inj} + \Delta V_{th} - \Delta V_{hy}\ , \tag{A. 13.a}$$

and

$$V^f = V^o + \Delta V_{ch} - \Delta V_{mc}. \tag{A.13.b}$$

Then, by substituting (A.13.a) and (A.13.b) in the equation (A.12) the following equations is obtained;

$$\Delta V_{inj} + \Delta V_{th} - \Delta V_{hy} \ = \beta \Delta P_c (V^o + \Delta V_{ch} - \Delta V_{mc}) \tag{A. 14}$$

Where, V^o is the initial cavern volume before the test. The equation is re-written by isolating $\frac{\Delta V_{inj}}{V^o}$ in LHS.

$$\frac{\Delta V_{inj}}{V^o} = \beta \Delta P_c \left(1 + \frac{\Delta V_{ch}}{V^o} - \frac{\Delta V_{mc}}{V^o}\right) - \left(\frac{\Delta V_{th}}{V^o} - \frac{\Delta V_{hy}}{V^o}\right). \tag{A. 15}$$

Reciprocal to the previous equation the relationship can be re-written by isolating $\frac{\Delta V_{inj}}{\Delta P_c}$ in LHS, which has as advantage that the right side consists of measured parameters. So, we obtain;

$$\frac{\Delta V_{inj}}{\Delta P_c} = \beta (V^o + \Delta V_{ch} - \Delta V_{mc}) - \left(\frac{\Delta V_{th}}{\Delta P_c} - \frac{\Delta V_{hy}}{\Delta P_c}\right). \tag{A. 16}$$

Once each volume component is dependent on cavern volume, it is useful to write the equation (A.16) as;

$$\frac{\Delta V_{inj}}{\Delta P_c} = \beta V^o \left(1 + \frac{\Delta V_{ch}}{V^o} - \frac{\Delta V_{mc}}{V^o}\right) - \left(\frac{\Delta V_{th}}{\Delta P_c} - \frac{\Delta V_{hy}}{\Delta P_c}\right). \tag{A. 17}$$

Isolating the target variable, the unknown volume we obtain:

$$\frac{\Delta V_{inj}}{\Delta P_c} = V^o \left[\beta \left(1 + \frac{\Delta V_{ch}}{V^o} - \frac{\Delta V_{mc}}{V^o}\right) - \frac{1}{\Delta P_c}\left(\frac{\Delta V_{th}}{V^o} - \frac{\Delta V_{hy}}{V^o}\right)\right]. \tag{A. 18}$$

Hence, the cavern volume is;

$$V^o = \frac{\Delta V_{inj}}{\Delta P_c}\left[\beta\left(1 + \frac{\Delta V_{ch}}{V^o} - \frac{\Delta V_{mc}}{V^o}\right) - \frac{1}{\Delta P_c}\left(\frac{\Delta V_{th}}{V^o} - \frac{\Delta V_{hy}}{V^o}\right)\right]^{-1} \qquad \text{(A. 19)}$$

Although the cavern volume V^o appears on the right side of the equation (A.19) this will be eliminated since, as in appendix B, each contributing volume is dependent of V^o, so dividing each of them by V^o is useful.

A.3. Mass-volume alternative model for pressure build-up

An alternative method can be proposed using the same principal as Thiel and incorporating the secondary effects. This is an alternative model based on mass-volume relationship to estimate cavity pressure response. Now the correlation is not only being impacted by the injected volume and compressibility, but also by other phenomena. We once again assume a brine and diesel filled cavern. The total mass within the cavern is then;

$$M = \rho_f V = [x_d\rho_d + (1 - x_d)\rho_b]V. \qquad \text{(A. 20)}$$

A mass change due to chemical dissolution is then added due to mass transfer on the cavern wall;

$$\Delta M_{ch} = \rho_s \Delta V_{ch}, \qquad \text{(A. 21)}$$

where; ρ_s is the salt density and ΔV_{ch} is the volume of salt dissolved. Now the cavern changes elastically under pressure build-up and also due to viscoplastic deformation (creep or mechanical volume) combined with volume increase with salt rock dissolution. The added volume in the cavity will be;

$$\Delta V = \beta_c \Delta P_c V - \Delta V_{mc} + \Delta V_{ch}, \qquad \text{(A. 22)}$$

where, β_c is the cavity compressibility, ΔP_c the pressure build-up in the cavern, ΔV_{mc} is the mechanical reduced volume (caused by creep), and ΔV_{ch} is the dissolved salt volume. If an additional mass of brine is forced into the cavern; $m = \rho_b \Delta V_{inj}$, as in equation (A.3), then the pressure increases by the following mass-volume relationship, including fluid density variation $\Delta\rho_f$;

$$M + \Delta M_{ch} + m = \rho_f(V + \Delta V) + \Delta\rho_f(V + \Delta V). \qquad \text{(A. 23)}$$

Substituting (A.20) into equation (A.23) we obtain,

$$\Delta M_{ch} + m = \rho_f\ \Delta V + \Delta\rho_f(V + \Delta V). \qquad \text{(A. 24)}$$

Substituting (A.3) and (A.21) into equation (A.24) we obtain,

$$\rho_s \Delta V_{ch} + \rho_b \Delta V_{inj} = \rho_f\ \Delta V + \Delta\rho_f(V + \Delta V). \qquad \text{(A. 25)}$$

The variation in fluid density, $\Delta\rho_f$, is defined as function of cavern pressure and fluid average compressibility as in equation (A.7),

$$\Delta\rho_f = \rho_f\beta_f\Delta P_c + \Delta\rho_f^{th} = \rho_f\beta_f\Delta P_c + \rho_f\left(\frac{1}{1+\gamma_b\Delta T} - 1\right). \qquad \text{(A. 26)}$$

Substituting (A.26) into equation (A.25) we obtain

$$\rho_s \Delta V_{ch} + \rho_b \Delta V_{inj} = \rho_f\ \Delta V + \rho_f\left[\beta_f\Delta P_c + \left(\frac{1}{1+\gamma_d\Delta T} - 1\right)\right](V + \Delta V). \qquad \text{(A. 27)}$$

Replacing the term $\left(\frac{1}{1+\gamma_b\Delta T} - 1\right) = \omega_{th}$, the equation can be simplified to

$$\frac{\rho_s}{\rho_f}\Delta V_{ch} + \frac{\rho_b}{\rho_f}\,\Delta V_{inj} = \Delta V + \left[\beta_f \Delta P_c + \omega_{th}\right](V + \Delta V). \tag{A. 28}$$

Substituting (A.22) into equation (A.28), we obtain

$$\frac{\rho_s}{\rho_f}\Delta V_{ch} + \frac{\rho_b}{\rho_f}\,\Delta V_{inj} = \beta_c \Delta P_c V - \Delta V_{mc} + \Delta V_{ch} + \left[\beta_f \Delta P_c + \omega_{th}\right](V + \beta_c \Delta P_c V - \Delta V_{mc} + \Delta V_{ch}). \tag{A. 29}$$

In equation (A.29) the terms $\omega_{th}\beta_c\Delta P_c = \left(\frac{1}{1+\gamma_d(\Delta T_t)} - 1\right)\beta_c\Delta P_c \rightarrow 10^{-1}$ and $\beta_f\beta_c\Delta P_c^2 \rightarrow 10^{-10}$, meanwhile the other terms tend to 10^{-5} order of magnitude. Therefore, the referred terms can be disregarded, and by re-arranging the equation we obtain

$$\frac{\rho_b}{\rho_f}\,\Delta V_{inj} = V\left[(\beta_c + \beta_f)\Delta P_c + \omega_{th}\right] - \Delta V_{mc}\left(1 + \beta_f \Delta P_c + \omega_{th}\right) + \Delta V_{ch}\left(1 + \beta_f \Delta P_c + \omega_{th} - \frac{\rho_s}{\rho_f}\right). \tag{A. 30}$$

Substituting the compressibility $\beta = \beta_f + \beta_c$, we obtain

$$\frac{\rho_b}{\rho_f}\frac{\Delta V_{inj}}{\Delta P_c} = V\left(\beta + \frac{\omega_{th}}{\Delta P_c}\right) - \Delta V_{mc}\left(\frac{1}{\Delta P_c} + \beta_f + \frac{\omega_{th}}{\Delta P_c}\right) + \Delta V_{ch}\left(\frac{1}{\Delta P_c} + \beta_f + \frac{\omega_{th}}{\Delta P_c} - \frac{\rho_s}{\rho_f}\frac{1}{\Delta P_c}\right), \tag{A. 31}$$

where; $\left(\frac{1}{\Delta P_c} \rightarrow 10^{-5}\right) \gg \left(\beta_f + \frac{\omega_{th}}{\Delta P_c} \rightarrow 10^{-1}\right)$ and therefore the term can be dropped out, and the equation becomes

$$\frac{\rho_b}{\rho_f}\frac{\Delta V_{inj}}{\Delta P_c} = V\left(\beta + \frac{\omega_{th}}{\Delta P_c}\right) - \Delta V_{mc}\left(\frac{1}{\Delta P_c}\right) + \Delta V_{ch}\left(\frac{1}{\Delta P_c}\right)\left(1 + \frac{\rho_s}{\rho_f}\right). \tag{A. 32}$$

For the case of blanket volume being much smaller than that of brine then $\frac{\rho_b}{\rho_f} \rightarrow 1$, we obtain

$$\frac{\Delta V_{inj} + \Delta V_{mc} - \Delta V_{ch}\left(1 + \frac{\rho_s}{\rho_b}\right)}{\Delta P_c} = V\left(\beta + \frac{\omega_{th}}{\Delta P_c}\right). \tag{A. 33}$$

Finally, and replacing back $\omega_{th} = \left(\frac{1}{1+\gamma_b\Delta T} - 1\right) = \frac{\gamma_b\Delta T}{1+\gamma_b\Delta T}$ then the equation includes the thermal volume

$$\frac{\Delta V_{inj} + \Delta V_{mc} - \Delta V_{ch}\left(1 + \frac{\rho_s}{\rho_b}\right)}{\Delta P_c} = V\left(\beta - \frac{1}{\Delta P_c}\frac{\gamma_b\Delta T}{(1+\gamma_b\Delta T)}\right). \tag{A. 34}$$

By re-arranging the terms in equation (A.34) we obtain

$$\frac{\Delta V_{inj}}{\Delta P_c} = V\left\{\beta - \frac{1}{\Delta P_c}\left[\frac{\Delta V_{mc}}{V} - \frac{\Delta V_{ch}}{V}\left(1 + \frac{\rho_s}{\rho_b}\right) + \frac{\Delta V_{th}}{V}\left(\frac{1}{1+\gamma_b\Delta T}\right)\right]\right\}, \tag{A. 35}$$

which can be rearranged to

$$V = \frac{\Delta V_{inj}}{\Delta P_c}\left\{\beta - \frac{1}{\Delta P_c}\left[\frac{\Delta V_{mc}}{V} - \frac{\Delta V_{ch}}{V}\left(1 + \frac{\rho_s}{\rho_b}\right) + \frac{\Delta V_{th}}{V}\left(\frac{1}{1+\gamma_b\Delta T}\right)\right]\right\}^{-1}. \tag{A. 36}$$

For the case of blanket volume being significant, then $\frac{\rho_b}{\rho_f} < 1$ equation (A.36) becomes

$$\frac{\Delta V_{inj}}{\Delta P_c}\left(\frac{\rho_b}{\rho_f}\right) = V\left\{\beta - \frac{1}{\Delta P_c}\left[\frac{\Delta V_{mc}}{V} - \frac{\Delta V_{ch}}{V}\left(1 + \frac{\rho_s}{\rho_b}\right) + \frac{\Delta V_{th}}{V}\left(\frac{1}{1+\gamma_b\Delta T}\right)\right]\right\}, \tag{A. 37}$$

Which can be rearranged to

$$V=\frac{\Delta V_{inj}}{\Delta P_c}\left(\frac{\rho_b}{\rho_f}\right)\left\{\beta-\frac{1}{\Delta P_c}\left[\frac{\Delta V_{mc}}{V}-\frac{\Delta V_{ch}}{V}\left(1+\frac{\rho_s}{\rho_b}\right)+\frac{\Delta V_{th}}{V}\left(\frac{1}{1+\gamma_b\Delta T}\right)\right]\right\}^{-1}. \tag{A. 38}$$

This alternative solution is not entirely tested in this work and is suggested for future studies since previous models failed. A discussion on this alternative method is discussed in appendix F.

Since $\Delta V_{th}=V\gamma_b\Delta T$ and if $\frac{\rho_b}{\rho_f}\rightarrow 1$, then equation (A.38) can also be rewritten as

$$V=\frac{\Delta V_{inj}}{\Delta P_c}\left\{\beta-\frac{1}{\Delta P_c}\left[\frac{\Delta V_{mc}}{V}-\frac{\Delta V_{ch}}{V}\left(1+\frac{\rho_s}{\rho_b}\right)+\frac{\gamma_b\Delta T}{1+\gamma_b\Delta T}\right]\right\}^{-1}. \tag{A. 39}$$

Appendix B – Model equations

In this section solutions in both spherical and cylindrical form are presented.

To transform the equation from rectangular (x, y, z) to spherical coordinates (r, ϕ, θ) the transformation applied:

$$\begin{cases} x = r\cos\phi\sin\theta \\ y = r\sin\phi\sin\theta \\ z = \cos\theta \end{cases}.$$

In cylindrical coordinates following transformation is applied:

$$\begin{cases} x = r\cos\phi \\ y = r\sin\phi \\ z = z \end{cases}.$$

A summary of the obtained solutions, in this section, is presented in Table 1Table 2. As shown in appendix A the pressure build-up in the cavity is not only related to the cavern volume and cavern compressibility but also to other phenomena. Table 2 summarizes the set of equations for the volume added by each phenomenon (thermal, hydraulic, mechanical and chemical).

Table 2 Summary of solutions used in the proposed model as obtained in appendix B.

	Sphere	**Cylinder**
Thermal	$\frac{\Delta V_{th}}{\mathrm{V}} = \gamma_b \frac{3\chi}{\pi}\left[T_\infty - T_b^o\left(1 - \frac{\gamma_b}{\rho_b C_b}\Delta P_c\right)\right]\left[\frac{t}{t_c^{th}} + 2\sqrt{\frac{t}{t_c^{th}}}\right]$	$\frac{\Delta V_{th}}{\mathrm{V}} = \gamma_b \frac{2\chi}{\pi}\left[T_\infty - T_b^o\left(1 - \frac{\gamma_b}{\rho_b C_b}\Delta P_c\right)\right]\left[\frac{t}{2t_c^{th}} + 2\sqrt{\frac{t}{t_c^{th}}}\right]$
Hydraulic	$\frac{\Delta V_{hy}}{V} = t(P_c - P_o)\left(\frac{3}{R^3}\frac{K}{\eta_b}\left(\frac{Rr_\infty}{r_\infty - R}\right) + \psi^o\right)$ $\frac{\Delta V_{hy}}{V}(r_\infty \gg R_c) = t(P_c - P_o)\left(\frac{3}{R^2}\frac{K}{\eta_b} + \psi^o\right)$	$\frac{\Delta V_{hy}}{\mathrm{V}} = t(P_c - P_o)\left(\frac{2}{R^2}\frac{K}{\eta_b}\left(\ln\frac{r_\infty}{R}\right)^{-1} + \psi^o\right)$
Mechanic	$\frac{\Delta V_{mc}}{V} = t\frac{3}{2}A^*\left[\frac{3}{2n}(P_\infty - P_C)\right]^n$	$\frac{\Delta V_{mc}}{V} = t\sqrt{3}A^*\left[\frac{\sqrt{3}}{n}(P_\infty - P_c)\right]^n$
Chemical	$\frac{\Delta V_{ch}}{\mathrm{V}} = \frac{3}{R}\frac{k(c_{sat} - c_0)}{\rho_s}t$	$\frac{\Delta V_{ch}}{\mathrm{V}} = \frac{2}{R}\left(1 + \frac{R}{H}\right)\frac{k(c_{sat} - c_0)}{\rho_s}t$

The thermal states that the relative volume change due to temperature effects as function of time is dependent of several parameters such as brine and rock properties (brine volumetric expansion coefficient γ_b, density ρ_i, and heat capacity C_i). It also includes the characteristic time t_c^{th}, which is dependent on thermal diffusivity of salt and cavern radius.

The hydraulic influence as function of time is dependent of the leak constant rate ψ^o, pressure gradient and hydraulic diffusivity $\frac{K}{\eta_b}$ of the brine lost by permeation.

The mechanic states that deformation is obtained from steady-state creep using Norton-Hoff law.

On the chemical influences the function is dependent on time, salt concentration c_0, convective mass transfer coefficient k, cavern radius and salt density.

Each of the solutions is obtained and explained in detail in this section for both spherical and cylindrical case. However, only spherical solutions are applied to the field data.

The solution for pressure build-up during a compressibility test can then be presented as function of the knowns contributing volumes in equation (A.18).

For the case of a spherical cavern the solution is;

$$\frac{\Delta V_{inj}}{\Delta P_c} = V^o\left[\beta\left(1+\frac{3}{R}\frac{k(c_{sat}-c_0)}{\rho_s}\;t\;-t\frac{3}{2}A^*\left[\frac{3}{2n}(P_\infty-P_C)\right]^n\right)-\frac{1}{\Delta P_c}\left(\gamma_b\frac{3\chi}{\pi}\left[T_\infty-T_b^o\left(1-\frac{\gamma_b}{\rho_b C_b}\Delta P_c\right)\right]\left[\frac{t}{t_c^{th}}+2\sqrt{\frac{t}{t_c^{th}}}\right]-t(P_c-P_o)\left(\frac{3}{R^3}\frac{K}{\eta_b}\left(\frac{Rr_\infty}{r_\infty-R}\right)+\psi^o\right)\right)\right]. \tag{B. 1}$$

In a cylindrical cavern the equation is written as

$$\frac{\Delta V_{inj}}{\Delta P_c} = V^o\left[\beta\left(1+\frac{2}{R}\left(1+\frac{R}{H}\right)\frac{k(c_{sat}-c_0)}{\rho_s}\;t-t\sqrt{3}A^*\left[\frac{\sqrt{3}}{n}(P_\infty-P_c)\right]^n\right)-\frac{1}{\Delta P_c}\left(\gamma_b\frac{2\chi}{\pi}\left[T_\infty-T_b^o\left(1-\frac{\gamma_b}{\rho_b C_b}\Delta P_c\right)\right]\left[\frac{t}{2t_c^{th}}+2\sqrt{\frac{t}{t_c^{th}}}\right]-t(P_c-P_o)\left(\frac{2}{R^2}\frac{K}{\eta_b}\left(\ln\frac{r_\infty}{R}\right)^{-1}+\psi^o\right)\right)\right]. \tag{B. 2}$$

B.1. Thermal

B.1.1. Governing Equations

For the thermal problem the heat equation is solved, which is presented in cartesian coordinates.

$$\rho_s C_s\frac{\partial T}{\partial t}-\nabla.(k_s\nabla \mathrm{T})+\dot{s}=0 \tag{B. 3}$$

$$\rho_s C_s\frac{\partial T}{\partial t}-\left[\frac{\partial}{\partial x}\left(k_s\frac{\partial T}{\partial x}\right)+\frac{\partial}{\partial y}\left(k_s\frac{\partial T}{\partial y}\right)+\frac{\partial}{\partial z}\left(k_s\frac{\partial T}{\partial z}\right)\right]+\dot{s}=0 \tag{B. 4}$$

Where, $\dot{s}$ is energy source or sink.

a) Sphere

By replacing in the transient heat equation, the spherical differential equation is obtained.

$$\rho_s C_s\frac{\partial T}{\partial t}-\left[\frac{1}{r^2}\frac{\partial}{\partial r}\left(k_s r^2\frac{\partial T}{\partial r}\right)+\frac{1}{r^2\sin^2\theta}\frac{\partial}{\partial\phi}\left(k_s\frac{\partial T}{\partial\phi}\right)+\frac{1}{r^2\,\mathrm{si}}\frac{\partial}{\partial\theta}\left(k_s\sin\theta\,\frac{\partial T}{\partial\theta}\right)\right]+\dot{s}=0 \tag{B. 5}$$

Rock salt is homogenous and isotropic, hence presenting uniform properties. Also, heat transfer is predominant in one direction, in this case radially from the far way boundaries of the sphere to the cavern cavity wall. The equation can then be re-written in its one-dimensional form to describe the heat flux from the rock to the brine inside the cavity.

$$\rho_s C_s\frac{\partial T}{\partial t}-k_s\frac{1}{r^2}\frac{\partial}{\partial r}\left(r^2\frac{\partial T}{\partial r}\right)+\dot{s}=0 \tag{B. 6}$$

b) Cylinder

Analogous to previous solution, considering the material isotropic and predominance of radial heat transfer then the equation can be reduced from its extended form (B.6) to reduced form (B.7).

$$\rho_s C_s\frac{\partial T}{\partial t}-\left[\frac{1}{r}\frac{\partial}{\partial r}\left(k_s\,r\frac{\partial T}{\partial r}\right)+\frac{1}{r^2}\frac{\partial}{\partial\phi}\left(k_s\,r\frac{\partial T}{\partial\phi}\right)+\frac{\partial}{\partial z}\left(k_s\frac{\partial T}{\partial z}\right)\right]+\dot{s}=0 \tag{B. 7}$$

$$\rho_s C_s\frac{\partial T}{\partial t}-k_s\frac{1}{r}\frac{\partial}{\partial r}\left(r\frac{\partial T}{\partial r}\right)+\dot{s}=0 \tag{B. 8}$$

B.1.2. Analytical solution

Carslaw & Jaeger, [29] present the solution for a solid at initial temperature ($\theta_i(0) = \theta_o$) and bounded by constant surface temperature (θ_R^∞). The solution is given by Van Sambeek et al. [6] and Beréast et al [30], by applying the conditions,

$$\begin{cases} \frac{\partial \theta_R}{\partial t} = k_s^{th} \Delta \theta_R \\ \iint_{S_\Omega} K_s^{th} \frac{\partial \theta_R}{\partial n} dS_\Omega = \rho_b C_b V \dot{\theta}_\imath \\ \theta_R(wall, t) = \theta_i(t) \\ \theta_R(rock\ mass, 0) = \theta_R^\infty \end{cases} , \tag{B. 9}$$

where all heat supplied by the rock is used in the brine warming process, and $\dot{s}$ is zero since no geothermal heat flux is considered.

a) Sphere

In the case of cavity with spherical shape, the brine temperature solution is given as below, [30].

$$\theta(r,t) = \theta_o + T_o \frac{a}{r} \operatorname{erf} \frac{r-a}{\sqrt{4kt}} \tag{B. 10}$$

Or in the case that $a = a(t)$ we obtain

$$\theta(r,t) = \theta_o + \int_0^t \frac{\partial \theta}{\partial t} [a(\tau), \tau] \frac{a(\tau)}{r} \operatorname{erf} \frac{r-a(t)}{\sqrt{4kt}} d\tau\ . \tag{B. 11}$$

The solution is presented in a simplified form as derived by Van Sambeek, [6], which include the thermal capacity ratio χ that is obtained by applying the boundary conditions in (B.9) where $k_s^{th} = \frac{K_s^{th}}{\rho_S C_S}$.

$$\Delta \theta = \frac{3\chi}{\pi} [\theta_R^\infty - \theta_i(0)] \left[\frac{t}{t_c^{th}} + 2\sqrt{\frac{t}{t_c^{th}}} \right] \tag{B. 12.a}$$

$$\chi = \frac{\rho_S C_S}{\rho_b C_b} \tag{B. 12.b}$$

$$t_c^{th} = \frac{R^2}{\pi\, k_s^{th}} \tag{B. 12.c}$$

The term $[\theta_R^\infty - \theta_i(0)]$ in equation (B.12.a) is the temperature difference between rock and brine, which can be re-written as $[T_\infty - T_b^o]$.

Another approach and solution are presented by VanSant, [31], for the case of a spherical object with infinity conductivity in an infinite medium. The assumption of infinity conductivity implies that there is no temperature gradient inside the brine.

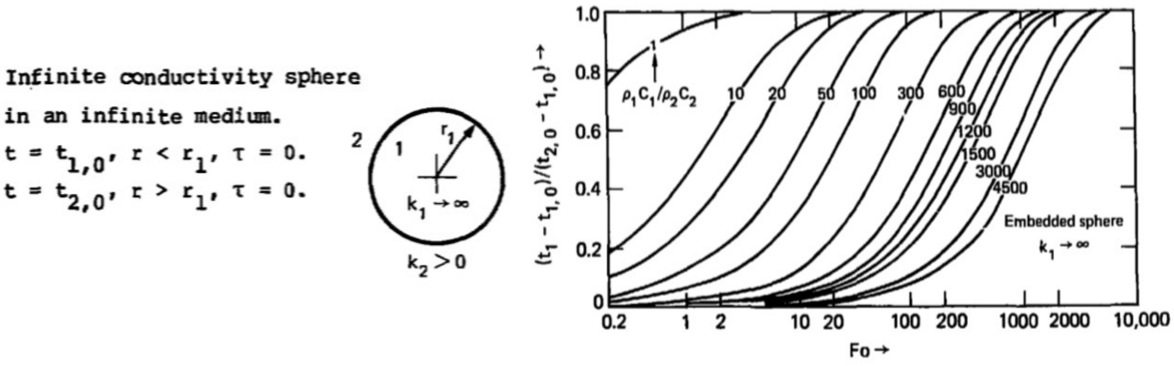

Figure 14 On the left the problem is illustrated by a solid sphere with infinity conductivity with initial temperature, embedded by an infinite solid with known initial temperature. On the right a plot of the problem solution as function of Fourier number ($Fo = \frac{\alpha t}{L_c^2}$) and system thermal capacity ratio ($\chi = \frac{\rho_s c_s}{\rho_b c_b}$) .

The solution for brine temperature can be found graphically in Figure 14, where

$$\frac{T_b(t)-T_{b,0}}{T_\infty-T_{b,0}} = f\left(Fo,\frac{1}{\chi}\right), \qquad \text{(B. 13)}$$

and

$$Fo = \frac{\alpha t}{L_c^2}. \qquad \text{(B. 14)}$$

If work performed during fluid pressurization is considered, from Van Sambeek [6], the impact in temperature can be written as:

$$\Delta\vartheta = \frac{3\chi}{\pi}\left[\frac{\gamma_b}{\rho_b c_b} T_b^o \Delta P_c\right]\left[\frac{t}{t_c^{th}} + 2\sqrt{\frac{t}{t_c^{th}}}\right] \qquad \text{(B. 15)}$$

Where, $\Delta\vartheta$ is the temperature increase due to pressure change only. During a compressibility test this impact is very small, unless significant pressure increase is inferred to the cavern.

By using Van Sambeek solution, the final increase in temperature due to warming and pressure is written as:

$$\Delta T = \frac{3\chi}{\pi}\left[T_\infty - T_b^o\left(1-\frac{\gamma_b}{\rho_b c_b}\Delta P_c\right)\right]\left[\frac{t}{t_c^{th}} + 2\sqrt{\frac{t}{t_c^{th}}}\right] \qquad \text{(B. 16)}$$

b) Cylinder

Bérest and Van Sambeek also present a solution for a cylindrical shape (eq. B.17 and B.18) and its simplified form (eq. B.19).

$$\theta(r,t) = \theta_o + T_o \Upsilon\left(\frac{r}{R},t\right) \qquad \text{(B. 17)}$$

$$\theta(r,t) = \theta_o + \int_0^t \frac{\partial\theta}{\partial t}[a(\tau),\tau]\Upsilon\left(\frac{r}{R(t-\tau)},t-\tau\right)d\tau \qquad \text{(B. 18.a)}$$

$$\Upsilon\left(\frac{r}{R},t\right) = 1 + \frac{2}{\pi}\int_0^\infty e^{ku^2 t}\,\frac{J_o(ur)Y_o(uR)-Y_o(ur)J_o(uR)}{J_o^2(uR)+Y_o^2(uR)}\frac{du}{u} \qquad \text{(B. 18.b)}$$

$$\Delta\theta = \frac{2\chi}{\pi}[\theta_R^\infty - \theta_i(0)]\left[\frac{t}{2t_c^{th}} + 2\sqrt{\frac{t}{t_c^{th}}}\right] \tag{B. 19}$$

As derived by Karimi-Jafari [17], the characteristic time for a cylindrical shape is:

$$t_c^{th} = a\exp\left[-\frac{1}{2}\left(\frac{\ln\frac{H/D}{A_0}}{b}\right)^2\right]. \tag{B. 20}$$

Where; a, b, A_0 are empirical constants, and H/D the cylinder height and diameter ratio.

An alternative solution is presented by VanSant, [31], for the case of an infinite cylinder with infinity conductivity in an infinite medium. The brine temperature evolution in time is given below.

$$\frac{T_b - T_\infty}{T_{b,0} - T_\infty} = \frac{4(2\chi)}{\pi^2}\int_0^\infty \exp(-\lambda^2 Fo)\frac{d\lambda}{\lambda\Lambda} \tag{B. 21}$$

$$\Lambda = [\lambda J_o(\lambda) - 2\chi J_1(\lambda)]^2 + [\lambda Y_o(\lambda) - 2\chi Y_1(\lambda)]^2 \tag{B. 22}$$

Analogous to the spherical case, incorporating brine temperature increase due to pressure as derived by Van Sambeek, the solution can be written as:

$$\Delta T = \frac{2\chi}{\pi}\left[T_\infty - T_b^o\left(1 - \frac{\gamma_b}{\rho_b C_b}\Delta P_c\right)\right]\left[\frac{t}{2t_c^{th}} + 2\sqrt{\frac{t}{t_c^{th}}}\right]. \tag{B. 23}$$

B.2. Hydraulic

There are two forms for fluid loss in the system; one is by permeation and the other by leaks within the system. Such leaks may occur by loss of fluid to well completions, topsides, or within the cavern sump. According to Bérest [1], the leak is linked to the difference between cavern and pore pressure.

$$\Delta V_{leak} = t\psi(P_c - P_o) = t\psi^o V(P_c - P_o) \ , \tag{B. 24}$$

where; ψ is a leaking constant. The total hydraulic volume change ΔV_{hy} is then obtained by summing leak and permeation losses, i.e.

$$\Delta V_{hy} = \ \Delta V_p + \Delta V_{leak} \ . \tag{B. 25}$$

B.2.1. Governing equations

From mass conservation and total compressibility ($c_t = c_{fluid} + c_{formation}$), we obtain

$$\frac{\varphi\eta_b c_t}{K_s}\frac{\partial P}{\partial t} - \nabla^2 P = 0 \ . \tag{B. 26}$$

a) Sphere

For spherical coordinates the equation can be written as below i.e.,

$$\frac{1}{r^2}\frac{\partial}{\partial r}\left(r^2\frac{\partial P}{\partial r}\right) + \frac{1}{r^2\sin^2\theta}\frac{\partial}{\partial\phi}\left(\frac{\partial P}{\partial\phi}\right) + \frac{1}{r^2\sin\theta}\frac{\partial}{\partial\theta}\left(\sin\theta\,\frac{\partial P}{\partial\theta}\right) = \frac{\varphi\eta_b c_t}{K_s}\frac{\partial P}{\partial t} \ . \tag{B. 27}$$

For the case of predominantly flow in radial direction, the spherical form can be simplified i.e.,

$$\frac{1}{r^2}\frac{\partial}{\partial r}\left(r^2\frac{\partial P}{\partial r}\right) = \frac{\varphi\eta_b c_t}{K_s}\frac{\partial P}{\partial t} \ . \tag{B. 28}$$

b) Cylinder

In cylindrical coordinates the equation can be written as below.

$$\frac{1}{r}\frac{\partial}{\partial r}\left(r\frac{\partial P}{\partial r}\right) + \frac{1}{r^2}\frac{\partial}{\partial\phi}\left(r\frac{\partial P}{\partial\phi}\right) + \frac{1}{z}\frac{\partial}{\partial z}\left(\frac{\partial P}{\partial z}\right) = \frac{\varphi\eta_b c_t}{K_s}\frac{\partial P}{\partial t} \tag{B. 29}$$

For a predominant linear flow in radial direction, the equation can be simplified as

$$\frac{1}{r}\frac{\partial}{\partial r}\left(r\frac{\partial P}{\partial r}\right) = \frac{\varphi\eta_b c_t}{K_s}\frac{\partial P}{\partial t} \ . \tag{B. 30}$$

B.2.2. Analytical solution

By applying boundary conditions, the solutions for spherical and cylindrical caverns are obtained.

a) Sphere

Since the brine is permeating to the formation for a long time with cavern pressure above halmostatic, it is plausible to assume that steady-state flow is stablished.

$$\frac{1}{r^2}\frac{\partial}{\partial r}\left(r^2\frac{\partial P}{\partial r}\right) = 0 \ \rightarrow \ \left(r^2\frac{\partial P}{\partial r}\right) = C_1 \ , \tag{B. 31}$$

$$\frac{\partial P}{\partial r} = \frac{C_1}{r^2} \rightarrow \ \int dP = \int\frac{C_1}{r^2}dr \qquad , \tag{B. 32}$$

$$P(r) = C_1\left(-\frac{1}{r}\right) + C_2 \qquad . \tag{B. 33}$$

The Dirichlet boundary conditions are then applied to obtain constants for equation (B.33), i.e.,

$$\begin{cases} P_c = C_1\left(-\frac{1}{R_c}\right) + C_2 \\ P(r_\infty) = C_1\left(-\frac{1}{r_\infty}\right) + C_2 \end{cases} \rightarrow \; C_1 = \frac{P_o - P_c}{\left(\frac{1}{R_c} - \frac{1}{r_\infty}\right)} \; . \tag{B. 34}$$

Applying Neumann boundary conditions from Darcy's law $q = -\frac{K_s A_c}{\eta_b}\frac{\partial P}{\partial r}$ we obtain

$$\frac{\partial P}{\partial r} = -\frac{q\eta_b}{4\pi r^2 K_s} = \frac{C_1}{r^2} \rightarrow C_1 = -\frac{q\eta_b}{4\pi K_s} \; . \tag{B. 35}$$

By substituting (B.34) and (B.35) in equation (B.33 we obtain

$$P(r) - P_c = \frac{q\eta_b}{4\pi K_s}\left(\frac{1}{R_c} - \frac{1}{r}\right) . \tag{B. 36}$$

At the cavern wall then the volumetric flow rate will be

$$q = \frac{4\pi K_s}{\eta_b}\left(\frac{R_c r_\infty}{r_\infty - R_c}\right)(P_c - P_o) \; . \tag{B. 37}$$

Therefore, the total volume loss by permeation ΔV_p for steady-state condition during the test is;

$$\Delta V_p = t\,\frac{4\pi K_s}{\eta_b}\left(\frac{R_c r_\infty}{r_\infty - R_c}\right)(P_c - P_o) \; . \tag{B. 38}$$

The dependency on the boundary radius, distance to aquifer, is eliminated if $(r = r_\infty) \gg R_c$ at equation (B.36), where $P(r = r_\infty) = P_0$. This results ins $\frac{1}{R_c} \gg \frac{1}{r_\infty}$, and q reduces to $q = \frac{4\pi K_s R_c}{\eta_b}(P_c - P_o)$. Equation (B.38) than can be written as

$$\Delta V_p(\mathrm{r}_\infty \gg \mathrm{R_C}) = t\,\frac{4\pi K R_c}{\eta_b}(P_c - P_o) \; . \tag{B. 39}$$

This is a useful relation for the cases where $r_\infty \gg R_c$, and unknown.

b) Cylinder

Assuming steady-state we obtain Darcy flow and

$$\frac{1}{r}\frac{\partial}{\partial r}\left(r\frac{\partial P}{\partial r}\right) = 0 \;\rightarrow\; \left(r\frac{\partial P}{\partial r}\right) = C_1 \; , \tag{B. 40}$$

$$\frac{\partial P}{\partial r} = \frac{C_1}{r} \rightarrow \; \int dP = \int \frac{C_1}{r} dr \; , \tag{B. 41}$$

$$P(r) = C_1 \ln r + C_2 \qquad . \tag{B. 42}$$

Applying Dirichlet boundary conditions to equation (B.42) the first constant is obtained, i.e.

$$\begin{cases} P_c = C_1 \ln r_c + C_2 \\ P(r_\infty) = C_1 \ln r_\infty + C_2 \end{cases} \;\rightarrow\; C_1 = \frac{P_o - P_c}{\ln\frac{r_\infty}{R_c}} \; . \tag{B. 43}$$

Applying Neumann boundary conditions, and using Darcy's law $q = -\frac{K_s A_c}{\eta_b}\frac{\partial P}{\partial r}$ we obtain

$$\frac{\partial P}{\partial r} = -\frac{q\eta_b}{2\pi r H K_s} = \frac{C_1}{r} \rightarrow C_1 = -\frac{q\eta_b}{2\pi H K_s} \; . \tag{B. 44}$$

Therefore, by substituting in equation (B.42) and subtracting it from (B.43) we obtain

$$P(r) - P_c = -\frac{q\eta_b}{2\pi HK}\ln\frac{r}{R_c} \quad . \tag{B. 45}$$

The volumetric flow rate q is then given by

$$q = \frac{2\pi HK_s}{\eta_b}\left(\frac{1}{\ln\frac{r_\infty}{R_c}}\right)(P_c - P_o) \ . \tag{B. 46}$$

Therefore, the total volume loss by permeation is;

$$\Delta V_p = t\,\frac{2\pi HK_s}{\eta_b}\left(\frac{1}{\ln\frac{r_\infty}{R_c}}\right)(P_c - P_o) \ . \tag{B. 47}$$

The dependency on the boundary radius, i.e. distance to aquifer, cannot be eliminated in this case. This is for $(r = r_\infty) \gg R_c$ at equation (B.45), then $(P(r = r_\infty) - P_\text{o}) \rightarrow \infty$, what is unphysical result. This is caused by the logarithmic singularity. The physical meaning is that either a transient solution should be used, or a representative radius should be defined.

B.3. Mechanical

B.3.1. Governing equations

The mechanical behaviour is obtained by applying Cauchy's Equation of motion (eq. B.48) or the equilibrium equation for the case of static equilibrium (eq. B.49), [11].

$$\rho \boldsymbol{f} + div\, \boldsymbol{\sigma} = \rho \frac{\partial^2 u}{\partial t^2}\,, \tag{B. 48}$$

which reduces for stationary conditions to

$$\rho \boldsymbol{f} + div\, \boldsymbol{\sigma} = 0\ . \tag{B. 49}$$

The constitutive relationship between strain and stress from Hooke's law gives, [32],

$$\boldsymbol{\sigma} = 2\mu \boldsymbol{\varepsilon} + \lambda \boldsymbol{\delta} \textstyle\sum_k \varepsilon_{kk}\ , \tag{B. 50}$$

where μ and λ are Lamé's elastic constants, and $\boldsymbol{\delta}$ is the Kronecker delta ($\delta_{ij} = 1$ if $i = j$ and $\delta_{ij} = 0$ if $i \neq j$).

$$\mu = G = \frac{E}{2(1+\vartheta)} \quad \text{and} \quad \lambda = \frac{\vartheta E}{(1+\vartheta)(1-2\vartheta)}\quad . \tag{B. 51}$$

For isotropic materials equation (B. 50) can be also expressed as;

$$\boldsymbol{\varepsilon} = \frac{1+\vartheta}{2} \boldsymbol{\sigma} - \frac{\vartheta}{E} tr(\boldsymbol{\sigma}) \mathbf{I}\ . \tag{B. 52}$$

Here, the deformation is denotated as the Cauchy's strain tensor,

$$\boldsymbol{\varepsilon} = \frac{1}{2}(\nabla \boldsymbol{u} + (\nabla \boldsymbol{u})^T)\ . \tag{B. 53}$$

But if $\nabla \boldsymbol{u}$ is symmetric $\nabla \boldsymbol{u} = (\nabla \boldsymbol{u})^T$, and therefore

$$\boldsymbol{\varepsilon} = \nabla \boldsymbol{u}\ \ . \tag{B. 54}$$

Navier-Cauchy equilibrium equation is then obtained by substituting Cauchy's strain tensor (B.53) into Hooke's law (B.50), and then into the equilibrium equation (B.49), [11], i.e.

$$(\lambda + G)\nabla(\nabla . \boldsymbol{u}) + \boldsymbol{G}\nabla^2 \boldsymbol{u} + \rho \boldsymbol{f} = 0\ \ . \tag{B. 55}$$

a) Sphere

For spherical coordinates the problem is illustrated as in Figure 15.

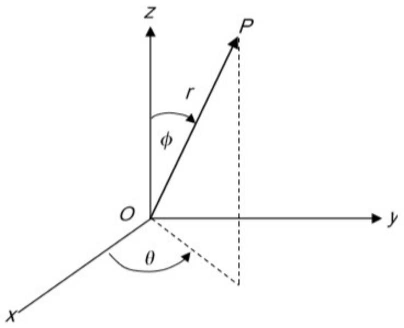

Figure 15 Spherical coordinates system, [11]

Adopting (u, v, w) as the displacement in (r, θ, ϕ) directions. The equilibrium equation, (B.49), in spherical coordinates in isotropic and impermeable solid than becomes, [11] [23]:

$$\rho f_r + \frac{\partial \sigma_{rr}}{\partial r} + \frac{2}{r}(\sigma_{rr} - \sigma_{\theta\theta}) = 0 \tag{B. 56.a}$$

$$\rho f_\theta + \frac{1}{r}\frac{\partial \sigma_{\theta\theta}}{\partial \theta} = 0 \tag{B. 56.b}$$

b) Cylinder

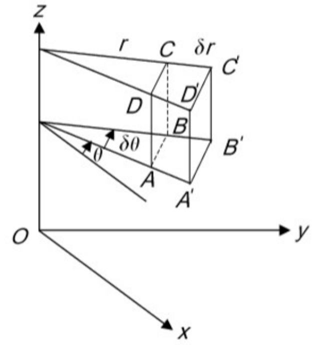

Figure 16 Cylindrical coordinates system, [11]

Adopting (u, v) as the displacement in (r, θ) directions, and no displacement in z. The equilibrium equation (B.49) for an infinite cylinder than becomes, [11], [32]:

$$\rho f_r + \frac{\partial \sigma_{rr}}{\partial r} + \frac{1}{r}\frac{\partial \tau_{\theta r}}{\partial \theta} + \frac{\sigma_{rr} - \sigma_{\theta\theta}}{r} = 0 \quad , \tag{B. 57.a}$$

$$\rho f_\theta + \frac{\partial \tau_{r\theta}}{\partial r} + \frac{1}{r}\frac{\partial \sigma_{\theta\theta}}{\partial \theta} + \frac{2\tau_{r\theta}}{r} = 0 \ . \tag{B. 57.b}$$

B.3.2. Analytical solution

By applying boundary conditions, the solutions for spherical and cylindrical caverns are obtained.

a) Sphere

Elastic and plastic deformations are obtained by applying governing equations of motion and Hooke's relationships.

ELASTIC SCENARIO

For Hooke's law (B.52) in spherical coordinates, [11];

$$\begin{bmatrix} \varepsilon_{rr} \\ \varepsilon_{\theta\theta} \\ \varepsilon_{\phi\phi} \end{bmatrix} = \frac{1}{E}\begin{bmatrix} 1 & -\vartheta & -\vartheta \\ -\vartheta & 1 & -\vartheta \\ -\vartheta & -\vartheta & 1 \end{bmatrix}\begin{bmatrix} \sigma_{rr} \\ \sigma_{\theta\theta} \\ \sigma_{\phi\phi} \end{bmatrix} . \tag{B. 58}$$

The stress-strain relationship can be written as:

$$\varepsilon_{rr} = \frac{1}{E}(\sigma_{rr} - 2\vartheta\sigma_{\theta\theta}) \quad , \tag{B. 59}$$

$$\varepsilon_{\theta\theta} = \varepsilon_{\phi\phi} = \frac{1}{E}[(1-\vartheta)\sigma_{\theta\theta} - \vartheta\sigma_{rr}] \ . \tag{B. 60}$$

Due to symmetry, only the radial displacement and normal strains are nonzero, [17], i.e.

$$\varepsilon_{rr} = \frac{\partial u}{\partial r} \quad , \tag{B. 61}$$

$$\varepsilon_{\theta\theta} = \varepsilon_{\phi\phi} = \frac{u}{r} \quad . \tag{B. 62}$$

Reciprocal to Hooke's law (read e.g. Jaeger et al.) [11] reads

$$\sigma_{rr} = (2\mu + \lambda)\varepsilon_{rr} + \lambda(\varepsilon_{\theta\theta} + \varepsilon_{\phi\phi}) \, , \tag{B. 63}$$

$$\sigma_{\theta\theta} = \sigma_{\phi\phi} = (2\mu + \lambda)\varepsilon_{\theta\theta} + \lambda(\varepsilon_{rr} + \varepsilon_{\phi\phi}). \tag{B. 64}$$

which can also be re-written as equations (B.65) and (B.66);

$$\sigma_{rr} = (2\mu + \lambda)\frac{\partial u}{\partial r} + 2\lambda\frac{u}{r} \; , \tag{B. 65}$$

$$\sigma_{\theta\theta} = \sigma_{\phi\phi} = 2(\mu + \lambda)\frac{u}{r} + \lambda\frac{\partial u}{\partial r} \, . \tag{B. 66}$$

Substituting in the equilibrium equation, (B.57) we obtain

$$\rho f_r + \frac{\partial^2 u}{\partial r^2} + \frac{2}{r}\frac{\partial u}{\partial r} - 2\frac{u}{r^2} = 0 \; . \tag{B. 67}$$

For negligible body forces, (B.67) can also be written as

$$\frac{\partial}{\partial r}\left[\frac{1}{r^2}\frac{\partial}{\partial r}(r^2 u)\right] = 0 \; . \tag{B. 68}$$

Integrating equation (B.68) shows that u must be of the form

$$u(r) = C_1 r + \frac{C_2}{r^2} \; . \tag{B. 69}$$

The relevant stress components take the form

$$\sigma_{rr}(r) = (2\mu + \lambda)\left(C_1 - \frac{2C_2}{r^3}\right) + 2\lambda\left(C_1 + \frac{C_2}{r^3}\right) = C_1^* + \frac{C_2^*}{r^3} \quad , \tag{B. 70}$$

$$\sigma_{\theta\theta} = \sigma_{\phi\phi} = 2(\mu + \lambda)\left(C_1 + \frac{C_2}{r^3}\right) + \lambda\left(C_1 - \frac{2C_2}{r^3}\right) = C_1^* - \frac{1}{2}\frac{C_2^*}{r^3} \; . \tag{B. 71}$$

Boundary conditions at the wall and far from the spherical cavity are applied to obtain the constants above, i.e.

$$\sigma_{rr}(\infty) = 0 \rightarrow C_1^* = 0 \quad , \tag{B. 72}$$

$$\sigma_{rr}(R) = (P_\infty - P_c) \rightarrow C_2^* = (P_\infty - P_c)R^3 \; . \tag{B. 73}$$

Therefore, the stress components as a function of radial distance to the cavity are given by

$$\sigma_{rr} = (P_\infty - P_c)\frac{R^3}{r^3} \quad , \tag{B. 74}$$

$$\sigma_{\theta\theta} = -\frac{1}{2}(P_\infty - P_c)\frac{R^3}{r^3} \quad . \tag{B. 75}$$

upon replacing it in: $\frac{u}{r} = \frac{1}{E}[(1-\vartheta)\sigma_{\theta\theta} - \vartheta\sigma_{rr}]$, (B.60) we obtain

$$\frac{u}{r} = -\frac{(1+\vartheta)}{2E}\frac{R^3}{r^3}(P_\infty - P_c) \quad . \tag{B. 76}$$

The total radial displacement at the wall of the spherical cavity is given by, $u(R)$, hence;

$$\frac{\delta V}{V} = \frac{A_C u(R)}{V} = \frac{4\pi R^2 u(R)}{\frac{4}{3}\pi R^3} = 3\,\frac{u(R)}{R} \,. \tag{B. 77}$$

Therefore, from eq. (B.76) the volume deformation as function of pressure is,

$$\frac{\delta V}{V} = -\frac{3}{2}\frac{(1+\vartheta)}{E}\,(P_\infty - P_c) \quad . \tag{B. 78}$$

This also leads to cavity compressibility for a spherical shape, i.e.,

$$\beta = -\frac{1}{V}\frac{\partial V}{\partial P} \rightarrow \beta_c = \frac{3}{2}\frac{(1+\vartheta)}{E} \quad . \tag{B. 79}$$

PLASTIC SCENARIO

From Karimi-Jafari the solution for the plastic deformation is presents, [17]. It is established that on the plastic zone the deformation rate will be a combination of elastic and plastic behavior, i.e.,

$$\dot{\varepsilon} = \dot{\varepsilon}^e + \dot{\varepsilon}^{vp} \quad . \tag{B. 80}$$

The rate of deformation components can be written as

$$\dot{\varepsilon}_{rr} = \frac{\partial v}{\partial r} = \frac{1}{E}(\dot{\sigma}_{rr} - 2\vartheta\dot{\sigma}_{\theta\theta}) + \dot{\mu} + \dot{\lambda} \,, \tag{B. 81}$$

$$\dot{\varepsilon}_{\theta\theta} = \frac{v}{r} = \frac{1}{E}[(1-\vartheta)\dot{\sigma}_{\theta\theta} - \vartheta\dot{\sigma}_{rr}] - \dot{\lambda} \,, \tag{B. 82}$$

$$\dot{\varepsilon}_{\phi\phi} = \frac{v}{r} = \frac{1}{E}[(1-\vartheta)\dot{\sigma}_{\theta\theta} - \vartheta\dot{\sigma}_{rr}] - \dot{\mu} \,. \tag{B. 83}$$

From the relationship it is possible to conclude that $\dot{\mu} = \dot{\lambda}$. Integrating both equations we obtain

$$\varepsilon_{rr} = \frac{\partial u}{\partial r} = \frac{1}{E}(\sigma_{rr} - 2\vartheta\sigma_{\theta\theta}) + 2\lambda \quad , \tag{B. 84}$$

$$\varepsilon_{\theta\theta} = \frac{u}{r} = \frac{1}{E}[(1-\vartheta)\sigma_{\theta\theta} - \vartheta\sigma_{rr}] - \lambda \,. \tag{B. 85}$$

Applying Tresca's criterium for failure [17], $(\sigma_{rr} - \sigma_{\theta\theta} = 2c)$, in the equilibrium equation;

$$\frac{\partial\sigma_{rr}}{\partial r} + \frac{2}{r}(\sigma_{rr} - \sigma_{\theta\theta}) = 0 \tag{B. 86}$$

$$\frac{\partial\sigma_{rr}}{\partial r} + \frac{4c}{r} = 0 \tag{B. 87}$$

Tresca's criteria is chosen instead of Von Mises because at the grain level yielding occurs due to displacement on the slip plane. However, Von Mises criteria could be applied, but this solution is more complex and not presented here.

By integrating eq. (B.87) and subsequently (B.86) a solution for the equation is obtained, which reads

$$\sigma_{rr} = -4c\ln\frac{r}{R} + C_3 \quad , \tag{B. 88}$$

$$\sigma_{\theta\theta} = -4c\ln\frac{r}{R} + C_3 - 2c\ . \tag{B. 89}$$

The boundary condition is that at the wall of the spherical cavity $\sigma_{rr}(R) = (P_\infty - P_c)$, thus $\lambda = 0$ at the wall, [17]. Therefore, the total plastic radial displacement in the spherical cavity is:

$$\frac{\delta V}{V} = 3\frac{u(R)}{R} = -\frac{3}{E}\left[(1-2\vartheta)(P_\infty - P_c) - \frac{3}{2}(1-\vartheta)\exp\left[(P_\infty - P_c)\left(\frac{3}{4c}\right) - 1\right]\right] \tag{B. 90}$$

STEADY-STATE PLASTIC SCENARIO

For the case of a steady state creep the stress in the massive is at stationary state, thus stress rates are zero;

$$\dot{\sigma}_{rr} = \dot{\sigma}_{\theta\theta} = 0\ , \tag{B. 91}$$

or

$$\frac{\partial v}{\partial r} + \frac{2v}{r} = 0\ . \tag{B. 92}$$

Karimi-Jafari [17] and Van Sambeek [6] propose that the solution for geometric creep under Norton-Hoff model in permanent regime for sphere is

$$\frac{\delta V}{V} = 3\frac{u(R)}{R} = \frac{3}{2}A^*\left[\frac{3}{2n}(P_\infty - P_C)\right]^n\ . \tag{B. 93}$$

b) Cylinder

From the governing equations the solution for elastic and plastic deformation are obtained as below.

ELASTIC SCENARIO

For Hooke's law (B.52) in spherical coordinates, disregarding z which covers stability of cavity roof, [11]

$$\begin{bmatrix}\varepsilon_{rr}\\ \varepsilon_{\theta\theta}\\ \varepsilon_{r\theta}\end{bmatrix} = \frac{1}{E}\begin{bmatrix}1 & -\vartheta & 0\\ -\vartheta & 1 & 0\\ 0 & 0 & 1+\vartheta\end{bmatrix}\begin{bmatrix}\sigma_{rr}\\ \sigma_{\theta\theta}\\ \tau_{r\theta}\end{bmatrix}\ . \tag{B. 94}$$

The stress-strain relationship is written as

$$\varepsilon_{rr} = \frac{1}{E}(\sigma_{rr} - \vartheta\sigma_{\theta\theta})\ , \tag{B. 95}$$

$$\varepsilon_{\theta\theta} = \frac{1}{E}(\sigma_{\theta\theta} - \vartheta\sigma_{rr})\ , \tag{B. 96}$$

$$\varepsilon_{r\theta} = \frac{1+\vartheta}{E}\tau_{r\theta} = \frac{1}{2\mu}\tau_{r\theta}. \tag{B. 97}$$

The stress-strain relationship can also be written as in Malvern, [33]:

$$\varepsilon_{rr} = \frac{\partial u}{\partial r}\ , \tag{B. 98}$$

$$\varepsilon_{\theta\theta} = \frac{1}{r}\frac{\partial v}{\partial \theta} + \frac{u}{r}\ , \tag{B. 99}$$

$$\varepsilon_{r\theta} = \frac{1}{2}\left(\frac{1}{r}\frac{\partial u}{\partial \theta} + \frac{\partial v}{\partial r} - \frac{v}{r}\right)\ . \tag{B. 100}$$

Therefore, the volumetric strain is, [11],

$$\varepsilon_{\mathrm{V}} = \varepsilon_{rr} + \varepsilon_{\theta\theta} = \frac{\partial u}{\partial r} + \frac{u}{r} + \frac{1}{r}\frac{\partial v}{\partial \theta} \; . \tag{B. 101}$$

Reciprocal to Hooke's law, (B. 50) we obtain

$$\sigma_{rr} = (2\mu + \lambda)\varepsilon_{rr} + \lambda\varepsilon_{\theta\theta} \;\; , \tag{B. 102}$$

$$\sigma_{\theta\theta} = (2\mu + \lambda)\varepsilon_{\theta\theta} + \lambda\varepsilon_{rr} \; , \tag{B. 103}$$

$$\tau_{r\theta} = (2\mu)\varepsilon_{r\theta} \quad . \tag{B. 104}$$

which can be re-written, from (B.98), (B.99) and (B.100) as the equations below;

$$\sigma_{rr} = (2\mu + \lambda)\frac{\partial u}{\partial r} + \lambda\left(\frac{1}{r}\frac{\partial v}{\partial \theta} + \frac{u}{r}\right) \quad , \tag{B. 105}$$

$$\sigma_{\theta\theta} = (2\mu + \lambda)\left(\frac{1}{r}\frac{\partial v}{\partial \theta} + \frac{u}{r}\right) + \lambda\frac{\partial u}{\partial r} \quad , \tag{B. 106}$$

$$\tau_{r\theta} = \mu\left(\frac{1}{r}\frac{\partial u}{\partial \theta} + \frac{\partial v}{\partial r} - \frac{v}{r}\right) = 2\mu\varepsilon_{\mathrm{V}} \quad . \tag{B. 107}$$

Substituting in the equilibrium equation we obtain

$$\rho f_r + (\mu + \lambda)\frac{\partial \varepsilon_{\mathrm{V}}}{\partial r} + \mu\left(\frac{\partial^2 u}{\partial r^2} + \frac{1}{r}\frac{\partial u}{\partial r} - \frac{u}{r^2} + \frac{1}{r^2}\frac{\partial^2 u}{\partial \theta^2} - \frac{2}{r^2}\frac{\partial v}{\partial \theta}\right) = 0 \; , \tag{B. 108}$$

$$\rho f_\theta + (\mu + \lambda)\frac{\partial \varepsilon_{\mathrm{V}}}{\partial \theta} + \mu\left(\frac{\partial^2 v}{\partial r^2} + \frac{1}{r}\frac{\partial v}{\partial r} - \frac{v}{r^2} + \frac{1}{r^2}\frac{\partial^2 v}{\partial \theta^2} - \frac{2}{r^2}\frac{\partial v}{\partial \theta}\right) = 0 \; . \tag{B. 109}$$

From Kirsch (1898) [34], Malvern, [33], and Grandi et al [10] the radial stress, circumferential stress and tangential shear stress can be written as

$$\sigma_{rr} = \frac{1}{2}(SH^* + Sh^*)\left(1 - \frac{R^2}{r^2}\right) + \frac{1}{2}(SH^* - Sh^*)\left(1 - 4\frac{R^2}{r^2} + 3\frac{R^4}{r^4}\right)\cos 2\theta + (P_c - P_o)\frac{R^2}{r^2} \quad , \tag{B. 110}$$

$$\sigma_{\theta\theta} = \frac{1}{2}(SH^* + Sh^*)\left(+1 - \frac{R^2}{r^2}\right) - \frac{1}{2}(SH^* - Sh^*)\left(1 + 3\frac{R^4}{r^4}\right)\cos 2\theta - (P_c - P_o)\frac{R^2}{r^2} \quad , \tag{B. 111}$$

$$\tau_{r\theta} = -\frac{1}{2}(SH^* - Sh^*)\left(1 + 2\frac{R^2}{r^2} - 3\frac{R^4}{r^4}\right)\sin 2\theta \quad . \tag{B. 112}$$

where $SH^* = SH - P_o$, also in the case of rock salt $SH = P_\infty$. For an infinite cylinder, in isotropic medium, assuming an impermeable wall, referred to as Lamé's solution is;

$$\sigma_{rr} = P_\infty\left(1 - \frac{R^2}{r^2}\right) + P_c\frac{R^2}{r^2} = -(P_\infty - Pc\,)\frac{R^2}{r^2} + P_\infty \; , \tag{B. 113}$$

$$\sigma_{\theta\theta} = P_\infty\left(1 + \frac{R^2}{r^2}\right) - P_c\frac{R^2}{r^2} = (P_\infty - Pc\,)\frac{R^2}{r^2} + P_\infty \; , \tag{B. 114}$$

$$\tau_{r\theta} = 0 \; . \tag{B. 115}$$

Observe that, with boundary conditions at the wall and far from the cylindrical cavity:

$$\sigma_{rr}(R) = P_c \qquad \text{and} \qquad \sigma_{rr}(\infty) = P_\infty \quad , \tag{B. 116.a}$$

$$\sigma_{\theta\theta}(R) = 2P_\infty - P_c \qquad \text{and} \qquad \sigma_{\theta\theta}(\infty) = P_\infty \quad . \tag{B. 116.b}$$

Therefore, by substituting (B.116.a) and (B.116.b) in (B.95) the radial strain becomes

$$\varepsilon_{rr} = \frac{\partial u}{\partial r} = \frac{1}{E}\left[(-P_\infty + P_c\,)\frac{R^2}{r^2}(1+\vartheta)\right]. \tag{B. 117}$$

By integrating (B.117) we obtain

$$\frac{u}{r} = -\frac{1}{E}\left[(P_\infty - Pc\,)\frac{R^2}{r^2}(1+\vartheta)\right]. \tag{B. 118}$$

The total radial displacement in the cylindrical cavity is given by, $u(R)$, and tanking p as the perimeter of the cylinder cross-section;

$$\frac{\delta V}{V} = \frac{\mathrm{p}\,u(R)}{A_c} = \frac{2\pi R u(R)}{\pi R^2} = 2\frac{u(R)}{R} \tag{B. 119}$$

Therefore, from equation (B.118) the volume deformation as function of pressure can be written as

$$\frac{\delta V}{V} = -2\frac{(1+\vartheta)}{E}(P_\infty - Pc\,)\,. \tag{B. 120}$$

This also leads to cavity compressibility for a spherical shape in isentropic medium

$$\beta = -\frac{1}{V}\frac{\partial V}{\partial P} \rightarrow \beta_c = 2\frac{(1+\vartheta)}{E}\,. \tag{B. 121}$$

PLASTIC SCENARIO

From Karimi-Jafari, on the plastic zone the deformation rate will be sum of elastic and visco-plastic deformation rate,

$$\dot{\varepsilon} = \dot{\varepsilon}^{e} + \dot{\varepsilon}^{vp}\,. \tag{B. 122}$$

The rate of relevant deformation components can be written as

$$\dot{\varepsilon}_{rr} = \frac{\partial v}{\partial r} = \frac{1}{E}(\dot{\sigma}_{rr} - \vartheta\dot{\sigma}_{\theta\theta}) + \dot{\mu} + \dot{\lambda}\,, \tag{B. 123}$$

$$\dot{\varepsilon}_{\theta\theta} = \frac{v}{r} = \frac{1}{E}(\dot{\sigma}_{\theta\theta} - \vartheta\dot{\sigma}_{rr}) - \dot{\lambda} \qquad . \tag{B. 124}$$

From the relationship it is possible to conclude that $\dot{\mu} = \dot{\lambda}$. Integrating both equations we obtain

$$\varepsilon_{rr} = \frac{\partial u}{\partial r} = \frac{1}{E}(\sigma_{rr} - \vartheta\sigma_{\theta\theta}) + 2\lambda \quad , \tag{B. 125}$$

$$\varepsilon_{\theta\theta} = \frac{u}{r} = \frac{1}{E}(\sigma_{\theta\theta} - \vartheta\sigma_{rr}) - \lambda \qquad . \tag{B. 126}$$

STEADY-STATE PLASTIC SCENARIO

For the case of a steady state creep the stress in the massive is at stationary state, thus;

$$\dot{\sigma}_{rr} = \dot{\sigma}_{\theta\theta} = 0 \quad , \tag{B. 127}$$

$$\frac{\partial v}{\partial r} + \frac{v}{r} = 0 \qquad . \tag{B. 128}$$

The solution for the stress around the cavity is as derived by Karimi-Jafari is

$$\sigma_{rr} = \left(\frac{R}{r}\right)^{\frac{2}{n}}(P_\infty - P_c) - P_\infty\,, \tag{B. 129}$$

$$\sigma_{\theta\theta} = \left(\frac{R}{r}\right)^{\frac{2}{n}} (P_\infty - P_c)\left(1 - \frac{2}{n}\right) - P_\infty \ , \tag{B. 130}$$

$$\sigma_{zz} = \left(\frac{R}{r}\right)^{\frac{2}{n}} (P_\infty - P_c)\left(1 - \frac{1}{n}\right) - P_\infty \ . \tag{B. 131}$$

Therefore, from Van Sambeek [6], the solution for Norton-Hoff permanent creep model for a cylinder is;

$$\frac{\delta V}{V} = 2\frac{u(R)}{R} = \sqrt{3}A^* \left[\frac{\sqrt{3}}{n}(P_\infty - P_c)\right]^n \ . \tag{B. 132}$$

B.4. Chemical

B.4.1. Governing equations

Assume that the accumulated mass in the cavity is equal to the transferred mass form the its boundary.

$$V_c \frac{dc}{dt} = A_c k(c_{sat} - c(t)) \quad , \tag{B. 133}$$

And k is obtained from mass transfer dimensionless numbers i.e.

$$Sh = 0.13(GrSc)^{1/3} = \frac{kh}{D_{ab}} \, , \tag{B. 134}$$

$$Gr = \frac{h^3 g \rho \, \Delta\rho}{\eta_b^2} \quad , \tag{B. 135}$$

$$Sc = \frac{\eta_b}{\rho D_{ab}} \quad . \tag{B. 136}$$

a) Sphere

Therefore, for a spherical cavern eq. (B.133) reads

$$\frac{dc}{dt} = \frac{3}{R} k(c_{sat} - c(t)) \, . \tag{B. 137}$$

b) Cylinder

For a finite cylindrical cavern, the equation is then written as

$$\frac{dc}{dt} = 2\left(\frac{1}{R} + \frac{1}{H}\right) k(c_{sat} - c(t)) = \frac{2}{R}\left(1 + \frac{R}{H}\right) k\left(c_{sat} - c(t)\right) . \tag{B. 138}$$

B.4.2. Analytical solution

By applying boundary conditions, the solutions for spherical and cylindrical caverns are obtained.

a) Sphere

If the initial brine concentration is known, and k does not change significantly in time, as does the cavern average brine concentration (c_0), then a steady state transfer can be assumed. This is only valid during the short period of time of the test, i.e.

$$\frac{\Delta V_d}{\mathrm{V}} = \frac{3}{R} \frac{k(c_{sat} - c_0)}{\rho_s} t \quad . \tag{B. 139}$$

b) Cylinder

Analogous to sphere case solution we obtain

$$\frac{\Delta V_d}{\mathrm{V}} = \frac{2}{R}\left(1 + \frac{R}{H}\right) \frac{k(c_{sat} - c_0)}{\rho_s} \; t \, . \tag{B. 140}$$

However, for the case of $H \gg R$ or dissolution occurs only radially, the equation becomes $\frac{\Delta V_d}{\mathrm{V}} = \frac{2}{R} k(c_{sat} - c_0)t$.

Appendix C – Physical constants

The physical constants used to obtain the results to be presented in the upcoming sections are here summarized. A range of the possible values is used to obtain upper and lower ranges of cavern volume, and standard values for tuning.

Table 3 List of parameters and used values for sensitivity analysis of the models

Symbol	Parameter	Value			Unit
		Minimum	Maximum	Standard	
A	Norton-Hoff law constant	$7.3 * 10^{-5}$	$7.31 * 10^{-1}$	$1.3 * 10^{-2}$	$[\frac{1}{s\,\mathrm{MPa}^n}]$
α	Thermal diffusivity			$3 * 10^{-6}$	$[\frac{m^2}{s}]$
β	Total cavern compressibility	$2.0 * 10^{-10}$	$9.7 * 10^{-10}$	$3.5 * 10^{-10}$	$[Pa^{-1}]$
β_b	Brine compressibility	$2.3 * 10^{-10}$	$4.5 * 10^{-10}$	$2.3 * 10^{-10}$	$[Pa^{-1}]$
β_s	Sump compressibility			$0.82 * 10^{-10}$	$[Pa^{-1}]$
C_b	Brine heat capacity			3840	$[\frac{W}{\mathrm{kg}°\mathrm{C}}]$
C_s	Salt heat capacity			926	$[\frac{W}{\mathrm{kg}°\mathrm{C}}]$
c_f	Fluid sound velocity	1500	1865	1865	$[\frac{m}{s}]$
c_{sat}	Salt concentration at saturation			$53 * 10^3$	$[\frac{mol}{m^3}]$
D_{ab}	Salt mass diffusivity coefficient			$0.12 * 10^{-9}$	$[\frac{m^2}{s}]$
E	Young's modulus of the rock	$0.5 * 10^{10}$	$4 * 10^{10}$	$2 * 10^{10}$	$[Pa]$
γ_b	Brine volumetric expansion			$4.4 * 10^{-4}$	$[°\mathrm{C}^{-1}]$
g	Acceleration of gravity			9.81	$[\frac{m}{s^2}]$
K_s	Permeability of salt formation	10^{-22}	10^{-19}	10^{-19}	$[m^2]$
K_s^{th}	Thermal conductivity of salt			6	$[\frac{W}{m°\mathrm{C}}]$
n	Norton-Hoff law exponent	3.1	3.6	3.6	$[-]$
η_b	Dynamic viscosity of brine			$1.2 * 10^{-3}$	$[Pa.s]$
P_∞	Lithostatic pressure			$5.8 * 10^7$	$[Pa]$
ψ^o	Leak constant per cavern volume	10^{-20}	10^{-15}	10^{-17}	$[\frac{m^3}{m^3 Pa.s}]$
$\frac{Q}{R}$	Norton-Hoff law constant	4100	7500	6120	$[K]$
ρ_b	Brine density			1265	$[\frac{kg}{m^3}]$
T_o, θ_o	Initial cavern fluid temperature	45	75	60	$[°\mathrm{C}, K]$
$T_\infty, \theta_R^\infty$	Rock geothermal temperature	75	95	86.5	$[°\mathrm{C}, K]$

Appendix D – Sensitivity to parameters

The sensitivity analysis of the of each component contributing in the pressure response of any of the model is studied is this section. The objective is to assess the impact of uncertainties in each term (thermal, hydraulic, mechanical, and chemical volume) of the models. The chemical model sensitivity assessment is done for the case of undersaturated brine, rather than additional dissolution due to cavern pressure increase as suggested by Van Sambeek and Bérest.

D.1. Thermal

The sensitivity of the total volume added by thermal influences during a compressibility test is displayed below for the case of a $10^6\ m^3$ cavern, with standard parameters as stablished in appendix C. The results are for the volume added after 1 hour of shut-in of the cavern with a $10\ bar$ pressure increase. Each of the parameters is then changed to analyse its impact in the total volume, Figure 17.

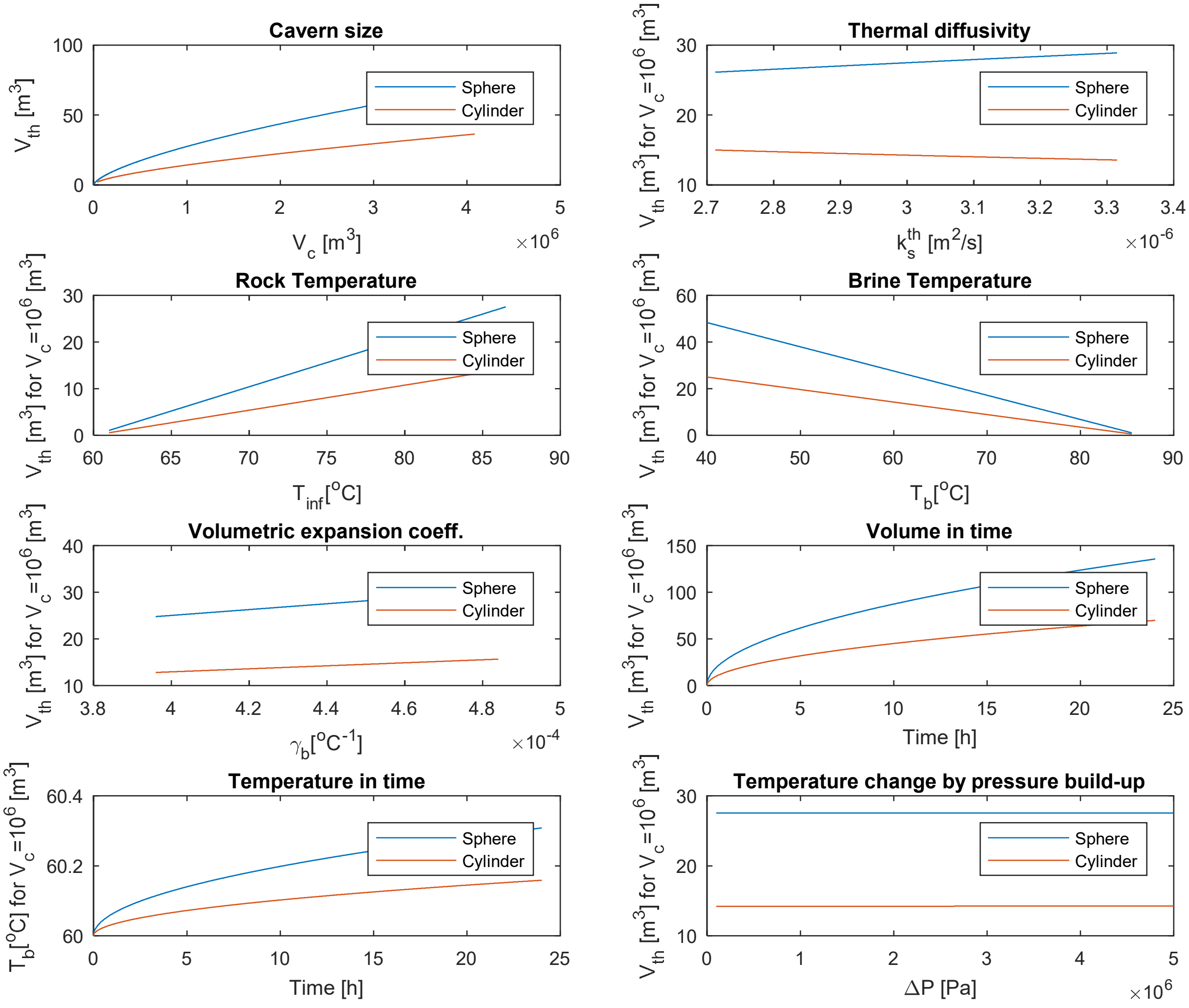

Figure 17 Sensitivity analysis plots for thermal volume used in all models. The sensitivity is performed for a cavity of $10^6\ m^3$ in $1\ hour$ of compressibility test, all values are shown for a total pressure increase of $10\ bar$.

D.2. Hydraulic

The sensitivity of the total volume added by hydraulic influences during the compressibility test is displayed below for the case of a $10^6\ m^3$ cavern, with standard parameters as stablished in appendix C. The results are for 1 hour of shut-in. Each of the parameters is then changed to analyse its impact in the total volume, as in plots from Figure 18.

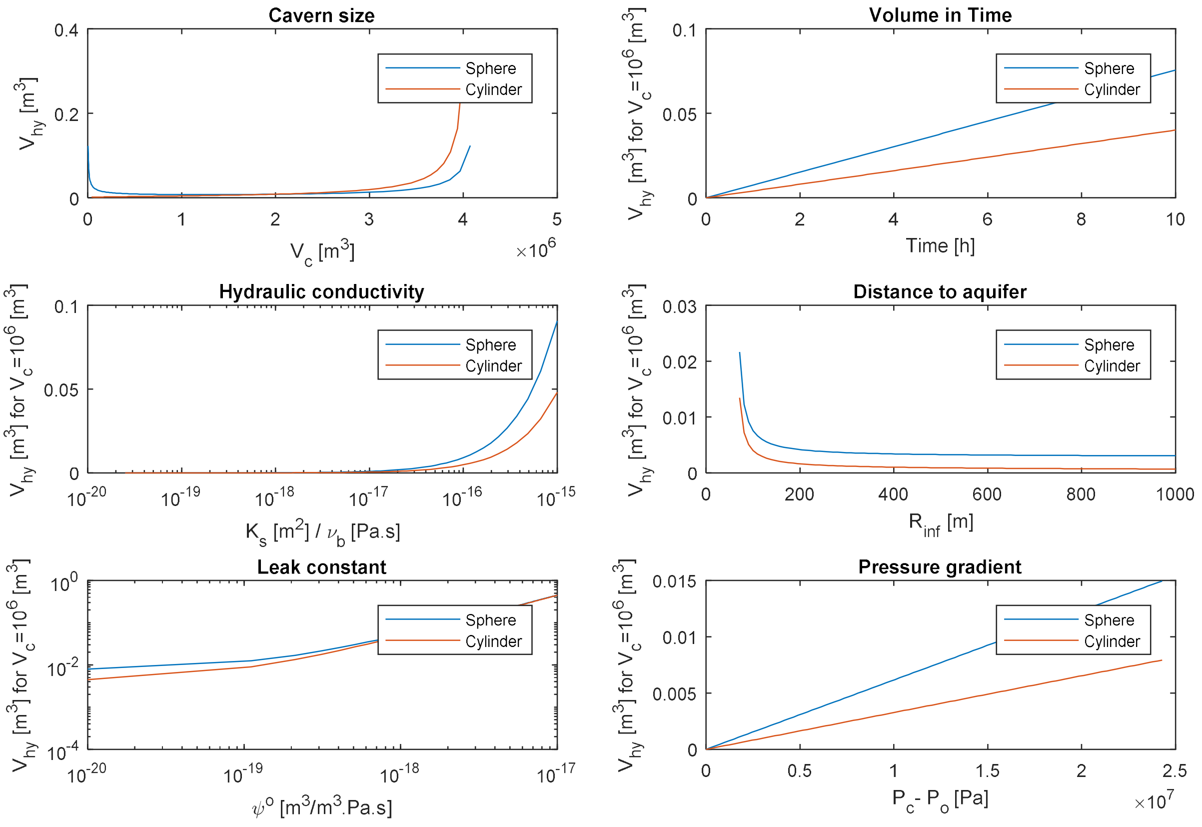

Figure 18 Sensitivity analysis plots for hydraulic volume used in all models. The sensitivity is performed for a cavity of $10^6\ m^3$ *in* $1\ hour$ *of compressibility test, all values are shown for a total pressure increase of* $10\ bar$

D.3. Mechanical

The total volume added by creep, or plastic deformation, of the rock salt during the compressibility test is depended on Norton-Hoff parameters, and cavern shape. In respect to shape the minimum radial creep occurs when the cavern has a spherical shape, and the maximum when it has a cylindrical. Hence, for different shapes;

$$\left(\frac{\delta\dot{V}_{cr}}{\mathrm{V}}\right)_{sphere} = \frac{3}{2}A^*\left[\frac{3}{2n}(P_\infty - P_C)\right]^n \quad \propto \quad \left(\frac{\delta\dot{V}_{cr}}{\mathrm{V}}\right)_{cylinder} = \sqrt{3}A^*\left[\frac{\sqrt{3}}{n}(P_\infty - P_c)\right]^n \tag{D.1}$$

$$f(\Omega) = a\left[\frac{a}{n}\right]^n,\ a = \left[\frac{3}{2}, \sqrt{3}\right] \tag{D.2}$$

In eq. (D.2) the variable $f(\Omega)$ is a function of shape a (which is different form shape factor F) and n the Norton-Hoff law coefficient.

The sensitivity of the volume change in the cavern due to creep after 1 hour of shut-in is displayed in Figure 19.

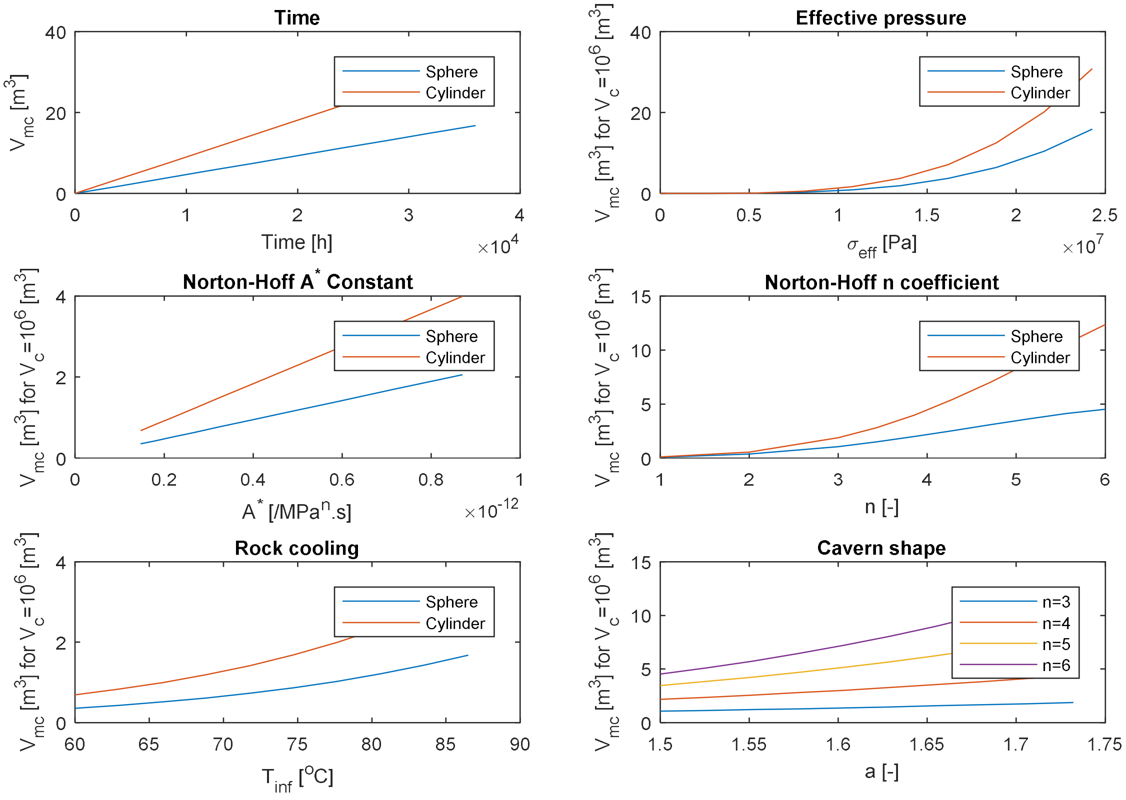

Figure 19 Sensitivity analysis plots for mechanical volume used in all models. The sensitivity is performed for a cavity of $10^6\ m^3$ in $1\ hour$ of compressibility test, all values are shown for a total pressure increase of $10\ bar$. Rock cooling occurs when the temperature of the rock is below the geothermal temperature due to cold water injection.

D.4. Chemical

One of the most important aspects of active leaching caverns is the dissolution impact in compressibility testing. Brine concentration can be obtained from production data before the test.

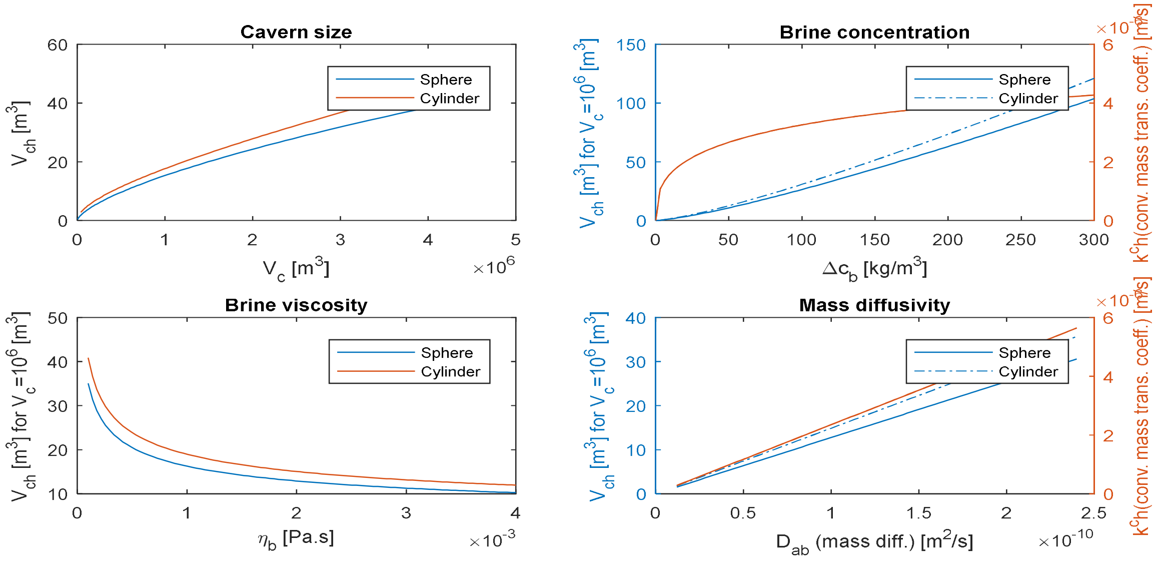

Figure 20 Sensitivity analysis plots for chemical volume applied in proposed model. The sensitivity is performed for a cavity of $10^6\ m^3$ in $1\ hour$ of compressibility test, all values are shown for a total pressure increase of $10\ bar$.

D.5. Compressibility

Another important factor in compressibility tests is the cavern compressibility itself, which is depend on the rock properties and cavern fluid.

The shape factor very from a sphere to a cylindrical cavity, although it can be greater than that for penny-shaped cavity. Rock properties relevant to obtain elastic deformation are rock Young Modulus and Poisson's ratio, which can vary between $5\ GPa$ to $40\ GPa$ and 0.2 to 0.3, respectively, for rock salt. Hence, the compressibility factor for salt cavities that are not penny-shaped is between $\beta_c = 0.45 * 10^{-10}\ Pa^{-1}$ and $\beta_c = 5.2 * 10^{-10}\ Pa^{-1}$.

Fluid compressibility is dependent on density, and therefore it's sonic velocity. The compressibility of the fluid within the cavity may vary from fresh water to saturated brine. The sonic velocity in fresh water is $1500\ m/s$ for a $1000\ kg/m^3$ density, and in saturated brine from $1865\ m/s$ and $1299\ kg/m^3$ (as observed in field data). Thus, brine, or fluid, compressibility can vary from $\beta_w = 4.4 * 10^{-10}\ Pa^{-1}$ to $\beta_b = 2.2 * 10^{-10}\ Pa^{-1}$ for a saturated solution of sodium chloride.

Figure 21 displays the range of compressibility between spherical and cylindrical shaped caverns.

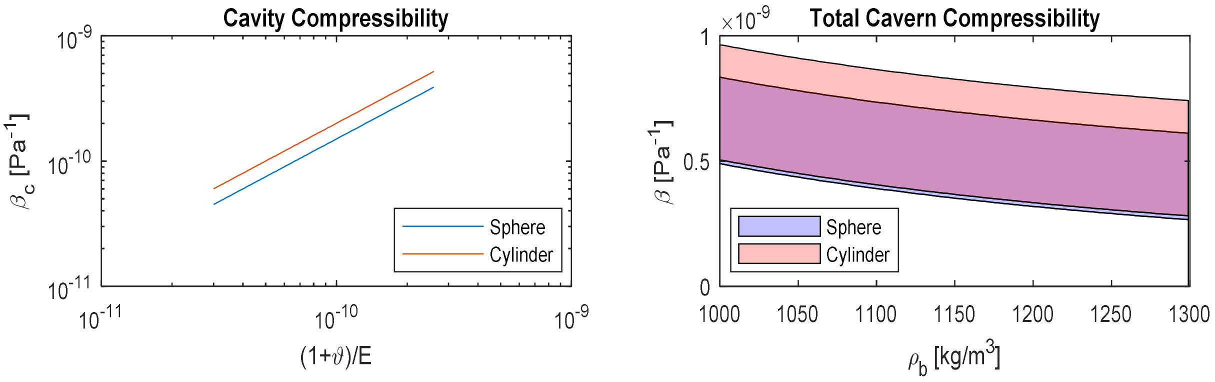

Figure 21 On the right plot cavity compressibility is displayed as function of rock constants, on the left the range of possible total compressibility from cavity and saturated to undersaturated brine density without sump contribution

This analysis is usefull to determine unphysical values of the compressibility for a salt cavern that can be used to disregard data from unsuccesful compressibility test. For caverns under leaching for a long period of time the compressibilty factor should tend to the most right side range for highly saturated brine, meanwhile for midaged caverns the value can be more abrangent.

Furthermore, the compressibility of a not perfectly spherical or perfectly cylindrical cavities must be within the overlaying range, for e.g. the compressibility of a real shaped cavern filled with highly saturated brine is expected to be between $\beta = 2.8 * 10^{-10}\ Pa^{-1}$ and $\beta = 6.1 * 10^{-10}\ Pa^{-1}$ for any shape (non-penny shaped cavity) and fluid density. Penny shaped caivities can present much larger values of compressibility than that of a cylinder [8], and such shape is characteristic of cavities with more than one well, what is not the case of BAS3O and BAS4.

Also, rock properties are assumed to be constant, thus the ratio $(1 + \vartheta)/E$ is not changing, but the shape of the cavity or brine concentration might change with leaching mode.

Retaken the previous example of a saturated cavern at any moment in time, given that the rock has $E = 20\ GPa$ and $\vartheta = 0.2$, the total compressibility must then be between $\beta = 3.1 * 10^{-10}\ Pa^{-1}$ and $\beta = 3.4 * 10^{-10}\ Pa^{-1}$ according to cavern shape. This analysis is usefull to narrowdown the possible values for the cavern compressibility, Figure 22.

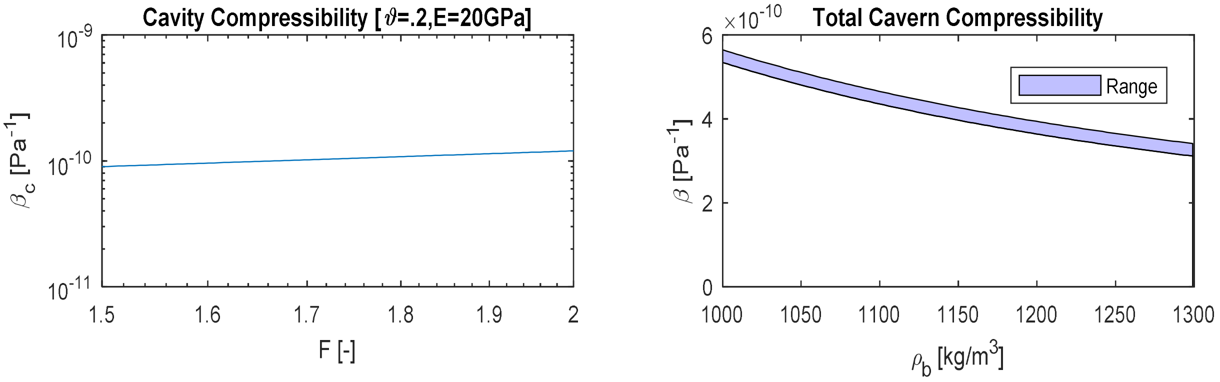

Figure 22 On the right cavity compressibility range as a function of shape for given rock constants, on the left the impact of brine density on the total compressibility for the same rock constants with unknown shape (range from spherical to cylindrical shape case).

Appendix E – Results for BAS3O and BAS4

Field data was tested for different models, with a different range of possible parameters. The parameters range is established from possible values from observed production data. The cavern equivalent radius and shape is necessary input to the model. Although, they are unknown it is possible to obtain an estimated range from leaching simulators and volume balance forecasts. They model is then tuned to obtain best fit results.

E.1. BAS3O

E.1.1. Field data

Field data is analysed by adopting Thiel's approach. At this perspective the slope between injected volume by cavern volume and normalized pressure increase is directly correlated to cavern volume and compressibility. By plotting compressibility tests performed at different dates in time, for BAS3O well, it is possible to see that the trend is not linear. This becomes clearer by plotting the derivative of the data set, what can be interpreted by Thiel's compressibility or hydraulic response.

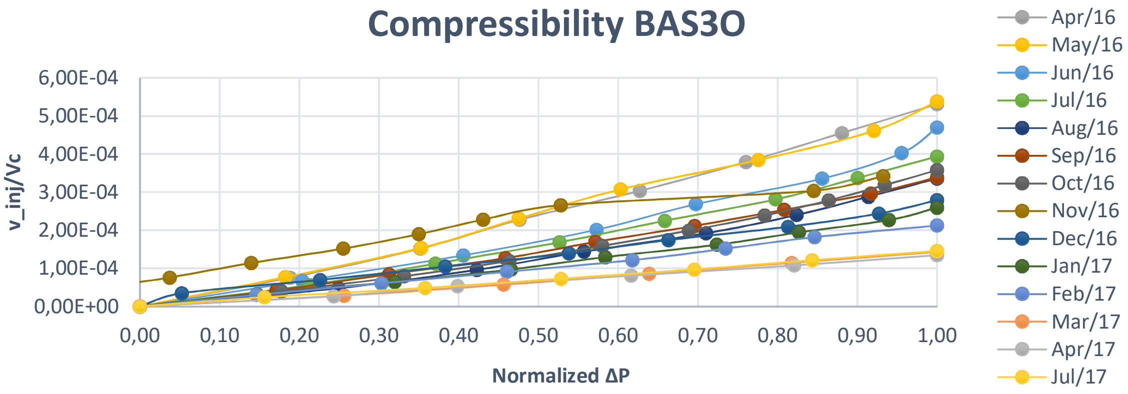

Figure 23 Compressibility test normalized data set for BAS3O.

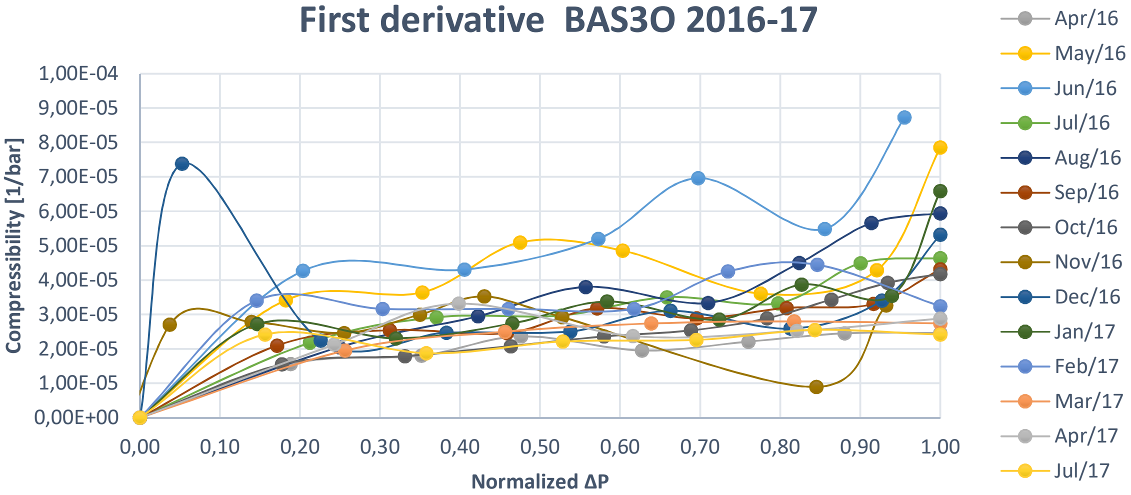

Figure 24 Compressibility of the cavern for each moment of the test from data set for BAS3O.

E.1.1. Analysis

Previous models have been applied to field data using the range of parameters in appendix C. The model has been tuned to incorporate the impact of sump on the compressibility. From the analysis of the range of possible outcomes (Figure 25, 26 and 27). The range represents the area between the minimum physically possible cavern volume (calculated using the referred model by applying low case parameters) and the maximum cavern volume (applying the referred model using high case scenario parameters) . It is possible to conclude that there is indeed a trend between compressibility and cavern volumes. However, the level of uncertainty is too large for the given models.

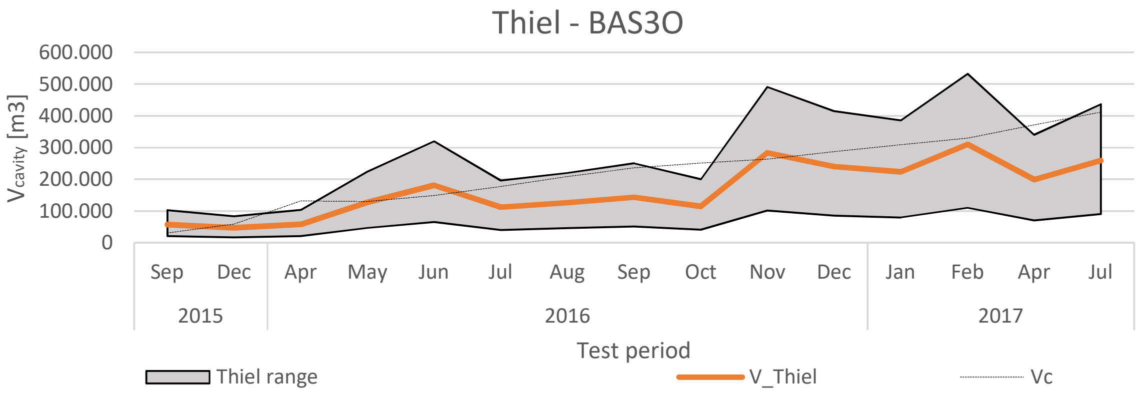

Figure 25 Maximum range of BAS3O cavern volume interpretation for different compressibility for Thiel's approach

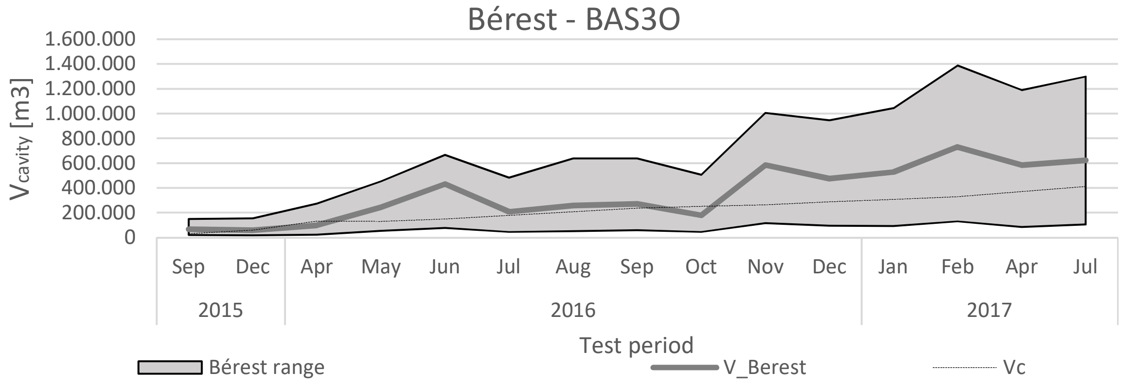

Figure 26 Maximum range of BAS3O cavern volume interpretation for different compressibility and secondary phenomena parameters for Bérest's approach

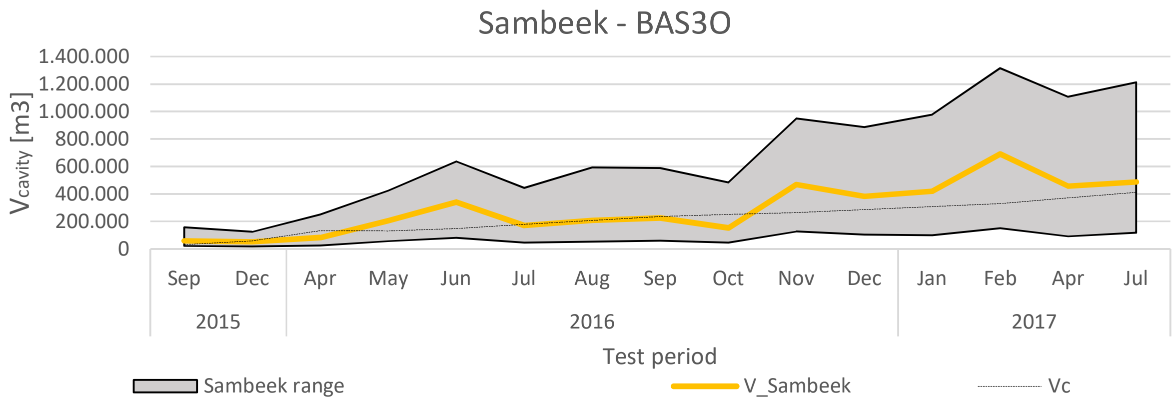

Figure 27 Maximum range of BAS3O cavern volume interpretation for different compressibility and secondary phenomena parameters for Van Sambeek's approach

The proposed model is then applied. The model helps in narrowing down the range of possible outcomes from the test when compared to Van Sambeek and Bérest approach, Figure 28. It is possible for it to be improved by calibrating the input data with laboratory surveys, such as creep constants and downhole brine temperature.

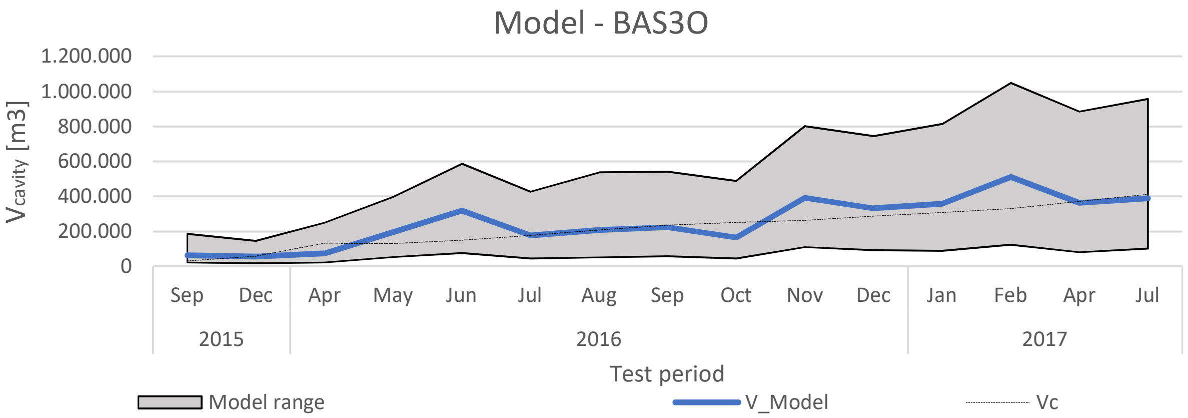

Figure 28 Maximum range of BAS3O cavern volume interpretation for different compressibility and secondary phenomena parameters for new proposed model.

The calibrated results for each of the models is presented in Figure 29.

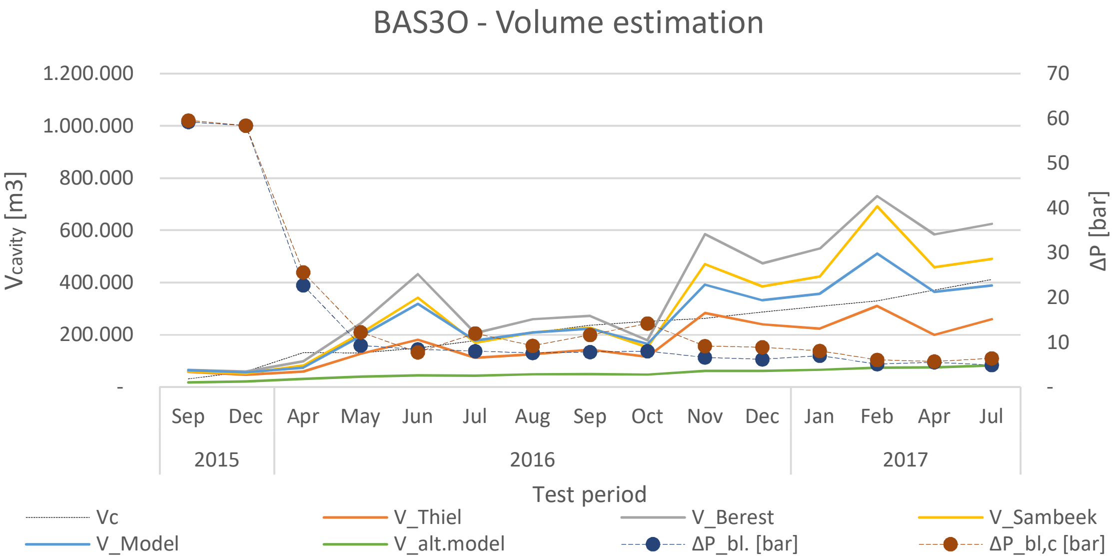

Figure 29 Summary of results from tuned field data for BAS3O

The model gives some sharp results. In the data points where it fails, a possible explanation is either test failure due to untracked leaks or change in average in situ brine temperature. Thiel's model shows a consistent approximation if properly calibrated, with an error of up to 30%, except for October 2015 and April 2016. Also, for Thiel's model 6 data points fall within the range of 10% accuracy under calibration of parameters to achieve best fit for the model. The proposed model presents 8 data points with error inferior to 5% under calibration to achieve best fit curve for this model.

Other models present a higher discrepancy, and therefore are not accurate for cavity volume prediction for the case of BAS3O.

E.2. BAS4

E.2.1. Field data

Analogous to BAS3O the same analysis has been performed for the compressibility test data set. For this cavern the data seems to be more linear, Figure 30, with exception of some data points. Cavern hydraulic response falls into a range of smaller values than that of BAS3O, Figure 31. However, the caverns should present similar responses, since they are both located at the same halite formation and similar depths. The difference between the cavities is due to the fact that BAS4 is larger and older than BAS3O.

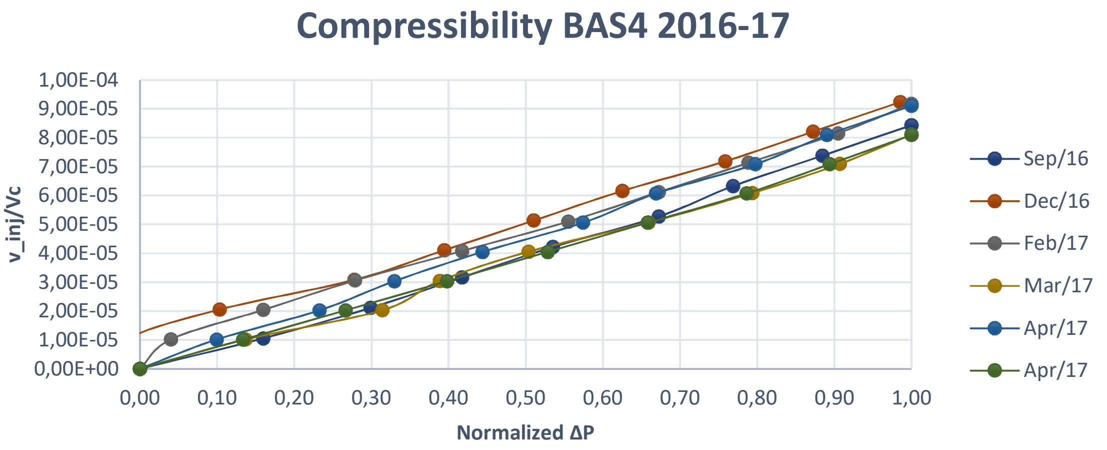

Figure 30 Compressibility test data set for BAS4.

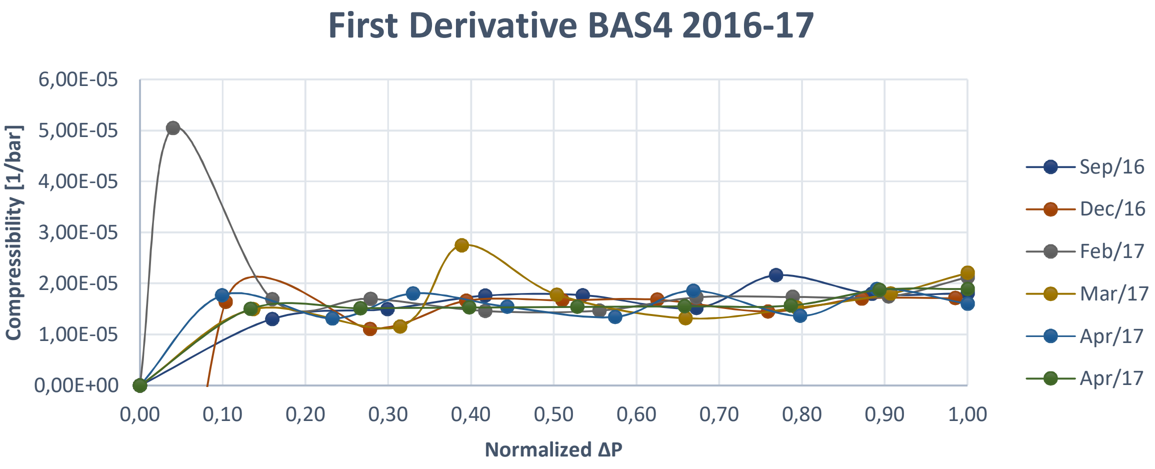

Figure 31 Compressibility of the cavern for each moment of the test from data set for BAS4.

From the pressure response it is visible that the pressure response of BAS4 is more stable, with moderate variations. There are many reasons for this observation, one is that BAS3O being a side track well has its hydraulic response more erratic due to well leaks on complex completions. Another reason may be simply because older caverns present more linear behaviour due to steady state production, with almost constant average brine concentration.

Under Thiel's model the cavities would have an unphysical value for cavern shape and compressibility, as in plot from Figure 31. Thiel's model is then not valid for BAS4, unless it is applied with constant correction factor.

E.2.2. Analysis

Previous models are applied to the BAS4 cavern data set. Even with tuning of the parameters to best fit real values it is difficult to match cavern volume with the known volume data set. For the case of Thiel's model for compressibility test the volume is considerably underestimated, Figure 32. For the other models, Figure 33 and Figure 34, the size is overestimated due to the creep input as part of the injected volume.

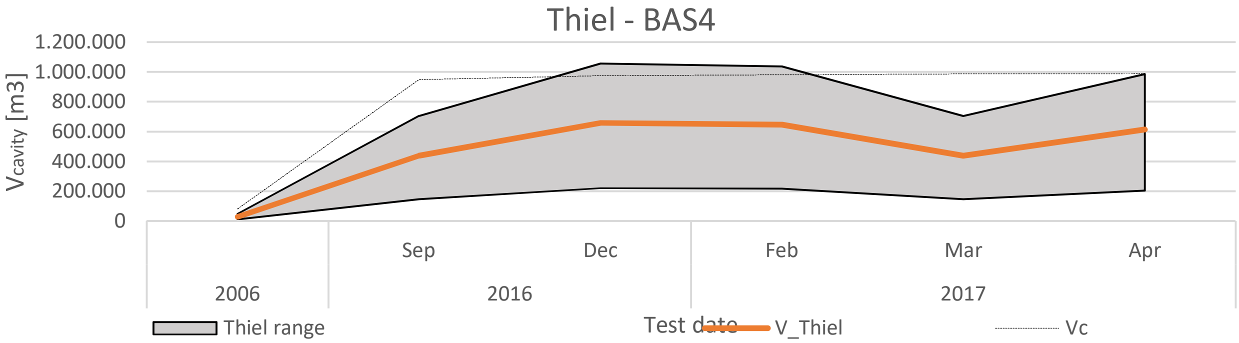

Figure 32 Maximum range of BAS4 cavern volume interpretation for different compressibility for Thiel's approach

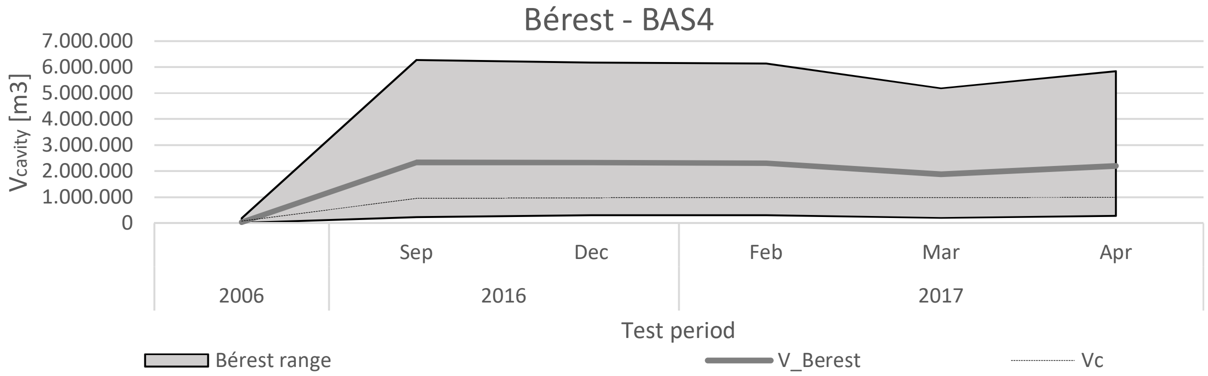

Figure 33 Maximum range of BAS4 cavern volume interpretation for different compressibility and secondary phenomena parameters for Bérest's approach

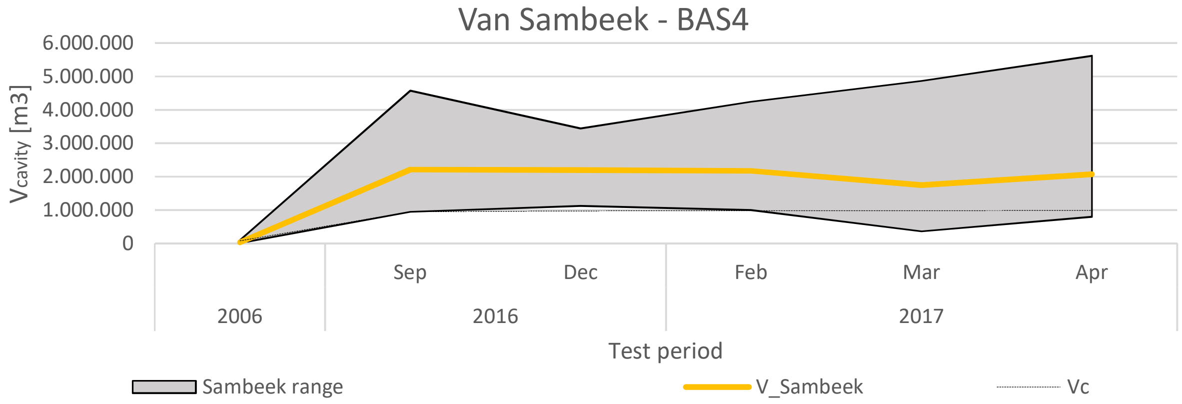

Figure 34 Maximum range of BAS4 cavern volume interpretation for different compressibility and secondary phenomena parameters for Van Sambeek's approach

The proposed model narrows down the range of possible values, when compared to Bérest and Van Sambeek, and succeeds to deliver cavern volumes within the range of maximum and minimal possible outcomes (according to maximum field observed creep, brine temperature and a range of cavern compressibility), Figure 35. Accurate results can then be obtained by tuning of parameters.

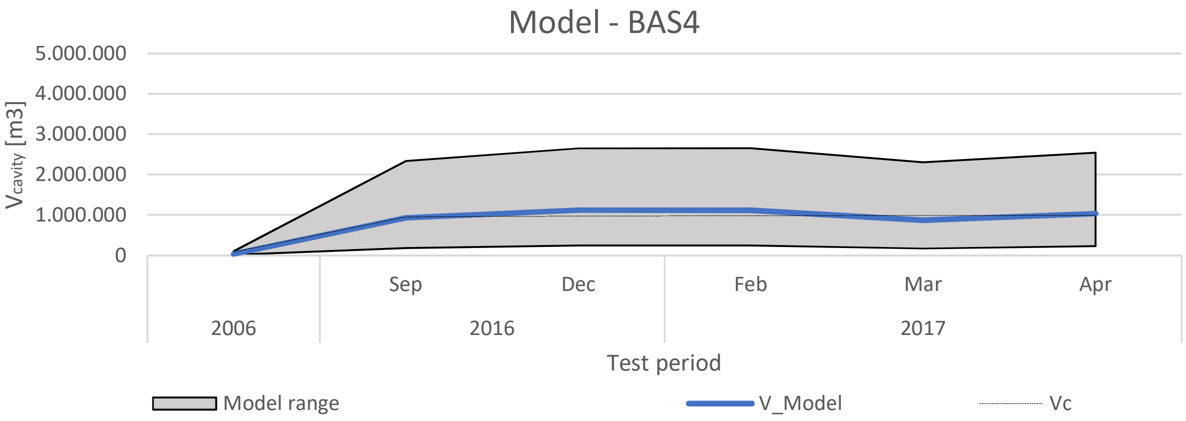

Figure 35 Maximum range of BAS4 cavern volume interpretation for different compressibility and secondary phenomena parameters for new proposed model

The models are then calibrated and compared, Figure 36, using physical possible compressibility factors aligned with those of BAS3O. The values must be somewhat similar since caverns are in same formation, and only fluid compressibility can be different between caverns.

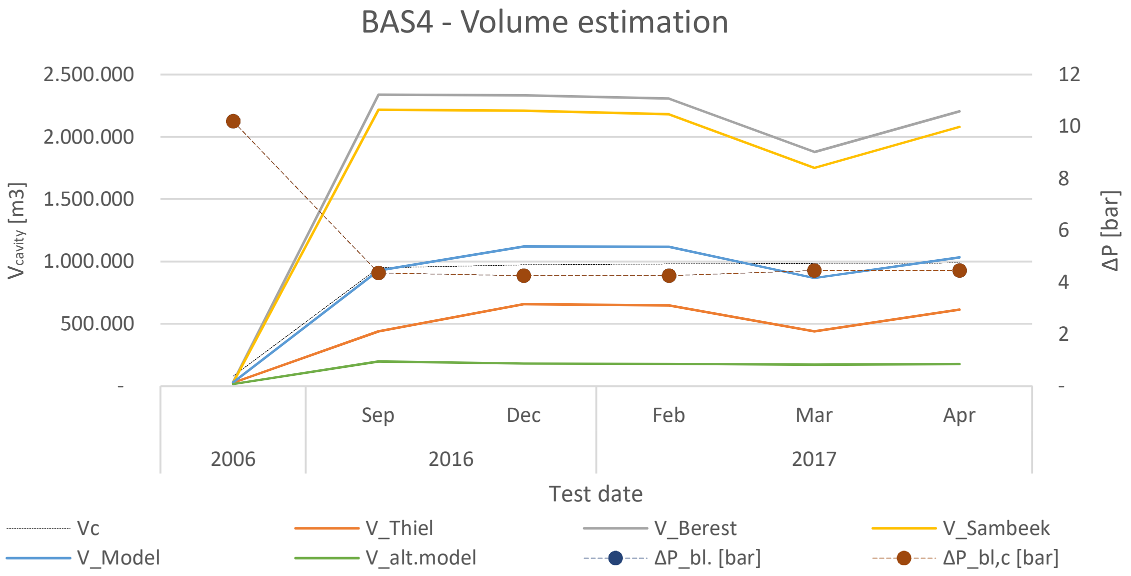

Figure 36 Summary of results from tuned field data for BAS4

The proposed model is then the only to satisfy volume prediction for BAS4 with 12% average error, since Thiel's model results in unphysically low compressibility (below saturated brine).

Appendix F – Alternative model analysis

The alternative model presented in the recommendation has been applied to the data set, however it has not been fully investigated in this work. The alternative model is obtained as in appendix A, eq. (A.39), by applying a mass-volume balance approach to the compressibility problem,

$$V = \frac{\Delta V_{inj}}{\Delta P_c}\left\{\beta - \frac{1}{\Delta P_c}\left[\frac{\Delta V_{mc}}{V} - \frac{\Delta V_{ch}}{V}\left(1+\frac{\rho_s}{\rho_b}\right) + \frac{\gamma_b \Delta T}{1+\gamma_b \Delta T}\right]\right\}^{-1}. \tag{F.1}$$

Each contributing volume is obtained as summarized in appendix B, table 2.

The prosed model and alternative proposed model are compared by applying sensitivity analysis since they result in extremely different values for the same input parameters.

F.1. Sensitivity to compressibility

From figures 37 and 38 we conclude that the alternative model is not as sensitive to cavern compressibility as the proposed model. In addition to that one can observe that by changing the compressibility alone in the alternative model, figure 38, it is not possible to achieve the forecasted cavern volume, hence other parameters have to be changed to increase accuracy.

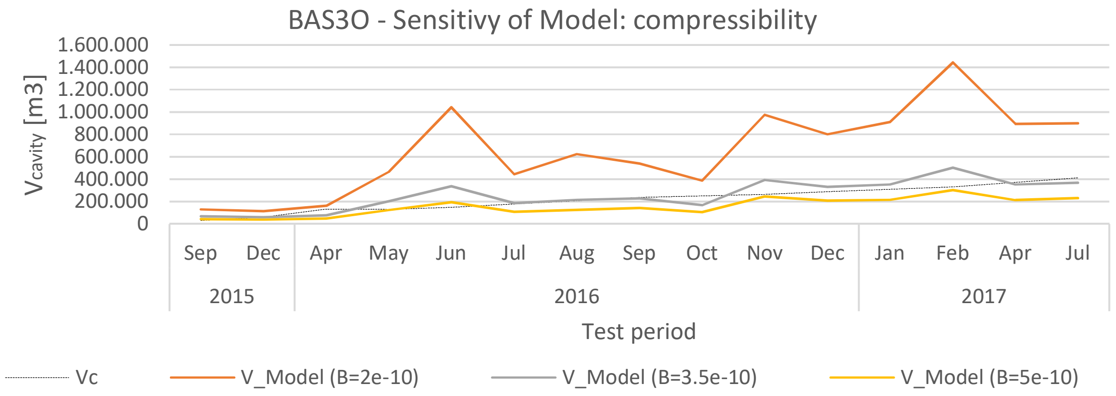

Figure 37 Sensitivity analysis of estimated cavern volume for BAS3O from model to compressibility, adopting calibration parameters as in appendix C.

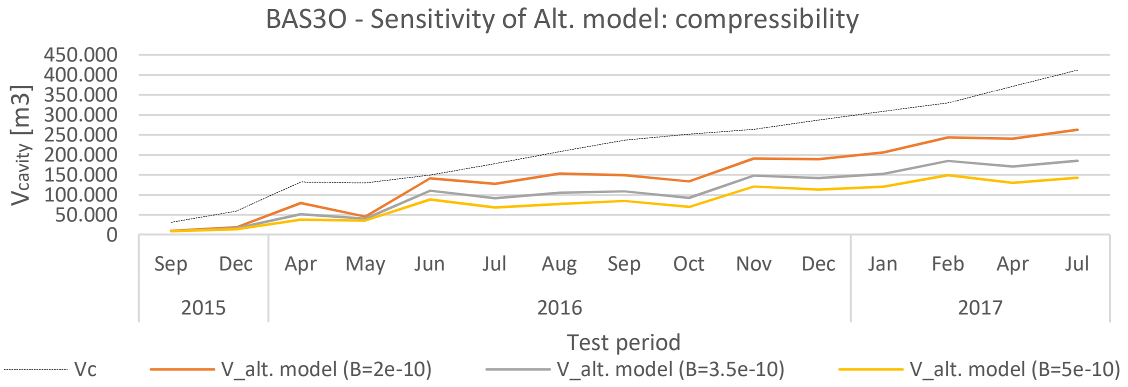

Figure 38 Sensitivity analysis of estimated cavern volume for BAS3O from alternative model to compressibility, adopting calibration parameters as in appendix C.

The same analysis is then performed for BAS4 cavern, figure 39 and 40. From figure 40 we conclude that the alternative model does not admit such low compressibility values for the case of September 2016 BAS4 data set, since denominator in equation (F.1) would be to low resulting in a jump in predict volume.

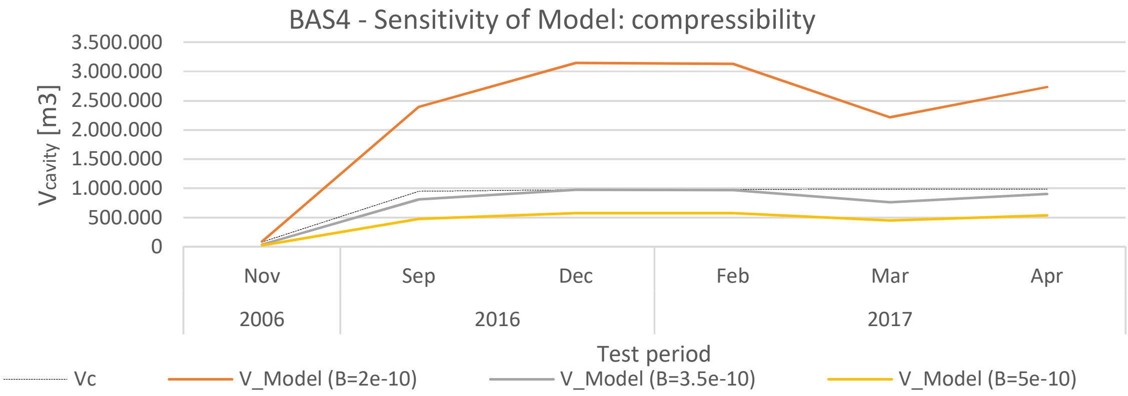

Figure 39 Sensitivity analysis of estimated cavern volume for BAS4 from model to compressibility, adopting calibration parameters as in appendix C.

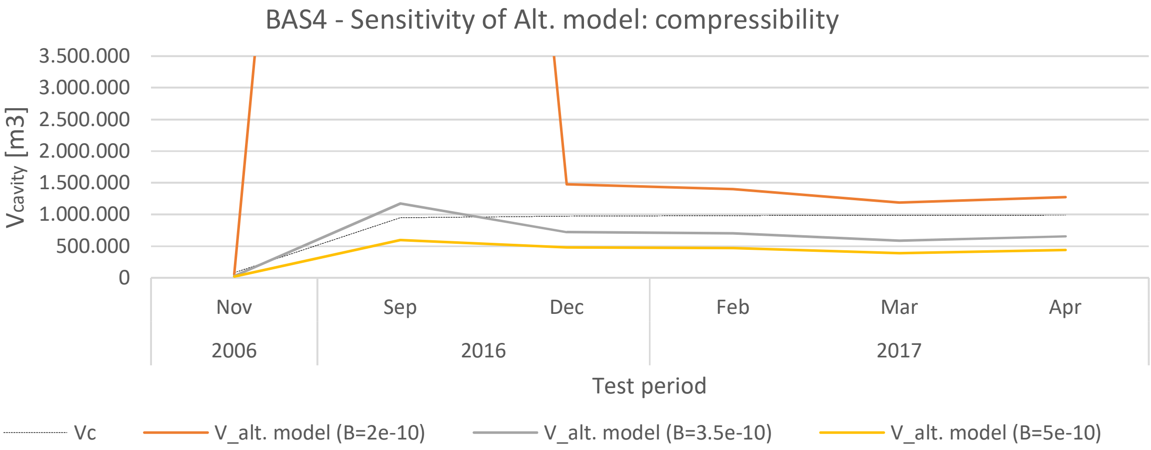

Figure 40 Sensitivity analysis of estimated cavern volume for BAS4 from alternative model to compressibility, adopting calibration parameters as in appendix C.

From figure 37 and 39 we conclude that the caverns compressibility should be near to that predicted for the proposed model. No conclusion can be inferred for the alternative model from figures 38 and 40, because that data is not enough to obtain a common value for cavern compressibility.

F.2. Sensitivity to temperature

The sensitivity analysis is then performed for different initial brine temperature, figure 41 and 42, for the alternative model for BAS3O and BAS4 cavern data set. The result displays the alternative model is more sensitive to brine temperature than to the compressibility, and it once again results in unphysical values for September 2016 BAS4 data set.

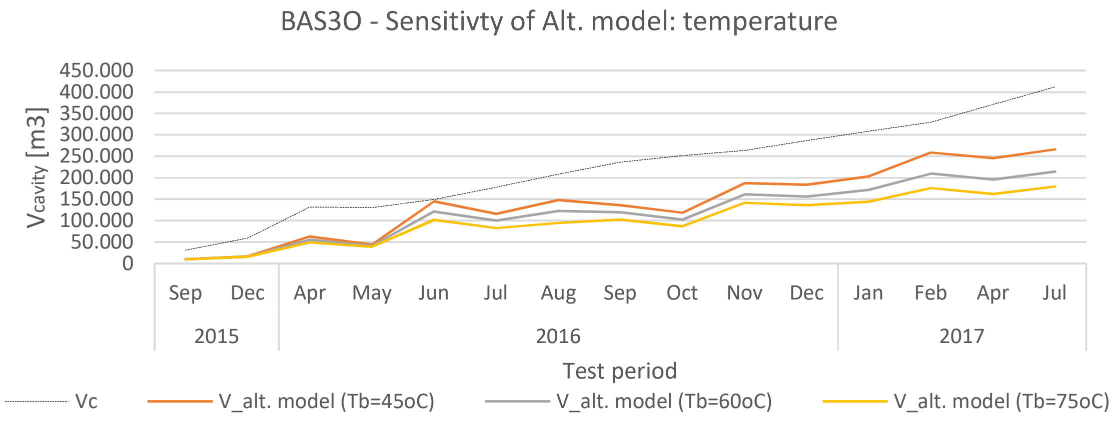

Figure 41 Sensitivity analysis of estimated cavern volume for BAS3O from alternative model to temperature, adopting calibration parameters as in appendix C.

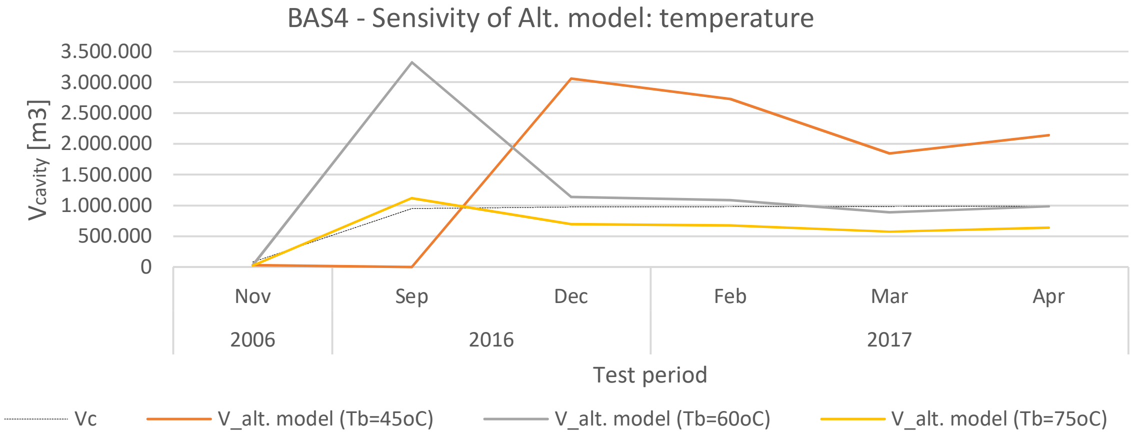

Figure 42 Sensitivity analysis of estimated cavern volume for BAS4 from alternative model to temperature, adopting calibration parameters as in appendix C.

F.3. Tuning of alternative model

In an attempt to obtain best fit curve for the alternative model the values for compressibility and initial brine temperature have been calibrated.

Some data points have their error reduced when compared to the proposed model, yet the proposed model comes out with the lowest average error. In addition to that the best fit solutions for the alternative model is only reached by applying unphysical values for cavity compressibility (lower than that of the fluid within the cavity alone).

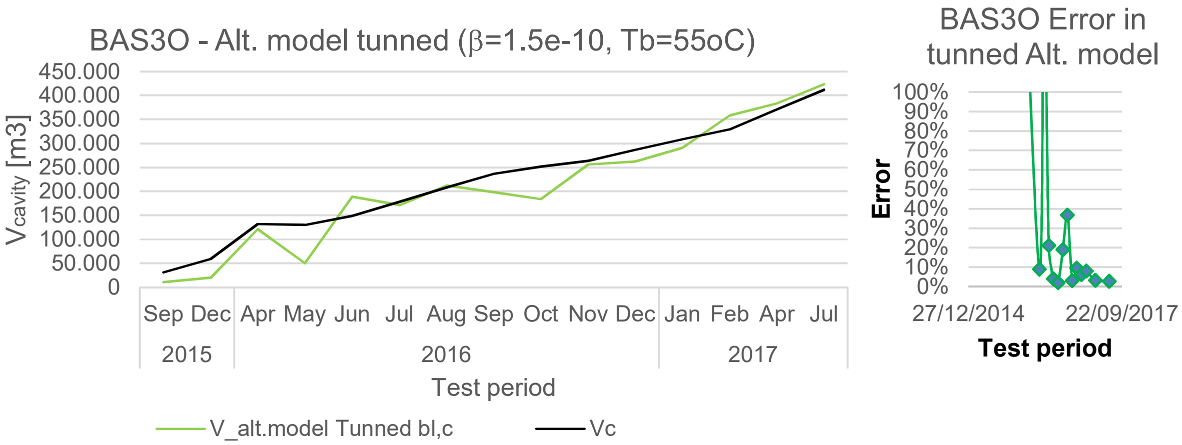

Figure 43 On the right, best fit estimated cavern volume for BAS3O using alternative model. On the left error from best fit curve for alternative model in BAS3O data set.

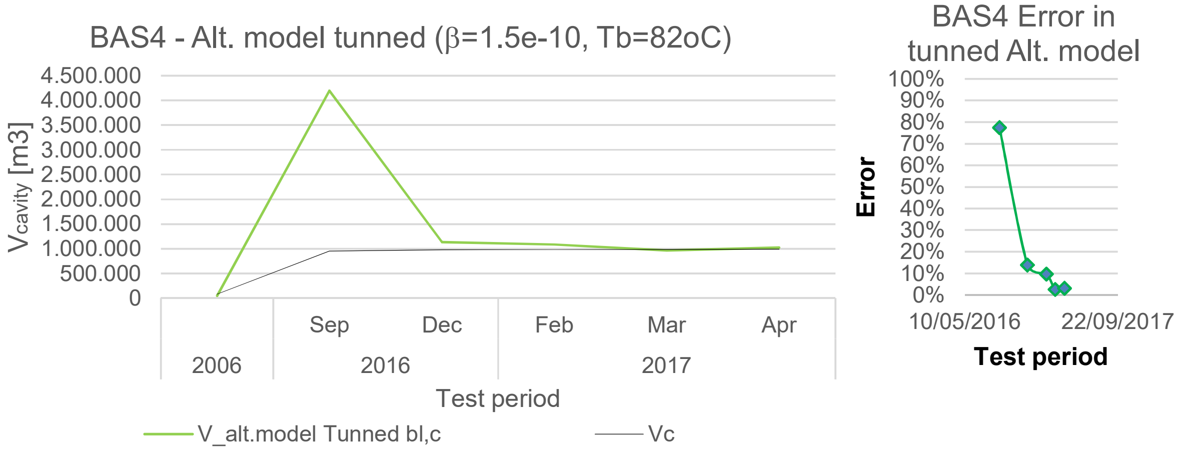

Figure 44 On the right, best fit estimated cavern volume for BAS4 using alternative model. On the left error from best fit curve for alternative model in BAS4 data set.

F.4. Indicators for tuning of proposed model

The proposed model has to be calibrated as the system changes in time with leaching operation. From the sensitivity analysis performed in this section it is possible to conclude that compressibility and temperature are a major player in estimated cavern volume from proposed model. The calibration to field application can use of charts in figure 45 and 46 to update model parameters according to known values of cavern volume after a sonar survey and performing a compressibility test immediately after (within days) the sonar operation.

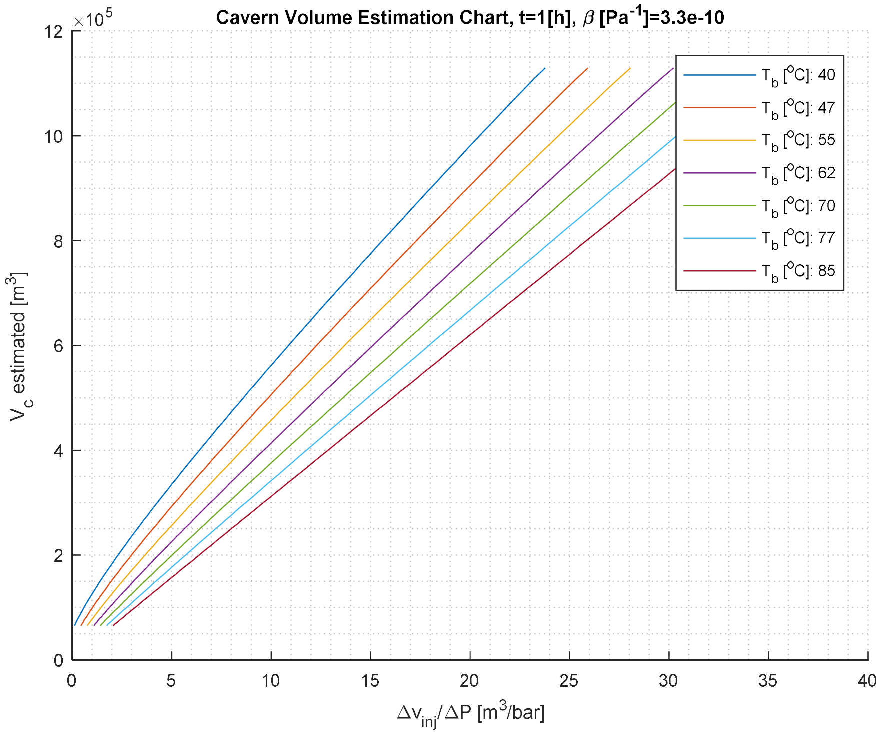

Figure 45 Indicator of brine temperature, for the case of proposed model, for known cavern volume and compressibility test measurements.

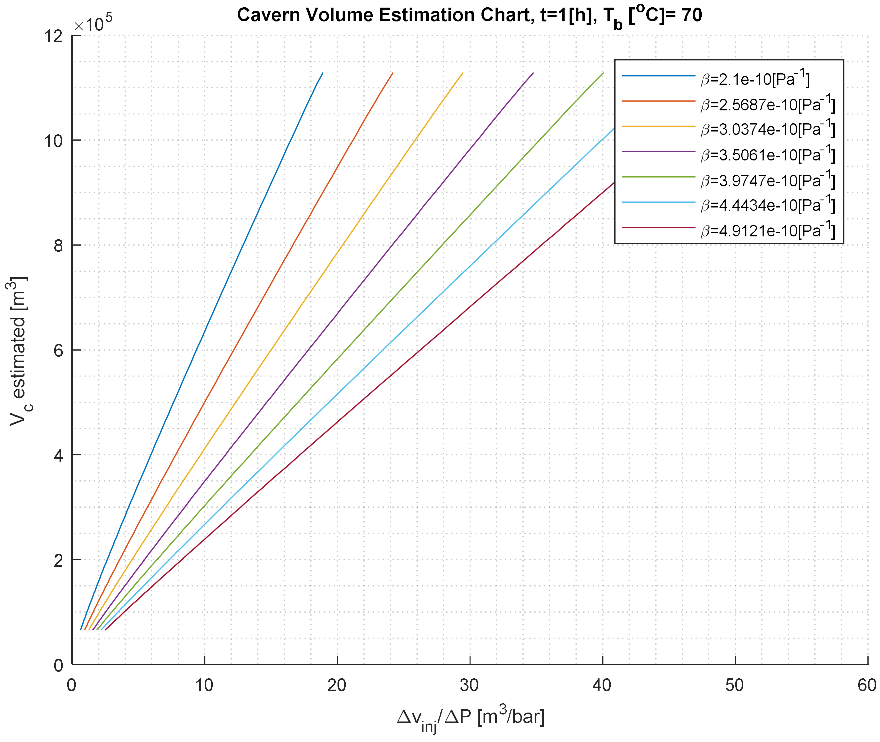

Figure 46 Indicator of cavern compressibility, for the case of proposed model, for known cavern volume and compressibility test measurements.